Trinity College Dublin
Coláiste na Tríonóide, Baile Átha Cliath
The University of Dublin

Modelling techniques to inform the design of sub-wavelength periodic acoustic structures

Lara Flanagan

Supervisor: Prof. Henry Rice

Department of Mechanical & Manufacturing Engineering

Trinity College Dublin

Ireland

2022

A thesis submitted to the University of Dublin in partial fulfilment of the requirements for the degree of Doctor of Philosophy

Declaration

I declare that this thesis has not been submitted as an exercise for a degree at this or any other university and it is entirely my own work.

I agree to deposit this thesis in the University's open access institutional repository or allow the Library to do so on my behalf, subject to Irish Copyright Legislation and Trinity College Library conditions of use and acknowledgement

I consent to the examiner retaining a copy of the thesis beyond the examining period, should they so wish (EU GDPR May 2018).

Lara Catherine Hélène Flanagan,

September 2021

Abstract

Minimising the environmental impact of aircraft noise and ensuring the sustainability of air travel in the future is crucial for the development of the industry. The advancement in additive manufacturing paves the way for new materials to develop noise reduction technologies. This document aims to apply the use of 3D-printed acoustic metamaterials for tackling fan noise emissions.

This work focuses on developing metamaterials based on coupled resonators. A detailed numerical investigation on the absorptive performances of a first geometry is carried out with an emphasis on predicting the viscothermal losses which are crucial in this application. The periodic nature of this geometry (unit cells composed of spherical cavities interlinked by cylindrical openings) is found to be well reproduced by additive manufacturing. The resultant microporosity of these printed structures causes deviations with the numerical predictions of their acoustic performance. Therefore, further development in designing low frequency high absorptive structures using more controlled techniques is explored.

A second configuration composed of multilayered plates is considered. This system exhibits multiple band gaps with subwavelength absorptive behaviour for a sample being 0.04λ thick. The repeating cellular structure enables efficiencies in the viscothermal modelling with the use of the transfer matrix approach. For further modelling efficiencies reduced order modelling is used to approximate losses in the gaps between plates. The absorptive results are evaluated against full viscothermal models and experimental measurements which show good agreements.

The satisfactory results obtained formed the basis to design more complex multilayered plate structures with acoustic resonances acting in parallel which lowered the first resonant frequency peak below 500 Hz and a broader absorption spectrum.

To my very dear Papa.

Fais de ta vie un rêve, et d'un rêve, une réalité.
Antoine de Saint-Exupéry

Acknowledgements

Most importantly, I wish to thank my father for his love, support and unconditional faith in my abilities. I would not have chosen this path had you not pushed me to do it and I thank you. Thank you to my mother, Aymeric, Mamie and Parrain. Vous êtes mon premier soutien et les personnes qui comptent le plus au monde.

I would like to thank my supervisor Henry Rice for his good humour, support and guidance over the last three years and for allowing me to be involved in very interesting activities. Also, thank you to John Kennedy for his constant support and reassuring words in moments of self-doubt.

This PhD was partially funded through the AERIALIST project no: 723367 EU H2020-EU.3.4. through which I'm grateful to have worked with many talented individuals. Luke the AERIALIST adventure would not have been the same without you. To the researchers in Le Mans, especially Thomas Humbert and Yves Aurégan, I would like to thank you for the interest you carried in our project and you enthusiasm for acoustics.

Thank you to Garret O'Donnell and Craig Meskell who enrolled me on the PhD path. Thank you Mick and Alex for your assistance with manufacturing difficulties. Merci Raphael pour tes relectures et tes encouragements constants. To all the acoustic guys in Parsons Eoghan, Kelvin, Robiul and Agnieszka thanks for your friendship and support!

Luc, je te remercie pour l'amitié que nous partageons que je pense si belle et unique. Merci aussi à Clémence, Valérie et Georges pour le soutien que vous m'avez témoigné et le réconfort que vous m'avez apporté. Je pense que sans le cabinet Dikansky et ses collaborateurs la thèse n'aurait peut-être pas eu de fin, donc merci à vous tous pour cette ambiance de travail chaleureuse.

Finally I want to thank my long time friends especially Laura, Molly and Sara for their support and belief. You have always helped me through difficult challenges. This year has been the most challenging I will ever face as you all know Papa is the closest person I will ever have. Thank you for always being there being for me.

List of publications

The following is a list of key publications associated with this work.

- Daniel Deery, Lara Flanagan, Gordon O'Brien, Henry Rice and John Kennedy, " Efficient modelling of acoustic metamaterials for the performance enhancement of an automotive silencer" (Preprint submitted to Journal of Sound and Vibration September 21, 2021)

- Giorgio Palma, Lara Flanagan, Lorenzo Burghignoli, Francesco Centracchio, John Kennedy and Umberto Iemma, "Numerical and Experimental Investigation of a Phase Gradient Metasurface Lining." (In draft)

- Flanagan L, Heaphy D, Kennedy J, Leiba R, Rice H. Development of acoustic "meta-liners" providing sub-wavelength absorption. International Journal of Aeroacoustics. 2020;19(6-8):310-323. doi:10.1177/1475472X20954894

- John Kennedy, Lara Flanagan, Luke Dowling, G. J. Bennett, Henry Rice, and Daniel Trimble, "The Influence of Additive Manufacturing Processes on the Performance of a Periodic Acoustic Metamaterial," International Journal of Polymer Science, vol. 2019, Article ID 7029143, 11 pages, 2019. https://doi.org/10.1155/2019/7029143.

List of conference presentations

The following is a list of conference and workshop presentations associated with this work.

- Flanagan, L., 'Sub-wavelength acoustic liner via "metamaterials", AIAA/CEAS Aeroacoustics Workshop, September 26^{th} – 27^{th}, 2019, Rome
- Flanagan, L., 2019, 'Numerical methods to simulate the behaviour of 3D printed acoustic metamaterials', International Graduate Summer School in Aeronautics and Astronautics, Beihang University, Beijing, China, 2-10 July 2019
- Dowling, L., Flanagan, L., 2019, 'The influence of additive manufacturing on the performance of acoustic metamaterials', DENORMS Industrial days on new acoustic treatments, acoustic metamaterials and sonic crystals, Athens, Greece, 28-1 March 2019
- Dowling, L., Flanagan, L., Rice, H., Trimble, D., Kennedy, J., 2018, 'The use of a benchmark periodic metamaterial to inform numerical modelling and additive manufacturing approaches', International Conference on Noise and Vibration Engineering, Leuven, Belgium, 17-19 September 2018
- Dowling, L., Mao, H., Flanagan, L., Kennedy, J., Rice, H., Trimble, D., Goransson, P., 2018, 'A combined design-manufacturing-testing investigation of micro- to macro-scale tailoring of open poroelastic materials based on perturbed kelvin cell micro-geometries', International Conference on Noise and Vibration Engineering, Leuven, Belgium, 17-19 September 2018

Contents

List of Figures

List of Tables

Chapter 1

Introduction

1.1 Context and research motivation

Aircraft noise is one of the most damaging environmental impacts of aviation. It has been linked to different cardiovascular diseases as well as illnesses derived from increased levels of stress [1]. Despite the fact that aircraft have become 75% less noisy over the last 30 years, due to the ever growing amount of air traffic many EU citizens are still exposed to high noise levels [2]. In 2016, EU aviation noise rules have been applied to airports with more than 50 000 civil aircraft movements per year. These rules follow the International Civil Aviation Organisation strategy and focus on four different elements; reducing noise levels at the source through the deployment of modern aircraft, managing the land around airports in a sustainable way, adapting operational procedures to reduce the impact of noise on the ground and introducing operating restrictions (ban on night flights) [3]. Air travel has become accessible to a larger demographic due to the growth of affordable air travel, this has evidently brought about a significant increase in air traffic. Figure 1.1 highlights the increase in the number of air travel passengers in the EU between 1993 and 2015.

Figure 1.1: Increase in passenger number within the EU [3]

Recent global events linked to the coronavirus pandemic caused a worldwide air traffic suspension to confine the pandemia, this led to an overnight drastic reduction in associated aircraft noise pollution. This was meant as a temporary measure and in time the number of air travel passengers will recover. A study was carried out on a group of inhabitants exposed to aircraft noise in Krakow in 2015 measuring their diastolic blood pressure (DBP, $P < 0.05$), 75 persons from that group underwent a second observation after 4 months of air traffic restrictions due to the pandemic in

June 2020, and it was shown that their hypertension had reduced significantly (DBP, $P < 0.022$) [4]. Therefore, it remains necessary to provide aircraft noise reduction measures since there is a vested interest in public health and the environment. Other studies have been carried out which underline the health effects associated with environmental noise exposure, the World Health Organisation have highlighted noise as a cause of annoyance, sleep disruption, impaired cognitive performance, and higher stress hormone levels [5, 6]. The link between aircraft noise exposure and the increased risk of developing cardiovascular related diseases has been researched extensively. According to the HYENA (HYpertension and Exposure to Noise near Airports) study carried out around 6 major European airports, it was found that night time exposure in particular may increase the risk of hypertension in men. Hypertension is an established risk factor for the development of cardiovascular diseases [7]. Researchers from the university of Bern established that persons who are subjected to noise levels superior to 60 dB have an increased mortality risk linked to heart attacks when compared to persons subjected to 45 dB per day. The noise exposure due to aircraft was estimated by noise contours in Figure 1.2 around an European airport averaged over a day, evening and night L_{den} period as well as the number of people living in that area [2].

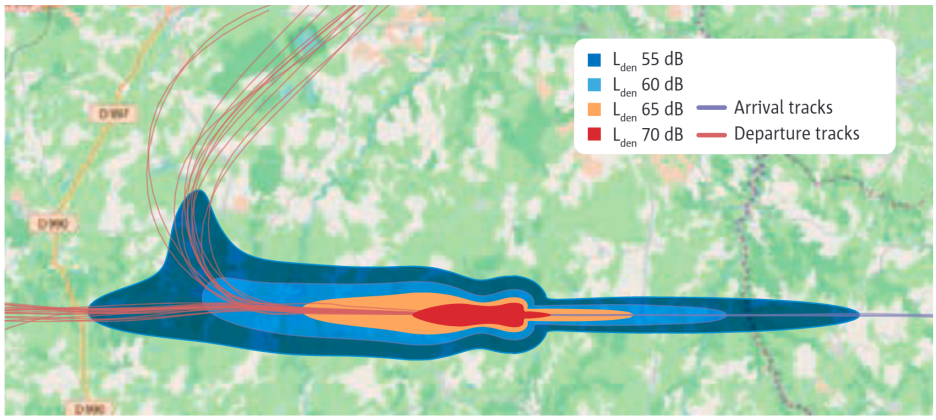

Figure 1.2: Noise footprint around an European airport. Estimated 3.44 million people inside excessive noise area by 2035 [2].

According to the STAPES (SysTem for AirPort noise Exposure Studies) model, a continued 0.1 dB reduction per annum for new aircraft deliveries would stop the growth of the overall noise exposure within the 2035 timeframe. However, without continued technological improvements for new aircraft, the population exposed to the larger L_{den} 55 dB contour could reach at minimum 2.58 million by 2035 due to densification [2].

In conventional aircraft the largest noise contributor is the turbofan engine, where the noise is primarily produced by the jet and fan. Blade design changes as well as jet flow modifications through increased bypass ratio have been used to decrease the noise levels produced. A significant portion of the noise produced during ascent and descent comes from the propulsion system. Continuing to increase the bypass ratio would result in an increased nacelle diameter. It would be heavier and also lead to spurious drag and additional weight. However, the engine nacelles act as a pillar of turbo machinery noise attenuation through traditional acoustic liners which are absorbing panels positioned in the internal walls of the nacelle [8]. A potential suitable alternative to traditional liners is emerging using metamaterials for acoustic applications in aeronautics. Metamaterials are man-made structures containing repeated cells that can operate at a sub-wavelength scale. The development of these noise alleviating structures are promising and has been aided by the emergence of new manufacturing capabilities. The advancements made in additive manufacturing has helped manufacture these components which can be tailored to a specific target application. They present an opportunity to be tuned at a low frequency of interest and their reduced volume in a nacelle is of major advantage. The space reserved for acoustic treatments in aircraft engines is restrictive so developing structures that are less bulkier than liners is significant.

1.2 Noise contributors in aircraft and mitigation strategies

Depending on the regime in which the aircraft is operating one noise source might dominate over another. Figure 1.3 presents the relative weights of noise contributors during different phases of flight.

During take-off, the combined noise from the turbofan would be dominant, whereas during descent and landing phases, the air frame noise becomes almost equivalent to the engine noise due to engine reduction. Landing gear, flaps and slat noises are predominant. Engine developments in the last decades have been produced by increasing the by-pass ratio (BPR), this has been translated by a significant reduction in jet noise. To the point which the noise contributions from what used to be minor tonal sources from the fan are now proportional to residual jet noise in the take-off regime. Even though, jet noise has been drastically reduced in modern engines, they are still a high

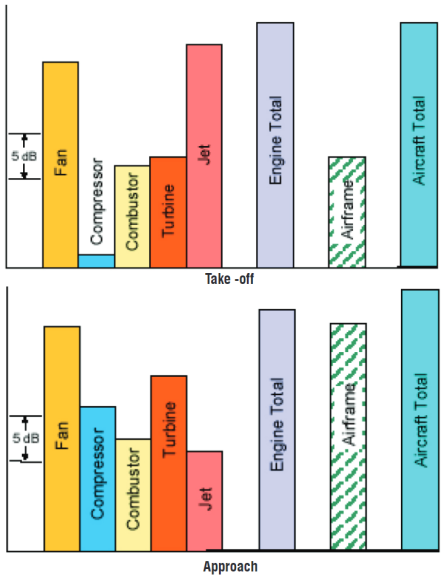

Figure 1.3: Relative weights of noise sources during take-off and landing [9].

contributor. The addition of chevrons to the trailing end of the engine nozzle reduces the pressure fluctuations through a smoother transition which also reduces the resultant noise [10]. Although, they provide additional noise reduction they increase the overall weight and drag of the aircraft. During landing the engine system reduces, and the air frame noise predominates along with contributions from the landing gear and flaps [8]. The contributing noise sources within a turbofan engine are provided in Figure 1.4. As was discussed previsouly fan noise is primarily tonal in nature whereas combustion has a broader operating bandwidth which occurs at lower frequencies. Therefore, it is of major importance to ensure noise treatments are adpated to target the source.

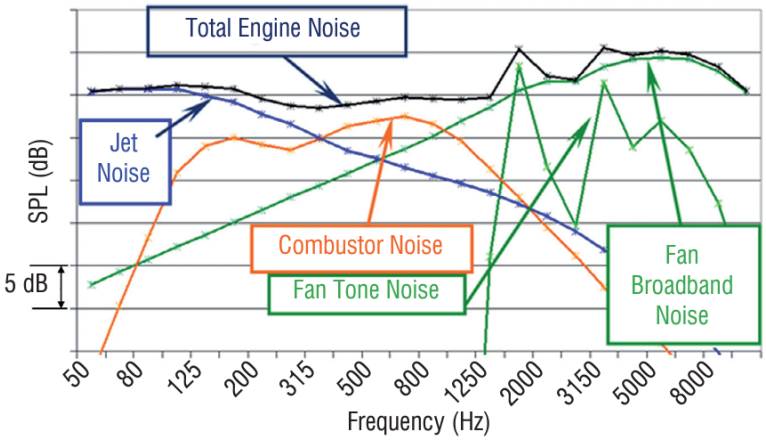

Figure 1.4: Contribution of engine noise sources on approach [11].

The nacelle possesses different functions, aerodynamic, structural, braking and aesthetic. However we are primarily interested in its acoustic function, where it attenuates the engine noise propagating within as shown in Figure 1.5. When acoustic waves propagate away from the noise generating components in an enclosed duct, the acoustic energy which strikes a boundary can result in energy loss due to absorption of the incident wave. Acoustic reflection is the resultant of impedance discontinuities, while absorption is the result of energy conversion from the incident energy on the nacelle to heat or stored energy [12]. In a quest for lighter aircraft, attempts have been made to shorten the nacelle. This has negative impacts when it comes to acoustics, where the shortened nacelle becomes less absorptive to fan and internal propagating noise since the area for acoustic treatment is reduced. Further noise reduction through acoustic liners in ultra-BPR engines is reaching its limits as the nacelle is the primary agent in reducing noise emanating from the engine's components [8].

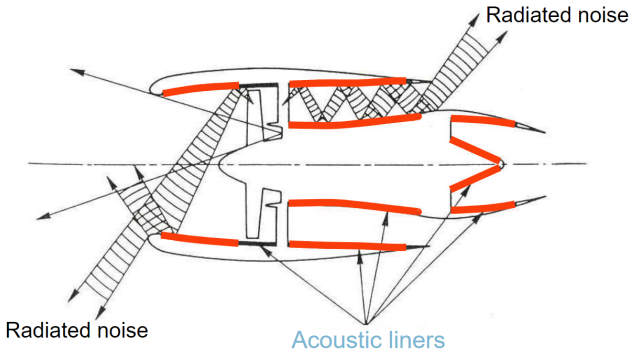

Figure 1.5: Turbofan nacelle [13].

Most acoustic liners are based on a 1 degree of freedom resonator, a common 1 DOF acoustic liner consists of an outer perforated plate backed by a honeycomb cavity based on a series of Helmholtz resonators with different tuned frequencies. They provide noise reduction over a designed frequency range, they are well suited to fan, tonal noise. Multiple degree of freedom liners can broaden the frequency range of absorption. An example of a 3 DOF honeycomb liner is presented in Figure 1.6. Optimising the noise reduction by means of extending areas where liners are placed can be efficient. A study performed by EPSL (*Ensemble Propulsif Silencieux Léger*) showed an efficient noise reduction from inlet lip treatment. However, other compatibility issues can arise in these sections that are used for anti-icing systems [14]. Other noise reducing mechanisms which do not focus on the nacelle can be developed, investigations of treating

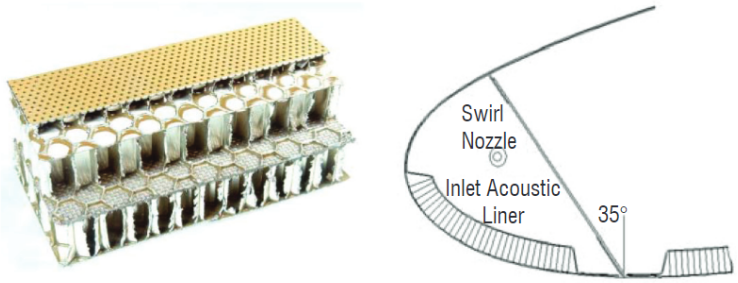

Figure 1.6: 3 DOF Honeycomb liner and added lip treatment [8].

noise by directly treating fan components, or through blade optimization have been considered [15]. However, the design change effect on the aerodynamics could affect the overall aircraft performance as they interfere with the efficiency of the engine. There are numerous different technologies which are explored when it comes to mitigating aircraft noise sources. This study will focus primarily on treatments placed within the nacelle to target fan noise. These could also potentially be expanded for use in other parts of the aircraft such as the air frame.

1.2.1 Acoustic liners

Liners are absorbing materials which assist in mitigating noise emanating from the turbofan engines. This is achieved by changing the boundary condition at the interior wall which decreases the amplitude on the incident sound wave [16]. Liners can be classified by their acoustic response to an incoming wave. Helmholtz resonator type liners are usually locally reacting, where the response is characterised by the local acoustic pressure, and not the structure of the acoustic field in the duct [17]. SDOF panels are composed of a perforated sheet, a layer composed of honeycomb-shaped cavities and a hard-backing layer. They can be modelled by a series of Helmholtz resonators where an analogy can be made with a mass-spring-damper system as in Figure 1.7. Where the air in the pore is the mass, and the cavity acts like a spring. The acoustic energy dissipates as the air is pushed back and forth through visco-thermal losses near constrictions. These losses are created by the acoustic and viscous boundary layer present on the rigid boundaries. The frequency dependent impedance can be described by the following model if all parameters are positive;

$$Z(\omega) = R + \jmath m\omega - \jmath\frac{K}{\omega} \tag{1.1}$$

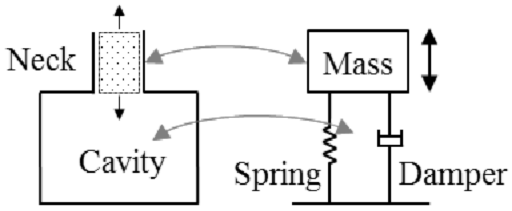

Figure 1.7: Analogy between 1 DOF acoustic liner (Helmholtz resonator) and a vibration absorber [18].

where R is obtained from the damping, m is the mass and K the spring in the system. The impedance of locally reacting liners does not depend on the incidence angle of the wave. For this reason, the characterisation usually takes place in an impedance tube without flow under normal incidence. The behaviour can become bulk reacting if the cell's dimensions are not small enough with respect to the wavelength or in the presence of drain holes where the cells become interconnected [17]. Figure 1.8 presents different types of acoustic liners used in an engine nacelle. A wire mesh can be applied on top of the perforate so the liner's behaviour is decoupled from other grazing flow effects. The superposition of two SDOF, allows for a larger frequency absorption spectrum. For example the absorption performance for a 2 DOF was shown to be effective from 800 Hz to 4000 Hz compared to 1000 Hz to 2500 Hz for a SDOF [19]. Non-locally reacting liners can be composed of a sandwiched porous material between the perforate and impervious layers. Such resulting impedances will depend on the incidence of acoustic modes [20] and will require modelling by Biot formulation [21] or an equivalent fluid model [22]. The performance of a liner is evaluated from the incoming and outgoing waves through the treated surface. The specific acoustic impedance quantifies its performance, and is defined as the ratio of the effective sound pressure acting on the surface to the particle velocity travelling through it [23]. The impedance of an array of Helmholtz resonators if the same conditions are satisfied can be defined by;

$$Z(\omega) = Z_L - \jmath \cot\left(\frac{\omega d}{c}\right) \tag{1.2}$$

where Z_L is the face-sheet impedance which is the resistive component and $-\cot\left(\frac{\omega L}{c}\right)$ is the reactance of the cavity with d the cell depth. Different constraints will guide the choice of the preferred acoustic treatment. In order to provide optimum noise reduction, the liner must be designed to target its source. It can aim at reducing specific tones or to provide a more broadband attenuation. Tools have been developed

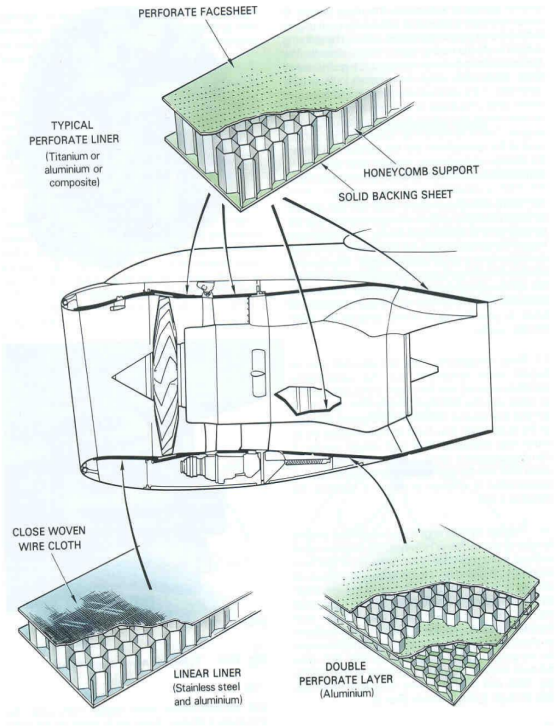

Figure 1.8: Different types of liners in a turbine engine [20].

by NASA [24] to establish the optimum impedance spectra for acoustic liners. This allows the modification of the liner's geometric parameters to produce a corresponding impedance spectra which will give maximum noise reduction. The acoustic impedance of a SDOF liner with the facing sheet resistance is described by the following formula, where the wave number $k = 2\pi f$:

$$\frac{Z}{\rho c} = R + \jmath\chi = R_{fs} + \jmath[\chi_{fs} - \cot(kd)] \tag{1.3}$$

In a SDOF liner, the absoption peaks created are narrowband where the maximum absorption occurs at the resonant frequency. The amplitude of the absorption is dependent on the designed cavity depth. The normal incidence absorption for conventional acoustic liners of different cavity depths are presented in Figure 1.9. The resistance is set at 0.5 and the reactance χ_{fs} is equivalent to kl where l is the mass inertance of 0.009. This shows the high dependency of the depth to frequency response, the resonant frequencies occur at 1440 Hz, 530 Hz, 280 Hz and 170 Hz for depths of 5 cm, 15 cm, 30 cm and 50 cm, respectively [25]. These peaks correspond to when the reactance approaches zero, which is determined by the cavity depth and wavelength. Acoustic liners contribute to an increase in the aerodynamic drag of the aircraft. From

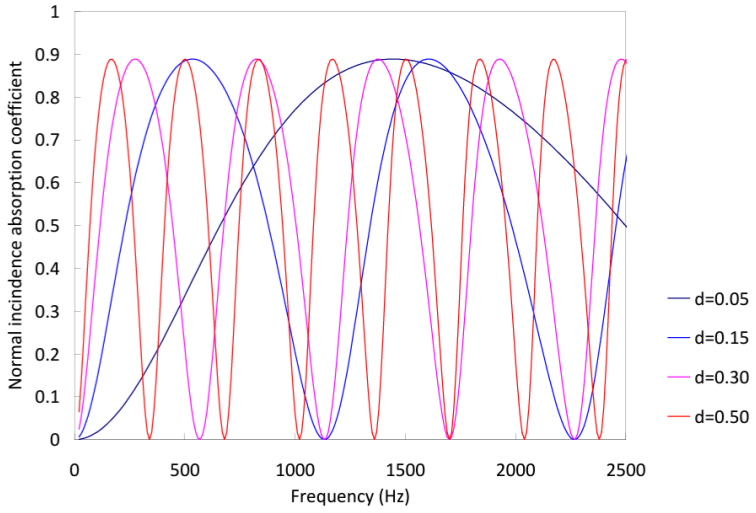

Figure 1.9: Normal incidence absorption coefficient of a convetional SDOF acoustic liners of different cavity depths d [25].

a structural viewpoint, the liner should be lightweight and minimise the space which it occupies. The flight environment also results in the liner having to withstand large temperature variations from -50°C to 180°C[26]. In this context, an objective in continued research on the topic of acoustic treatments is to provide improved performance in sound absorbing structures that are compact and lightweight while not adversely affecting the aircraft's performance. As regulations on noise reduction emanating from aircrafts become more stringent, there is motive to explore alternatives to traditional noise treatments which allow rigorous control of properties. The use of acoustic metamaterials as noise treatments has the potential to possibly bridge that gap.

1.3 The advent of metamaterials

The concept of metamaterials first emerged in the field of electromagnetics. In 1968, Veselago published his research on the propagation of electromagnetic waves in materials having negative permittivity, ϵ and permeability, k. He demonstrated analytically that a negative refractive index could be achieved if a medium displayed simultaneously negative permittivity and negative permeability [27]. It took a further three decades for this double negative condition to be experimentally proven. Pendry designed a new material as per Figure 1.10(a), composed of small conducting wires arranged in a periodic lattice which in the $\approx 10GHz$ range leads to a negative permittivity when a

wave propagates through the structure. The diameter of the conducting wires in this structure is a lot smaller than the wavelength. In a later publication [28], he devised a split ring resonator cell in Figure 1.10(b) which had the same sub-wavelength feature to obtain negative permeability. By combining the two structures in Figure 1.10 into

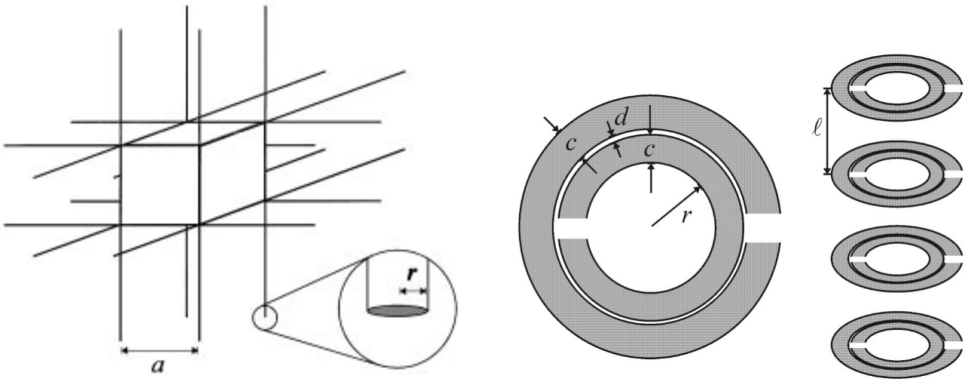

(a) Sructure of infinite wires arranged in a periodic lattice that exhibit negative permittivity in the microwave range [29].

(b) Split ring resonator exhibiting negative permeability [28]

Figure 1.10: Electromagnetic unit cells designed by Pendry which influence a) the electric field; b) the magnetic field

a metacell, it was possible to obtain a material which exhibits negative permeability and permittivity for electromagnetic waves in the microwave region [30]. Applying this concept of negative refractive index material he produced a "superlens" capable of focusing light to a point much smaller than its wavelength [31], thus overcoming the diffraction limit [32]. The particularity of metamaterials in comparison to phononic crystals is that their wavelength at the resonant frequency can be orders of magnitude larger than the geometric dimension of the cell. The advent of metamaterials settled the size problem of phononic crystals where the structure and wavelength were of the same order [33]. Wieglhofer and Lakhtakia defined metamaterials as "macroscopic composites having a man-made three-dimensional, periodic cellular architecture designed to produce an optimised combination not available in nature of two or more responses to a specific excitation" [34]. An extension of this was provided by Cui et al, as "a composite of periodic or non-periodic structures whose function is due to both its cellular architecture and chemical composition" [35]. In addition, the wavelength can be orders of magnitude larger than the dimension of the cellular structure [36]. A number of observed characteristics continue to complement the original definition. As part of the EU H2020 funded AERIALIST project, the following general description

for metamaterials in the field of acoustics is accepted; "A metamaterial is a human-made compound, a structured material engineered to achieve a response not available in nature and for which the model of an equivalent continuum can be defined" [37].

1.4 Acoustic Metamaterials

Originally discovered in the field of electromagnetics, the disruptive nature of metamaterials which allows the control of waves in a manner that is not possible in conventional materials sparked interest within researchers involved in acoustics. The following section will focus on potential applications of metamaterials to control airborne sound. Acoustic metamaterials are used to control sound propagation, important constitutive parameters are key to design these metamaterials. Acoustic waves are governed by Newton's law of motion, continuity and energy equations for adiabatic processes. The equation which describes the propagation of sound waves in a homogeneous fluid without sources can be described by the following;

$$\nabla^2 p - \frac{\rho}{B}\frac{\delta^2 p}{\delta t^2} = 0 \tag{1.4}$$

where p is acoustic pressure and the two material parameters are the mass density ρ and the bulk modulus B. The speed of sound is given by $c = \sqrt{B/\rho}$. In acoustic metamaterials, the effective parameters can be negative which results in unconventional wave characteristics. An analogy with electromagnetics described in the previous section can be made, as their wave equations have the same mathematical form. Electromagnetic waves are transverse vector waves whereas acoustic waves are scalar longitudinal waves [36]. The effective parameters in electromagnetics and acoustics can be related by $\epsilon \rightarrow \rho$ and $k^{-1} \rightarrow B$. Unlike ordinary materials who have positive effective parameters, acoustic metamaterials can exhibit negative mass density or bulk modulus or possess a double negative. The following sections will highlight different capabilities of acoustic metamaterials by classifying them according to their metabehaviour. Liu et al. designed the first acoustic metamaterial which incorporates local resonances. It is made up of a microstructure consisting of a solid core material of relatively high density and a coating of elastically soft material shown in Figure 1.11 [38]. This metamaterial was found effective for noise attenuation in the mid-frequency range. A slab of 2 cm of this material provides a 60 dB sound isolation at 400 Hz. The frequency resonances

are provided by the motion of the solid metallic core at 400 Hz and at 1350 Hz by that of the silicone rubber coating. The value of mass density becomes negative close to the resonances. In 2006, Fang et al. created an ultrasonic metamaterial based on a chain of

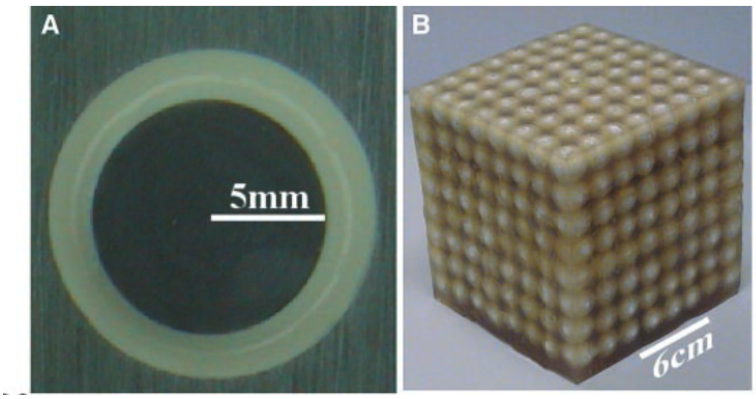

Figure 1.11: (A) Cross section of a coated lead sphere of the unit structure (B)8×8×8 sonic crystal of this unit with a lattice constant much smaller than the wavelength [38].

sub-wavelength Helmholtz resonators which achieves a negative effective bulk modulus close to the resonant frequencies [39]. Compared to the previous design mentioned, it does not rely on a change in material but in a geometric change which limits the propagation in the fluid. The change in volume of the cavity shown in Figure 1.12(a) modifies its resonant frequency. Combining an array of open-sided Helmholtz resonators in a waveguide produces lower resonant frequencies, and a negative bulk modulus can be observed. The bulk modulus becomes negative in the region of 35 kHz, the group velocity which follows the direction of the energy flux is anti-parallel to the direction of phase propagation. It was demonstrated that depending on the type of spatial sym-

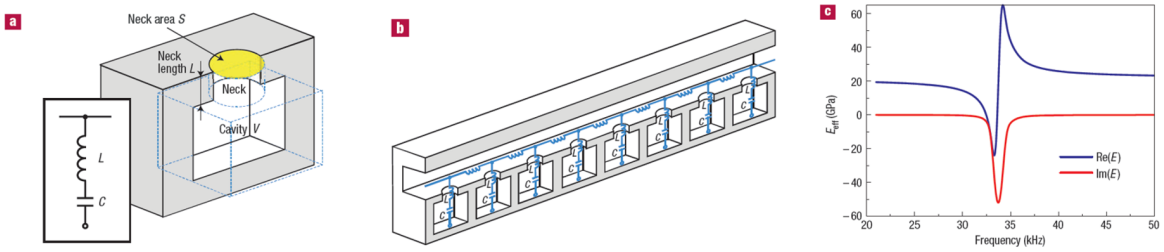

Figure 1.12: (a) Cross section of Helmholtz resonator of cavity 3.14×4×5 mm and neck 1 mm long and 1 mm diameter (b) waveguide loaded with a series of Helmholtz resonators connected by a channel (c) calculated effective bulk modulus for the 1-d array of Helmholtz resonators [39].

metry of the resonant modes, whether dipolar or monopolar, either the mass density or bulk modulus will be dispersive [40]. Modes with dipolar symmetry contribute to an inertial response whereas modes with monopolar symmetry produce a bulk modulus type response. Li and Chan theoretically illustrated this double negative concept in the context of Mie resonances of soft rubber spheres [41]. By superimposing the frequency response of these two modes with differing spatial symmetry, it is possible to obtain acoustic materials exhibiting dispersive effective parameters which turn negative within the same frequency range. There are different possible approaches to achieve double negativity. It can be achieved by using a single resonator with eigenmodes of differing symmetries which result in a negative mass density and bulk modulus. Or by creating two resonating structures, each having a different type of spatial symmetry [36]. A successful experimental characterisation of this double negativity was carried out by Lee et al. [42] using a combination of structures outlined in Figure 1.13. Frequency dispersion in the mass density is generated in a waveguide by an array of thin elastic membranes shown in Figure 1.13 (a). The metamaterial composed of an array of side holes in a waveguide displayed in Figure 1.13 (b) exhibits a negative effective modulus in a frequency range from 0 to 450 Hz. The superposition of the two dispersive

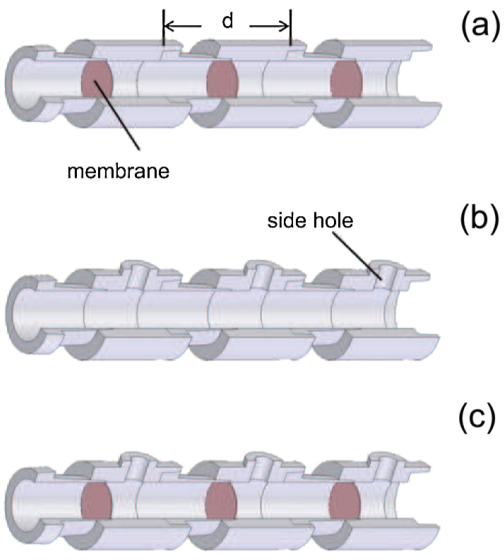

Figure 1.13: Three connected unit cells (a) Cross section of the thin membrane structure [43] (b) Cross section of metamaterial with connecting side holes [44] (c) Composite structure of (a) and (b) resulting in double negativity [42].

frequency ranges results in double negativity between 240 Hz and 450 Hz where the material is transparent. This type of material leads to potential application for super-

lenses and acoustic cloaking [42]. Acoustic metamaterials composed of different types of constitutive parameters of the material parameter space have been presented. Other potential applications more specifically applicable to aeroacoustics will be presented in the subsequent sub-sections according to the effect produced in the acoustic field. Some of these structures may exhibit multiple metabehaviours that show promise in reducing noise emanating from the aircraft.

1.4.1 Absorption

Absorption refers to the conversion of sound wave energy into a different form. To achieve optimal absorption performance, the system should be dissipative, this can be achieved through friction [36] and many porous materials are effective as sound absorbing structures [45]. The coupling between the incident wave energy and the acoustic absorber is also important to obtain good performance. A gradient index method for impedance matching may be used to achieve this. An example of such device which consists of an absorbing layer and a periodic array of solid tubes, with their filling density varying from the open air facing the external row, to the internal row which faces the porous absorptive layer is presented in [46]. This material is used to adjust the impedance of the air to that of the porous absorptive layer, consequently reducing the reflection. This study highlights the importance of impedance matching to obtain maximal absorption, in this case between the impedance at the exit of the metamaterial layer to the porous layer. However, when it comes to absorption at low-frequency it is not always effective. Adding a lot of absorptive material for low-frequency noise is impractical as the thickness could be of the order of several wavelengths. Therefore, to enhance absorption at low-frequency it is necessary to increase the energy density inside the material by use of resonances. The perspective of using sub-wavelength acoustic metamaterials with good absorptive performance is promising. An example of a decorated membrane resonator designed by Mei et al. [47] shown in Figure 1.14 (a) composed of an elastic membrane decorated with asymmetric rigid platelets displays good absorptive performance at frequencies ranging from 100 – 1000 Hz. The working principle of this high absorption device is created by the flapping motion of the platelets due to enhanced energy concentration at discontinuities within the perimeter region of the platelets. By increasing the width of the unit from 30 mm to 160 mm, the perfor-

mance of this modified membrane in Figure 1.14 (c) reaches close to unity absorption at frequencies where the relevant wavelength is three orders of magnitude larger than the membrane thickness. The addition of an orifice to a membrane ring structure was proposed by Chen et al. [48] in Figure 1.14 (d), this creates an extra transmission loss peak compared with the one produced from a membrane-ring structure. It is possible to tailor their frequencies by varying orifice or ring diameter, the sound reduction is due to the anti-resonance behaviour of the structure. The performance of this metamaterial backed by an air cavity was also assessed. In the case of a ventilated resonator with a two membrane structure, multiple peaks in transmission loss profiles were observed at low frequency. This type of structure offers noise reduction at low-frequency and can be used in ducts or ventilated systems. Another acoustic metamaterial design

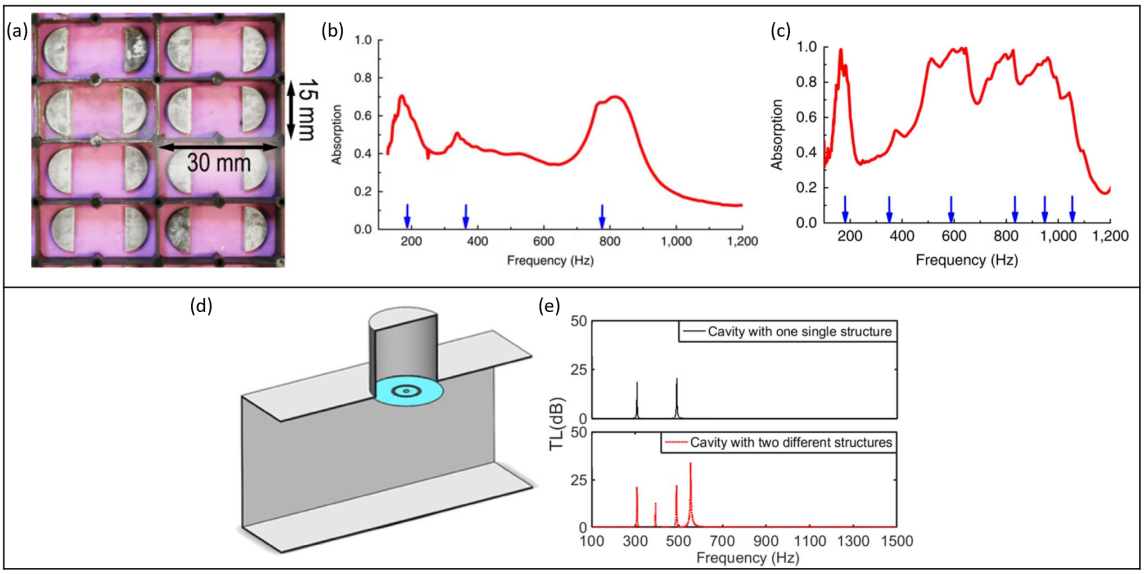

Figure 1.14: (a) Image of Elastic membrane decorated with asymmetric rigid platelets which induce a flapping motion. (b) Measured absorption coefficient and the positions of the numerically predicted absorption peak frequencies (blue arrows). (c) Measured absorption of modified decorated membrane (160 mm× 15 mm) which shows near-unity absorption of the low-frequency sound at multiple numerically predicted frequencies [47]. (d) Cutoff drawing of a ventilated composite resonator. (e) TL spectra of ventilated resonator composed of one membrane-ring-orifice structure and two different membrane-ring-orifice resonators [48].

which makes use of viscous dissipation and resonances to provide low-frequency sound absorption was put forward by Tang et al. [49]. It is composed of a microperforated panel, a honeycomb corrugation core which is also perforated and a facesheet on the

bottom. The design produces a series of different Helmholtz resonators comprised of narrow perforations and the cavity behind. When the resonant frequency is reached, the variations in acoustic pressure variations within the cavity causes the air to oscillate in and out of the perforation, dissipating energy through the viscous boundary layer at the perforations. The metamaterial provides low-frequency high broadband absorption as well as good mechanical performance. There is an emphasis within the research community to continue to develop low-frequency broadband absorptive structures for aeroacoutic applications,through modified liners [50], resonators in parallel [51, 52] and combining multiple single-resonant systems [53].

1.4.2 Space coiling and metasurfaces

Space-coiling metamaterials have shown some interesting reflective behaviour. Figure

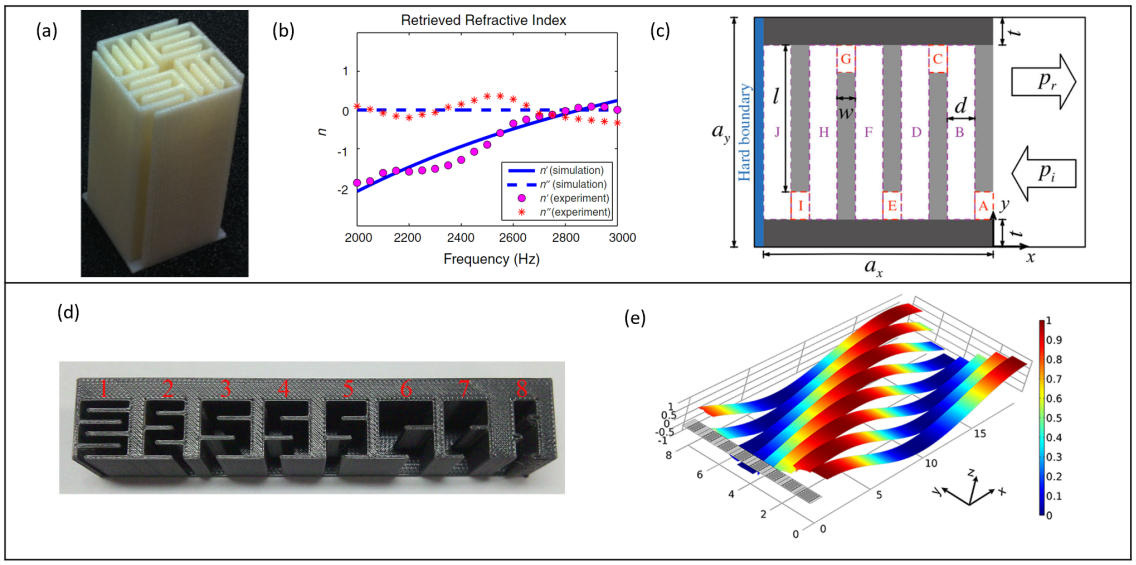

Figure 1.15: (a) Photograph of 3D printed labyrinthine unit cell designed by Xie et al. [54] (b) Retrieved refractive index of labyrinthine unit cell from experiment (pink circles for real part, red asterisks for imaginary part) and from simulation (solid blue line for real part, dashed blue line for imaginary part) [54] (c) Labyrinthine unit cell (width ax and height ay), composed of several identical cross arranged plates (width w and length l) that form a labyrinthine channel of width d. Top and bottom top plates (thickness t) used to seal the channels in the y direction. [55]. (d) Photo of the eight labyrinthine units which can provide phase shifts up to 2π with a step of $\pi/4$ [55]. (e) The pressure strips of the reflected waves by the eight units which shows the different phase shifts corresponding to each unit [56].

1.15 (a) shows a complex labyrinthine unit cell put forward by Xie et al. [54], its

channels are deep subwavelength in their cross-sections. The resonating nature of this metamaterial results from the space folding inside the unit cell rather than from local resonances. The structure forces the wave to travel inside the folded channels that is achieved through the tortuosity within the design, the path length of the wave to be multiplied. The negative refractive index obtained has a much broader frequency range (1000 Hz) shown in Figure 1.15 (b) due to its resonating nature. It is possible to tune the dispersive characteristics of the metamaterial by adjusting the channel length in the unit cell. This metamaterial constrains the acoustic wave to propagate within the channels, these are much longer than their external dimension. The coiled-up channel leads to a large phase delay. A space-coiled, pie-wedge shaped cylindrical metamaterial was designed by Cheng et al. [57]. The serpentine air channel gives the unit cell a high effective index, exhibiting multiple Mie resonances either with negative mass density or bulk modulus. Its single-negative nature is used to obtain large scattering cross-section with high reflectance for low-frequency sound [36, 57]. A metamaterial which possesses a thickness, $1/10^{\text{th}}$ of its operating wavelength is defined as a metasurface [37]. In aeroacoustic applications, the working space is quite limited for noise treatment so there is an incentive to develop such thin structures. A metasurface constructed of a unit composed of cross arranged plates to form a labyrinthine channel, sealed by a top and bottom plate with a hard backing is show in Figure 1.15(c). This structure proposed by Li et al. [56], introduces a phase shift to the reflected field after the incident wave navigates through the coiled channel. The phase of the reflected field can be controlled by selecting the geometrical dimensions of the unit. Up to 2π is provided across the layer. Eight units of the corrugated plate configuration shown in Figure 1.15 (d) were used to provide discreet phase shifts in steps of $\pi/4$. The reflected waves by these eight units can be seen in Figure 1.15 (e). This design was verified experimentally, where the same interesting characteristics could be observed such as scattering of waves with unusual reflection and refraction angles [55]. However, there can be some impedance mismatch to the incident wave with these space coiling structures [58].

1.4.3 Cloaking

Theoretical demonstration by Pendry et al. [59] have shown that electromagnetic waves can be concealed by cloaking the object with a metamaterial, it deflects the waves that would have struck it and redirects them around the object so that they return to their original trajectory. The example of a cloaked sphere was used, the rays are bent around the sphere, rapid changes in the effective parameters are sensed by the waves. The medium is compressed anisotropically [36]. The distortion of the field is represented as a coordinate transformation, that is used to generate values of permittivity and permeability which ensures that Maxwell's equations are satisfied [59]. Cummer and Schurig showed that there is an exact equivalence between the acoustic equations in two dimensional geometry and the Maxwell equations for anisotropic materials [60]. The same cloaking shell as in [59] is used, which results in an acoustic cloak with the following characteristics: inhomogeneous bulk modulus and an anisotropic and inhomogeneous mass density. The type of cloaking discovered by Pendry is referred to as inertial cloaking, the material exhibits anisotropic density and gives rise to a very large device [61]. Acoustic anisotropy is not observed in natural materials, a tensorial mass density is required, meaning that the force per unit volume is not necessarily aligned with the particle acceleration. Anisotropy can be dispersed between mass density and bulk modulus. Norris showed that perfect cloaking can be obtained with finite mass by using anisotropic stiffness. This class of material is referred to as a pentamode material [62]. A pentamode metamaterial has a solid structure but essentially behaves as a fluid, where five of the six modes are soft and one is stiff. They have advantages over inertial cloaking materials, cylindrical or spherical cloaks with isotropic density can be obtained where the total cloak mass is the original mass of the virtual region [61]. Successful manufacture is a challenge, lattices need to have thin members which are flexible in bending and stiff in compression. A successful structure engineered by Bückmann et al. [63] based on pentamode metamaterials is shown in Figure 1.16.

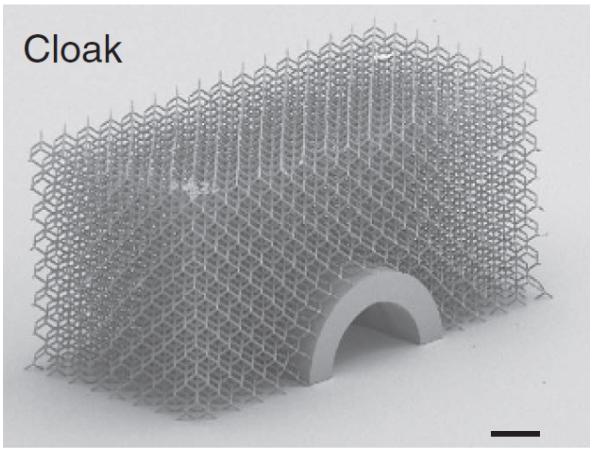

Figure 1.16: Rigid hollow cylinder and cloaking shell, Black scale bar, 200 mm [63].

1.5 Adaptability of of acoustic metamaterials

Although the metamaterials presented above have exciting capabilities, once the structure concept is designed it will be characterised by its passive performance. The possibility of tuning a device to broaden its range of application, without the need to fabricate new samples for different target applications is of major interest. The ability to reconfigure metamaterials is an exciting prospect, and the use of nonlinear processes, piezoelectric elements and powered devices have been exploited to obtain reconfigurable acoustic metamaterials [36]. Furthermore the inherent presence of losses impacts on the efficiency of passive metamaterials. In the case of sound propagation in metamaterials with resonant inclusions, the energy is ultimately dissipated through viscous action. The effective fluid properties then limits the range of applications of such metamaterials. An example of an external control active metamaterial presented in [64] uses a pneumatic actuation system to vary the pressure behind the pistons inside each cell, thus changing the cavity depth of the Helmholtz type resonator. The change in pressure shifts the acoustic band gap. By tuning different cells with different pressures, it would be possible to obtain an attenuation over a broader range of frequencies.

1.6 Overview of manufacturing technologies

While a wide range of sound absorbing structures can be manufactured using traditional manufacturing methods such as milling, drilling and fabrication of sheet components. Traditional manufacturing processes cannot provide automated solutions to manufac-

ture nanoscale and macroscale features in a unit cell or the alignment of these cells in 3D across large volumes [65]. As mentioned in Section 1.5, additive manufacturing has enabled to design some metamerials that could not be achieved using traditional methods. Currently, 3D printing is a method for producing acoustic metamaterials which is receiving considerable attention. Not withstanding, 3D printing may generally not be sustainable for mass production particularly from a time-consumption viewpoint.

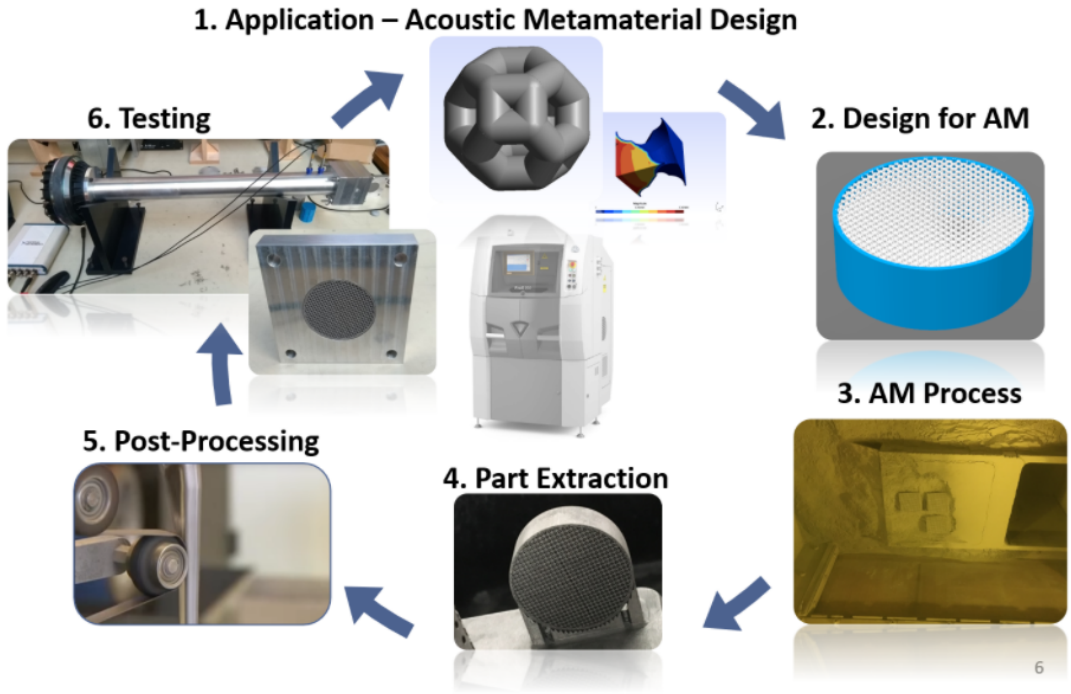

Figure 1.17: Design process for additive manufacturing of acoustic metamaterials [66].

Figure 1.17 demonstrates the design cycle of a 3D printed acoustic metamaterial. From its conceptualisation through computer-aided design, the component is initially modelled as a mesh file composed of triangular elements. This allows an interpretive printing software to perform the slicing and produce a "G-code" containing the 3D printer pathway. In this orientation and supports that are needed for the print must also be modelled. The nature of the layer by layer process and the resolution of each layer step creates a staircase phenomenon, which can affect the quality of the produced part. Consideration of the minimum feature size is critical. To minimise the staircase effect it is important to use a printer which exhibits a layer thickness of a much smaller

scale than the desired feature size [67]. Figure 1.18 highlights some of the effects

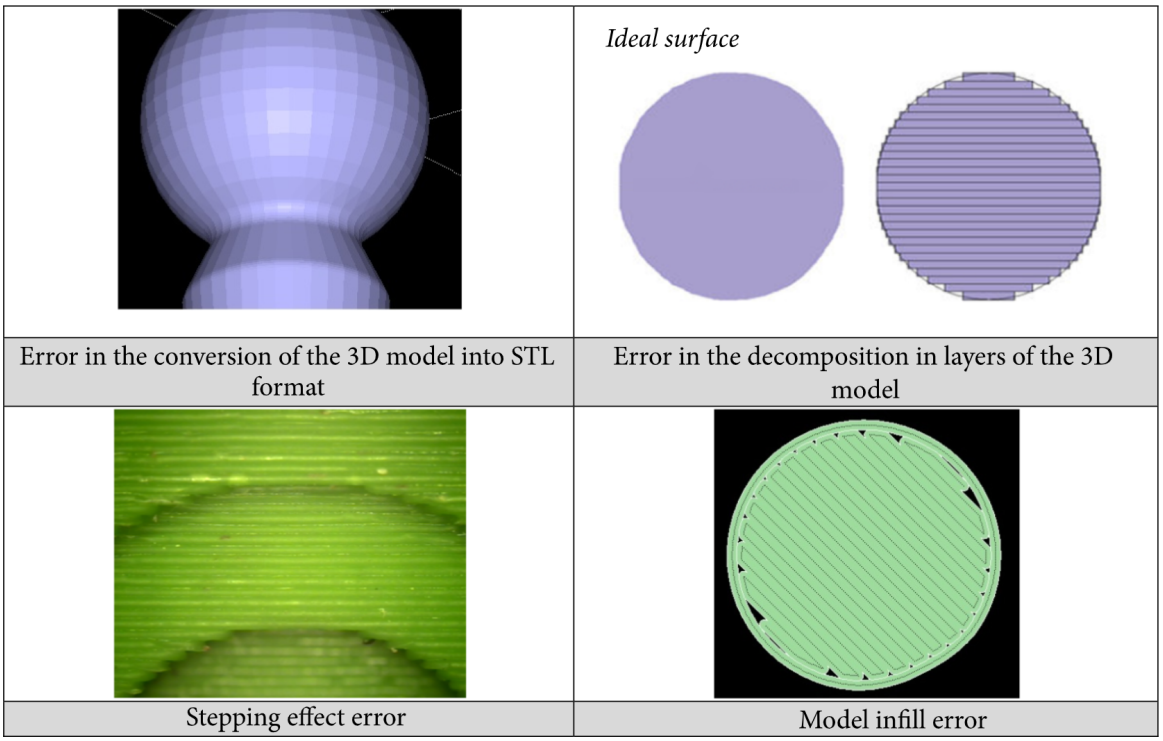

Figure 1.18: Effects which affect the fidelity of the print [68].

that can be encountered in this process including coarser elements during the CAD conversion, a layer thickness decomposition error, the staircase effect, and a model infill error. Ultimately an STL file is an approximation of the designed part as the discreet nature of the mesh causes issues in approximating curved surfaces. Thus, deviations in the final part should be expected. The quality of the STL file produced can generally be improved by discretizing the object with a higher number of elements [69]. Following the manufacturing, some cleaning including removal of supports and post-processing of the part are required depending on the print technology used. A range of additive manufacturing processes used in this work are briefly described below. Each technology provides different capabilities in terms of materials, resolution and build volumes.

1.6.1 Fused Deposition Modelling (FDM)

Most low-cost 3D printers are filament based, in this process a thin thermoplastic filament is extruded. The nozzle extrudes the molten plastic and the material is deposited on the build plate or on the preceding layer of material, following the layer pattern

determined by the slicing software. The build plate is cooled by fans to allow for the deposited layers to solidify. With this type of technology the nozzle extrudes the material in a thickness typically of 0.25 mm [70], therefore the resolution could be insufficient for small feature sizes which are characteristic of metamaterials. Although the resolution remains one of this technology's main disadvantage, it is the least expensive and no chemical post-processing is required [70]. The manufacturing is governed by the infill factor and the diameter nozzle, the density of the filament pattern will influence the mechanical properties of the produced part. Small filaments can also subside outside the 3D printed volume which may impact the acoustic performance.

1.6.2 Stereolithography (SLA) and Direct Light Processing (DLP)

In both SLA and DLP, a build platform is lowered into a resin reservoir. However the curing mechanism differs. With SLA, a UV laser traces over the cross-section predefined by the slicing software. Photopolymerisation occurs, transforming the liquid monomer into a solid polymer. The solidified material matches the cross-section of the part at that layer. The build platform is raised from the resin reservoir and the resin is stirred to give a new even spread of resin. The process is repeated until the part is finished. DLP is Similar to SLA, a build platform is lowered into a resin reservoir. However, a UV flash bulb is used to light up a LCD screen which uses pixels to create a map of the cross section for the layers [71]. A DLP printer produces smooth flat surfaces, but on curved surfaces it will produce a staircase effect. The light source used in DLP remains fixed therefore it will cure the entire layer which increases the speed of production of the part.

1.6.3 Selective laser melting (SLM)

Selective laser melting is a powder bed fusion process where the metallic powdered material is fully melted using a laser or an electron beam. Comparable to the other additive technologies, it applies a layer by layer approach whereby an electron beam or laser spot rapidly heats the pre-determined cross-section obtained from the slicing software to the material's melting temperature. The powder melts to form a melt pool which solidifies and cools down rapidly. Once the layer is solidified, the platform is lowered by the slicing distance and a new layer of powder is deposited. This process is

repeated until the part is completed [71]. A significant number of process parameters which occur at different stages of the building process can have an impact on the produced part such as the laser beam size, laser power, laser scan speed, and powder layer thickness [72].

1.6.4 Observed differences between additive techniques

For a particular structure there are varying differences between some additive manufacturing technologies. Microscopy images of a structure using different additive technologies discussed previously are presented in Figure 1.19 with information on the dimensional accuracy of holes. The FDM sample in Figure 1.19 exhibits some filaments across the cylindrical opening which are elliptical shaped instead of circular. This also represents the most economical technology, the printer used for Figure 1.19 (a) is a FDM Ultimaker which costs approximately € 3000. The other three technologies show a higher fidelity of the cylindrical shaped opening. DLP technology relies on pixel controlled granularity which causes a layer step effect. This is visible in the DLP sample in [53]. This effect increases the surface roughness of the part. Each technology presents its own characteristic defects. However there are disadvantages to printing periodic metamaterials. Depending on the technology chosen, there can be internal residual material which may be difficult to remove. With a SLA print, the resin can become entrapped within the channels even though cleaning is performed post-curing as SLA and DLP use photopolymers. The SLA printer used to manufacture the sample in Figure 1.19 (c) is a mid range desktop machine, the Formlabs Form 2 printer costs € 5000 by comparison. The deeper the material and length of the channels the more difficult it can be to remove the resin [53]. The DLP prints have similar constraints however, the viscosity of the resin used is a lot lower and therefore it is easier to remove it. Inspection on manufactured samples allow to see whether the print failed. This can be the result of blocked channels, warping, disconnections or damage, the extent of these will determine how to manufacture the replacing print. The resolution of the feature size of SLA and SLM technologies is dependent on the laser spot size and its path. These technologies possess smoother printed parts. The SLM printer used to manufacture the sample in Figure 1.19 (d) is the 3D Systems Prox DMP 200 which costs approximately € 450 000. This achieves the smoothest

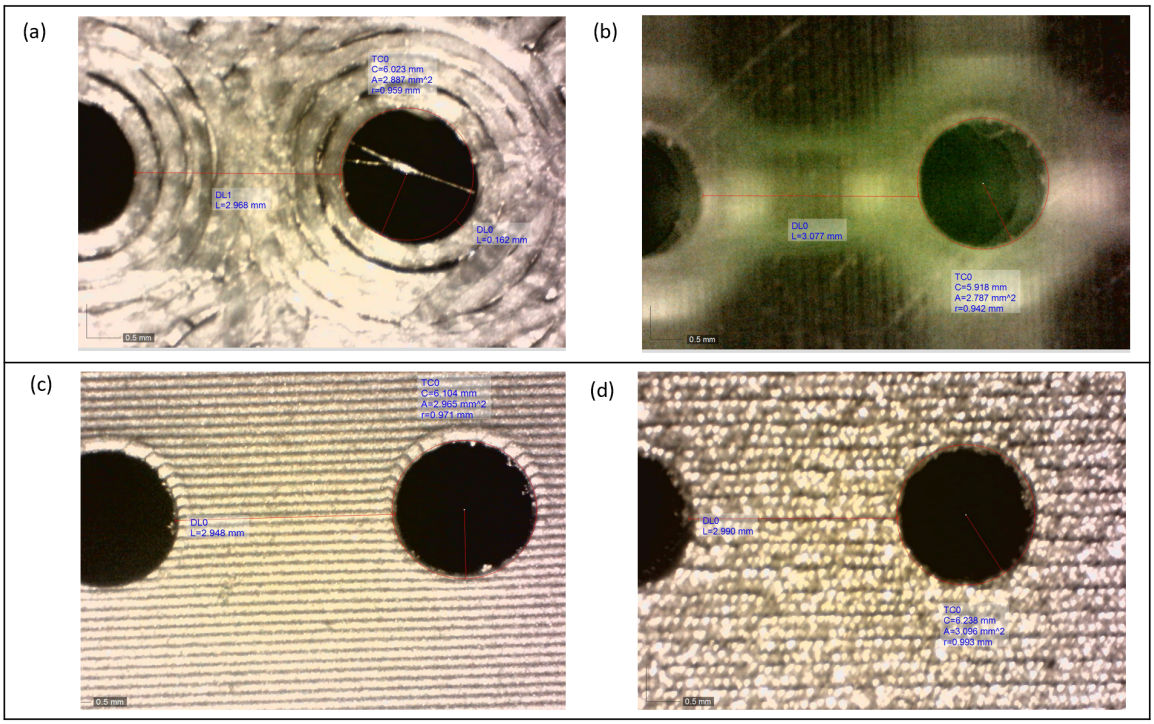

Figure 1.19: Microscopy images using a Leica S6E under 56x magnification of different printing processes; (a) FDM,(b) DLP, (c) SLA and (d) SLM used [53].

print with the highest resolution and closest to the ideal structure [53]. A review by Dowling et al. [72] on repeatability issues in powder bed fusion describes how porosity and an uneven microstructure develops during interactions between the laser and the melt pool. During the print set-up, numerous parameters will inevitably affect the final obtained microstructure. Some post-processing can be realised to improve the mechanical properties of the produced part. A study which notifies the occurrence of porosity by a visual camera has been realised [73]. However, controlling the occurrence of surface defects by continued parametrisation during the process could greatly aid in developing printed metamaterials of high fidelity.

1.7 Conclusions and discussion

When designing acoustic metamaterials, whether fixed or active, the fabrication process used will influence the desired acoustic performance. The availability of additive manufacturing processes has enabled the realisation of complex structures, that would not have been previously conceived. The democratisation of this field has also allowed the wider research community to design structures with affordable printers. The unit

cell structure, which relies on its geometric configuration to obtain its metabehaviour, can give rise to significant complexity and to accommodate this complexity for manufacturing a physical system, a suitable additive printing process is frequently required. Even with these processes, it can be challenging to realise the desired part due to issues inherent to the manufacturing such as micro-porosity, layer depth and nozzle resolution. These can lead to some discrepancy between the designed and produced part without reasonable quality checks. The numerous types of 3D printing technologies such as FDM, SLA, SLM all possess different resolution, and within these technologies the prints are greatly affected by the quality of the printer itself as its characteristics are also cost-dependent. The aerospace industry is assessing the potential use of acoustic metamaterials as noise mitigation components and through the range of potential materials offered by additive manufacturing, it may be possible to obtain lighter and durable components which are critical in that sector. While additive manufacturing has streamlined the manufacturing process, there is a larger dimensional tolerance to account for, compared with traditional methods. Even though there are current limitations with the fidelity of produced parts via additive manufacturing, as the technology becomes more widely available it is a relatively inexpensive tool available to develop acoustic metamaterials. The issues which arise during the printing process can be difficult to incorporate when predicting the acoustic performance of a structure. However, some surface defects such as roughness can also be advantageous to the acoustic performance of the structure by for example modifying viscous and thermal boundary effects. In conclusion, acoustic metamaterials are promising sound mitigation structures which show potential in the aeronautics field. Most of the studies realised have been under no flow conditions, which makes it difficult to assess their performance in actual environmental conditions. Observing their behaviour in such conditions it is important to validate this technology. Furthermore, the complexities associated with fabrication continues to be addressed. Designing structures which show low-frequency broadband noise attenuation which can be manufactured using more traditional methods is an important option to pursue in parallel.

1.8 Research objectives

The thesis focused on the development of efficient modelling tools to design absorptive sub-wavelength acoustic structures. It also provided a reflection on the role additive manufacturing can play in printing these components and the problematic of predicting their behaviour. This led the way to reassessing more conventional layouts and how best to exploit them. The primary aim of this study is related to developing an efficient design tool to predict losses induced by energy dissipation in sub-wavelength acoustic structures for noise mitigation purposes.
In order to achieve this, a number of objectives are established:

- Propose a validation of acoustic performance of manufactured samples using different additive printing technologies
- Develop viable macro models of built-up structures based on detailed models of the unit cell
- Propose efficient modelling techniques for microacoustics through reduced-order models which account for visco-thermal losses.
- Sensitivity analysis through parametric studies in order to achieve a low broadband frequency sub-wavelength multilayered plate structure.

1.9 Thesis Outline

In this Chapter, motivation for the project and research objectives were provided. A literature review of noise mitigating structures for aeronautical applications was also provided to contextualise the research. From the extensive literature provided, it became clear that while additive manufacturing presented an opportunity to manufacture acoustic metamaterials, it is also important to be able to predict the behaviour of the printed structure.

In Chapter 2, acoustic propagation models are presented. Modelling strategies adopted for 3D printed acoustic metamaterials are also exposed, it became evident that some defects inherent to the printing technology employed would impact on the acoustic behaviour of the designed structure. Means to account for these must be adressed.

In Chapter 3, the sound absorptive performance of a metaliner is investigated. This structure made use of a staggered pathway to enhance energy dissipation with most of the losses occurring in slits between the plates. The system presented multiple high absorptive peaks and deep sub wavelength behaviour achieved through tortuosity in the design. The acoustic performance of a single layer was obtained numerically and experimentally validated from a printed sample. Due to the repeatability of the single layer, the transfer matrix method was used to efficiently obtain the acoustic performance of a built-up structure of 5 multi-layered units.

In Chapter 4, a parametric design study of the metaliner configuration examined in Chapter 3 is presented in view of optimsing the design. Reduced order modelling was implemented to account for the losses in the system and compared with compressible linearised Navier Stokes formulation for validation. This allowed the development of an efficient design process which predicted the acoustic performance of ultilayerd plate configurations. The parametric design study paved the way to develop novel liner configurations which showed high absorption at a low broadband frequency range.

An additional discussion of the study carried out is available in Chapter 5 and concluding remarks are made in Chapter 6.

Chapter 2

Numerical prediction of printed acoustic metamaterials using viscothermal acoustics

2.1 Introduction

In this chapter, the physics governing all fluid motion of ideal fluids with small perturbations are explored. The full viscothermal acoustic formulation is described for which the Navier Stokes equations are linearised for small acoustic perturbations. Simplifications in the case of isentropic acoustics are also stated. In the case of lossy acoustics some loss approximations can be made and included in the Helmholtz equation via a complex wave number.

The following section also presents a design for an acoustic metamaterial composed of a connected network of resonant structures. The design is periodic, composed of cubes with internal spherical cavities connected by cylindrical openings on each face of the cube. The design presented in this chapter, was developed as part of the AERIALIST project no: 723367 EU H2020-EU.3.4. Societal Challenges Smart, Green And Integrated Transport. A benchmark unit cell structure is presented which has been replicated and tested by many laboratories part of the COST Action DENORMS (CA 15125) [74], whose goal is to provide a framework for efficient information exchange and channelling the work of groups involved in designing multi-functional, light and compact noise reducing treatments. Achieving structurally complex acoustic absorbers at a microscopic scale is possible in part due to the progress of additive manufacturing technologies. This design concept was first proposed by Dr. Tomasz G. Zieliński from the Institute of Fundamental Technological Research of the Polish Academy of Sciences. This design was proposed due to its potential acoustic performance and suitability to both additive manufacturing and numerical modelling. The chapter will report on the modelling strategy employed to characterise the absorptive performance of this cellular structure. And also provide experimental validation of samples obtained via different additive manufacturing technologies.

2.2 Viscothermal acoustics

Viscothermal acoustics describes the most general and complete form of acoustic propagation which can make it complex to solve. Viscothermal acoustics theory is used for acoustic propagation in small devices where the geometries are of the same scale or smaller than the viscothermal boundary layers. In some cases when the geometry per-

mits, a lossless version of the governing equations can be solved presented in 2.3.2 which provides an acoustic solution for the bulk region. In general viscothermal simulations are > 5 times heavier than isentropic acoustic simulations. Many lossy semi-analytical models can be found in the literature which are an alternative to direct implementation [75]. In a viscothermal acoustic solution, distinctions are made between the bulk and boundary layer regions as shown in Figure 2.1. Acoustic propagation in metamate-

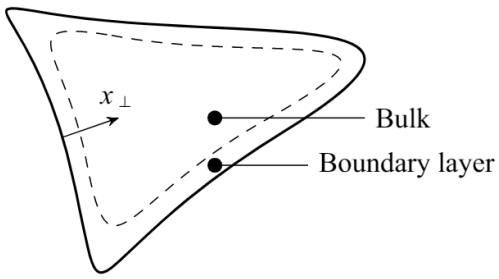

Figure 2.1: Bulk and boundary layer regions in viscothermal solution [76].

rials need to include associated entropic and vortical fields to accurately represent the acoustic behaviour [77]. In small channels the bulk may totally vanish. Also in very large domains, the boundary layer effects can be very small compared to the bulk and that region may be neglected. When waves propagate in narrow slits and tubes the thermal and viscous effects can be large and cannot be neglected. These effects become more significant near no-slip isothermal wall conditions due to the viscous shear and heat conduction that contribute to dampen the acoustic wave. This contributes to the development of the viscous and thermal boundary layers. These cause high perpendicular gradients $x_\perp$ in the shear velocity and temperature. Section 2.3.5 provides more extensive detail on these boundary layer effects and how they are quantified. They are necessary to accurately model energy dissipation within the system, numerical solutions are used as the geometry is often complex and there are more degrees of freedom to solve for than in isentropic acoustics. The method presented in this thesis uses the complete formulation from COMSOL's FEM implementation for acoustics in thermoviscous fluids [78]. However, this method is computationally expensive to solve for. As detailed in 2.3 it contains five degrees of freedom in 3 dimensional models u_x, u_y, u_z, T and p. In such models, the discretization of complex fields are quadratic with the exception of p that is linear. As this formulation is complex to solve for, there is a

strong interest in developing viable reduced order models which includes these losses to accurately predict the acoustic behaviour of metamaterials.

2.3 Governing equations

The study of acoustic propagation in tubes dates back to the late nineteenth century. Helmholtz [79] analysed the induced viscosity effects and estimated absorption arising from them. Kundt experimentally tested this theory and found a higher absorption which he presumed to be from thermal effects [80]. The theory for viscothermal acoustics derived from fluid dynamics was first described by Kirchhoff in 1868 [81]. An exact solution to the equations of motion is not possible in general as the problem is non-linear. In general, acoustics is a first order approximation where non-linear effects are neglected [82]. Thus linear acoustics is characterised by small pressure perturbations. Acoustic studies primarily examine stationary sound fields, therefore time harmonic form can be used and equations carried out in the frequency domain. This is also more efficient as the sound field is resolved per frequency instead of a large time series. The Navier Stokes equation govern fluid motion under the continuum assumption, which signifies that it can be defined that a fluid particle is large compared to molecular scales but small in comparison with other length scales [82]. In summary the motion of a viscous compressible Newtonian fluid can be described by the conservation of mass, momentum and the energy equation, respectively.

$$\frac{d\rho}{dt} + \nabla \cdot (\rho \mathbf{u}) = 0 \tag{2.1}$$

$$\rho \frac{d\mathbf{u}}{dt} + \rho(\mathbf{u} \cdot \nabla)\mathbf{u} = \nabla \cdot \sigma + \mathbf{F} \tag{2.2}$$

$$\rho C_p T \frac{dT}{dt} - \alpha_0 T \frac{dp}{dt} = -\nabla \cdot \mathbf{q} + \phi + Q \tag{2.3}$$

where p, $\mathbf{u}$, T and ρ denote the dependent variables, pressure, velocity field, temperature and density. And $\mathbf{F}$ and Q are force and heat source and ϕ is the viscous dissipation function.. For a compressible Newtonian fluid, the Cauchy stress tensor σ, can be expressed as a function of the velocity field. Stokes made the following observations for Newtonian fluids [83, 84].

- The stress tensor is a linear function of the strain rate tensor.
- The fluid is isotropic.
- τ should vanish if the flow there is no deformation of the fluid elements [85].

The Cauchy stress tensor is given by

$$\sigma = -p\mathbf{I} + \tau = -p\mathbf{I} + \mu(\nabla\mathbf{u} + \nabla\mathbf{u}^T) - (\frac{2\mu}{3} - \mu_b)(\nabla \cdot \mathbf{u})\mathbf{I} \tag{2.4}$$

where $\mathbf{I}$ is the 3 x 3 identity matrix and τ the viscous stress tensor and μ and μ_b the dynamic and bulk viscosity of the fluid. Following Stokes's hypothesis, the dynamic viscosity for a Newtonian fluid μ_b is neglected and set to zero due to its small contribution to the total dissipation. A comprehensive discussion of Stoke's hypothesis related to the bulk viscosity is provided in [86]. Assuming the fluid is Newtonian and the heat flux $\mathbf{q}$, is proportional to the temperature gradient, this leads to Fourier's law;

$$\mathbf{q} = -\kappa\nabla T \tag{2.5}$$

where κ is the thermal conductivity, which is constant under linear acoustic assumptions. We can relate any of the thermodynamic state properties as a function of two other state properties.

$$\rho = \rho(p, T) \tag{2.6}$$

The viscous dissipation function is defined as $\phi = \tau(\mathbf{u}) : \nabla\mathbf{u}$. If the mean velocity is zero, this term vanishes under linear acoustic assumptions [87]. The viscous losses are not contributing to added heat flow at the boundary or increase internal energy in the system. The viscosity component in that case is only included through the Cauchy stress tensor in Equation 2.2. The viscous effects damp out propagating waves but are not included in the energy balance [88]. The heat capacity at constant pressure C_p and the coefficient of thermal expansion α_0 are both functions of pressure and temperature.

2.3.1 The Linearised Navier Stokes equations

It is possible to obtain a linearised version of the governing equations 2.1 to 2.3 around a steady state solution. Assuming for small perturbations where $p' << P_0$, a solution can be written as the sum of time-independent mean flow and a time-dependent perturbation. These can also be re-written assuming small time harmonic oscillations.

$$\begin{aligned} p &= p_0(x) + p'(t,x) = p_0(x) + Re\{p'(x)e^{\jmath\omega t}\} \\ \mathbf{u} &= \mathbf{u_0}(x) + \mathbf{u}'(t,x) = \mathbf{u}_0(x) + Re\{\mathbf{u}'(x)e^{\jmath\omega t}\} \\ T &= T_0 + T'(t,x) = T_0(x) + Re\{T'(x)e^{\jmath\omega t}\} \\ \rho &= \rho_0(x) + \rho'(t,x) = \rho_0(x) + Re\{\rho'(x)e^{\jmath\omega t}\} \end{aligned} \tag{2.7}$$

Inserting these perturbations for dependent variables with zero mean flow $\mathbf{u}_0 \approx 0$ to the governing equations, and keeping only first order terms the linearised Navier Stokes are obtained. In the ideal gas case, the following relationships can be derived from the state equation $p = \rho RT$, where R is the universal gas constant and β_T the isothermal compressibility.

$$\beta_T = \frac{1}{p_0} \qquad \alpha_0 = \frac{1}{T_0} \tag{2.8}$$

$$\rho = \rho_0 \left(\frac{p}{p_0} - \frac{T}{T_0} \right) = \rho_0 \left(\beta_T p - \alpha_0 T \right) \tag{2.9}$$

The time harmonic form $+e^{\jmath\omega t}$ represented by the convention $\jmath\omega$ of the continuity, momentum and energy equation are presented for viscothermal acoustics in the case of an ideal gas free from any external forces or heat source in Equations 2.10 to 2.12.

$$\jmath\omega\rho + \rho_0(\nabla \cdot \mathbf{u}) = \jmath\omega \left(\frac{p}{p_0} - \frac{T}{T_0} \right) + \nabla \cdot \mathbf{u} = 0 \tag{2.10}$$

$$\jmath\omega\rho_0\mathbf{u} = \nabla \cdot \left[-p\mathbf{I} + \mu(\nabla\mathbf{u} + \nabla\mathbf{u}^T) - (\frac{2\mu}{3} - \mu_b)(\nabla \cdot \mathbf{u})\mathbf{I} \right] + \mathbf{F} \tag{2.11}$$

$$\jmath\omega(\rho_0 C_p T - T_0\alpha_0 p) = -\nabla.\left(-\kappa\nabla T\right) + Q \tag{2.12}$$

It is necessary to use a viscothermal acoustic formulation in small acoustic devices where viscous and heat dissipative effects are large. In this thesis, a finite element implementation of the viscothermal acoustic formulation was used using COMSOL [78]. It is preferred to other methods, as the integral form can deal with discontinuities and overall more complex geometries. With this type of formulation it is important to properly resolve the acoustic boundary layers where viscous dissipation and heat

conduction are important. The dual requirement of boundary layer resolution and multi-degree of freedom resolutions render the method computationally expensive.

2.3.2 Helmholtz equation

If the system is lossless where $\mu = \kappa = 0$, the thermodynamic process in the system is assumed adiabatic and the acoustic field inviscid, the thermal conductivity and the temperature can be eliminated. Then the following constitutive equations for an isentropic gas which relates density and pressure to temperature can be used [89].

$$\rho = \frac{p}{c_0^2} \qquad T = \frac{p}{\rho_0 C_p} \tag{2.13}$$

The speed of sound where $\gamma = \frac{C_p}{C_v}$ is given by;

$$c^2 = \gamma \frac{p_0}{\rho_0} \tag{2.14}$$

Visco-thermal effects are neglected which leaves momentum and compressional effects to be included. The speed of sound in this scenario is satisfied by $c^2 = \frac{p}{\rho_0}$. Therefore assuming no external sources, Equations 2.10 to 2.12 can be reduced to the continuity and Navier-Stokes for lossless acoustics.

$$\jmath\omega p + c^2 \rho_0 \nabla \cdot \mathbf{u} = 0 \tag{2.15}$$

$$\jmath\omega \rho_0 \mathbf{u} = -\nabla p \tag{2.16}$$

Substituting the divergence of the momentum into the continuity equation yields to;

$$\nabla^2 p + k_0^2 p = 0 \tag{2.17}$$

where the isentropic wavenumber is $k_0 = {}^{\omega}/_{c}$ [90]. In most practical situations an exact analytical solution to Equation 2.17 does not exist. Solving the equation requires a numerical solution.

2.3.3 Finite element methodology

The partial differential equations are solved using a numerical method to obtain an approximate solution. The set of Equations 2.10 to 2.12 which describe the motion of a fluid particle under the continuum assumption can be adapted for a finite element

formulation. This method deals with discontinuities effectively and is adaptable to a multiphysics approach. The numerical studies carried out in this thesis use Comsol's FEM platform [78]. The finite element method provided by COMSOL uses a mixed formulation. The weak form of the viscothermal acoustic equations is obtained by using a Galerkin approach where Equations 2.10 to 2.12 are multiplied by corresponding test functions. These are integrated over the model's domain and Green's formula is applied to eliminate second order derivatives. The implementation of the governing equations in a mixed weak formulation used in COMSOL's FEM has been described by Kampinga [89, 91] and Nijhof [88]. The system matrix is presented by Rice [92] in matrix form where the global node **a** stores the five degrees of freedom **u**, p and T.

$$[\mathbf{K} + \jmath\omega\mathbf{M}]\,\mathbf{a} = \mathbf{F} \tag{2.18}$$

The loading vector **F** models boundary pressure, material injection and heat flux. K and M are constructed following the mixed formulations in [93]. In the case of isentropic acoustics, wave propagation is described by the Helmholtz equation and solutions for these acoustic wave problems can also be solved numerically. As with the governing equations which describe viscothermal acoustics, the same approach is used to apply FEM formulation to the Helmholtz equation. A test function ϕ_t is applied to the Helmholtz equation and integrated over the domain Ω of boundary Γ which leads to the following expression.

$$\int_\Omega \phi_t[\Delta p + k^2 p]d\Omega = 0 \tag{2.19}$$

Applying Green's first identity to the Laplace operator converts it to a domain and boundary integral which yields to the weak form of Equation 2.17.

$$-\int_\Omega \nabla\phi_t \cdot \nabla p d\Omega + \int_\Gamma \phi_t(\nabla p \cdot \mathbf{n})d\Gamma + \int_\Omega k^2\phi_t p d\Omega = 0 \tag{2.20}$$

The pressure can be approximated by the following relationship $p \approx \mathbf{Np}$ where **N** is the shape function of the matrix. In a Galerkin approach the test and shape functions are equivalent [94]. The FEM description to evaluate acoustic wave propagation is presented, composed respectively from left to right, of the acoustic stiffness, natural boundary conditions and mass matrices.

$$-\int_{\Omega} \nabla \mathbf{N}^{\mathbf{T}} \cdot \nabla \mathbf{N} d\Omega \mathbf{p} + \int_{\Gamma} (\nabla \mathbf{N} \mathbf{p} \cdot \mathbf{n}) d\Gamma + \int_{\Omega} k^2 \mathbf{N}^{\mathbf{T}} \mathbf{N} d\Omega \mathbf{p} = 0 \tag{2.21}$$

2.3.4 Discretisation

In order to obtain a numerical solution to the acoustic problem it is necessary to resolve the wavelength which depends on the frequency and sonic speed of the fluid. To resolve the wave, the elements of the mesh need to be smaller than the wavelength. The minimum number of degrees of freedom necessary per wavelength depends on the order of the elements used. Mesh elements are comprised of nodes. For a linear mesh element, the nodes are located at the vertices. A minimum number of degrees of freedom (DOF) per wavelength is required to compute the propagating wave. COMSOL considers 12 DOF per wavelength as an acceptable lower limit [78] for quadratic elements. As this value is cubed for 3D models by the volume of the structure it can lead to very large acoustic models and become computationally expensive. Attention needs to be taken for narrow regions, geometric details and gradients.

The weak form of the governing equations are discretised using FEM shape functions to interpolate the DOF. The element order and type used for the models discussed in this thesis are quadratic Lagrange shape functions for the velocity field and temperature. In air, the thermal and viscous boundary layers are of the same order of magnitude and the same element order is taken. To ensure numerical stability, the discretisation for pressure is set to an element order less than for the velocity field [95]. There is no evidence that the independent discretisation of the temperature is important for the stability, but it is convenient to have the same order as the velocity [91]. To resolve the wavelength the maximum element size allowed is set to $\lambda/6$, as there needs to be at least 6 elements per wavelength for quadratic Lagrange and 12 elements per wavelength for linear Lagrange.

2.3.5 Viscothermal boundary-layer effects

The viscothermal effects in small devices are important to correctly capture the acoustic behaviour. The viscous effect is the result of the viscosity in the fluid resisting the velocity gradient. Near a wall boundary a no slip wall condition is applicable, the velocity field $\mathbf{u} = 0$ is assumed to be null. In this region there are high viscous

forces and a large velocity gradient as the velocity field grows within the boundary layer to be fully developed at the bulk of the fluid [96]. Heat conduction in the fluid contributes to the thermal boundary layer development. The heat conductivity of air is proportional to the temperature gradient. An isothermal condition is assumed at the boundary with high thermal conductivity. This results in a temperature gradient which grows to the bulk region with a corresponding loss [97]. Both these effects contribute to damping the acoustic wave and a fine mesh is required in the acoustic boundary layer to sufficiently capture these losses. However, the pressure and normal velocity fields remain smooth within the boundary layer. Kirchhoff [81] and Rayleigh [98] investigated sound propagation through infinitely long narrow tubes. It was determined that boundary layer effects on the tube's walls emerging from the air's thermal and viscous properties should be included in the solution. As sound propagates through a fluid cavity bounded by rigid walls, a no-slip boundary condition applies at the wall, where the tangential velocity particle at the wall is zero. The viscous boundary layer which exists has a characteristic thickness δ_{visc}.

$$\delta_{visc} = \sqrt{\frac{2\mu}{\omega\rho_0}} \tag{2.22}$$

The thermal boundary layer is the resultant of heat exchanges between the fluid and the walls which has for characteristic thickness δ_{therm}.

$$\delta_{therm} = \sqrt{\frac{2\kappa}{\omega\rho_0 C_P}} \tag{2.23}$$

In air, the Prandtl number is the ratio of these lengths $P_r = \delta_{visc}^2/\delta_{therm}^2$ and is ~ 0.7 [99]. Gradients in this region are large so are the losses. Careful meshing consideration should be applied to correctly model the behaviour of the system. Parameters based on the acoustic boundary layer thickness are used to create and control the mesh to ensure the losses are included. When computing for a large frequency range an appropriate meshing strategy for the boundary layer should be devised as the thickness gets significantly smaller with increasing frequency.

2.3.6 Approximation for energy dissipation

As the computation time for viscothermal acoustics is significantly longer and a high mesh refinement is needed to resolve the acoustic boundary layers. Lossy Helmholtz

models have been developed which expedites the computation time, these models simulate the viscothermal losses that exists in narrow sections. There are geometrical limitations to these models. Kirchhoff [81] produced analytical approximations for sound propagation in wide tubes. Zwikker and Kosten [100] derived a solution which nearly covers all approximations and only depends on the shear wave number [101]. The Low Reduced Frequency (LRF) model provides a solution for propagation of acoustic waves including thermal and viscous losses in small waveguides, many geometry dependent analytical solutions are provided including slits and ducts. The thermal and viscous losses in the boundary layers are thus distributed over the fluid domain. One such approximation is the wide duct approximation which is presented in Equation 2.39, this model is applicable if the hydraulic diameter is much larger than the boundary layer thickness. The losses arising from the acoustic boundary layer are included through an effective wall shear force [87]. The approximations for a wide range of geometries can be used within COMSOL based on the low reduced frequency model as long as the cross section of the duct is much smaller than the acoustic wavelength [78]. This approach includes the losses through a complex wave number which is reintroduced into the Helmholtz equation.

$$\Delta p + k_{eq}^2 p = 0 \tag{2.24}$$

Where the value of the LRF complex lossy wave number k_{eq} depends on the type of approximation used for the duct in the model. The LRF model is computationally efficient as pressure is the only field variable, the mesh only needs to capture the acoustic behaviour [96] and does not require as much refinement. Some equivalent fluid models can also be used to capture losses in porous materials. These are based on the frequency dependent fluid density $\rho(\omega)$ and bulk modulus $K(\omega)$ of the porous material which are assumed to be related to the static flow resistivity. The values of $\rho(\omega)$ and $K(\omega)$ are complex frequency and pore dependent. Analytic expressions exist for simple pore shapes. The propagation of sound waves which includes viscothermal losses can be obtained by the following relationship which is comparable to the Helmholtz equation.

$$\Delta p + \omega^2 \frac{\rho(\omega)}{K(\omega)} p = 0 \tag{2.25}$$

Many propagation models have been developed since Kirchhoff, some are empirical with measurement data based on experiments of fibrous materials but their usage is quite restrictive [102, 103]. Analytical models are usually used for simple predefined geometries where cross-sections do not vary. It will be presented at a later stage that the results obtained through these models are a good design tool, even for small varying cross-sections, as it lowers the computation time required. More complex equivalent fluid models can be used for varying cross-sections such as the Johnson-Champoux-Allard-Lafarge model [104], an example of which is given in Appendix B.3 for a configuration developed in Chapter 4.

2.3.7 Incorporation of surface roughness in modelling

Some 3D printed structures will exhibit significant anisotropy depending on the type of additive manufacturing selected. The use of 3D printing technologies enables the manufacture of some complex periodic cellular structures which could not have been achieved with traditional methods. However, there is a gap in predicting the change in absorptive properties of these structures depending on what print technology and material is used as most modelling is carried out on an ideal representative unit. Predicting the roughness of these structures and incorporating into modelling is possible by handling certain parameters such as viscosity and flow resistivity. Flow resistivity σ is defined as the pressure difference Δp across a sheet over the volume velocity per unit area u' and sheet thickness t [105].

$$\sigma = \Delta p/u't = (\delta p/\delta x)/u' \tag{2.26}$$

The pressure gradient along a uniform tube of radius r carrying Steady Poiseuille's flow is

$$u = \frac{\Delta p r^2}{8\mu l} \tag{2.27}$$

This reduces to

$$\sigma = \frac{8\mu}{r^2} \tag{2.28}$$

Where $r = \frac{2V}{A}$.

The defects in printed components are difficult to account for. These defects are not homogeneous across the structure, as such they cannot be directly quantified. To

estimate the influence of the printing process, it is necessary to compare the acoustic behaviour between estimated numerical ideal behaviour and experimental characterisation of structures obtained via different printing technologies. A fitting procedure can be applied to results obtained by controlling the hydraulic radius and reducing its nominal value. This will increase the viscosity in the system which is usually true for 3D printed samples.

2.4 Acoustic metamaterial modelling

Additive manufacturing presents a unique opportunity to manufacture complex acoustic metamaterials. The benchmark design proposed by members of the COST Action DENORMS (CA 15125) was studied. The repeatability of the unit structure led to the development of versatile macro structures and the design variations aimed to provide an enhanced absorptive performance at lower frequencies. These simulations used the FEM formulation of the governing equations detailed in Section 2.3. By applying the appropriate boundary conditions, material properties and using proper discretisation full numerical solutions could be obtained with high performance computing. The equations governing the system were applied to individual mesh elements that combined to give a global numerical result. The simulations carried out primarily used the thermoviscous module from COMSOL to model the energy dissipation within the cellular structure. Throughout this study, experimental results were compared with numerical simulations and there was a particular focus in this section to examine the deviation observed due to the technology employed for manufacture. Also, close correlation between numerical simulations and experiments ensured that the essential physics were properly resolved. Furthermore, once the model was validated it was used to predict the acoustic behaviour of built-up structures that could not be manufactured with the available printers in the laboratory due to the limitations on build volume. The technologies reported in [53] were presented in Section 1.6 and experimental testing of those samples under normal incidence were compared with numerical results based on an idealised unit cell. The following section reports on the modelling strategy employed for an acoustic metamaterial, results of their absorptive performance are also available in [53]. Noting the precision afforded by the full viscothermal formulation there was an

emphasis to use reduced order models to achieve similar results in a more time efficient way.

2.4.1 DENORMS structure

The DENORMS periodic cell contained a spherical cavity that was connected to identical cavities of neighbouring cells by cylindrical tubes. The parameters which described the structure were the cell size, the internal spherical cavity and the interconnecting cylinders. The relative simplicity of the design made it easily modifiable to suit the technology used for manufacture. The dimensions were selected to suit the allowed resolution of the printing technologies used in this study. The modelled DENORMS unit was composed of a 5 mm cubed cell size with an interior spherical pore of radius 2.1 mm connected by short cylindrical channels of radius 1 mm from all faces of the cubic cell as in Figure 2.2.

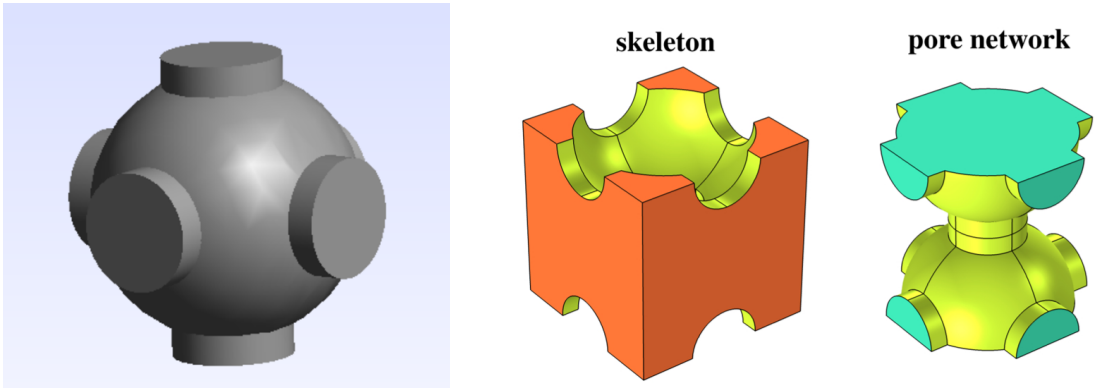

(a) DENORMS unit cell.

(b) Skeleton and the corresponding pore network for DENORMS unit cell [74].

Figure 2.2: DENORMS benchmark design

The unit cell in Figure 2.2 was used to construct a 10 layer deep periodic structure. As outlined in Chapter 1, some acoustic metamaterials exhibited interesting reflecting and absorptive behaviour achieved by sub-wavelength thicknesses. The objective of these design variations was to lower the first resonant frequency. This was experimented by increasing the length of the channel where energy could dissipate within the same depth. And different lengths of resonating chambers were combined with the aim of achieving a broadband behaviour. Design modifications studied include the use of space-coiling as demonstrated for the DENORMS design in Figure 2.3 and labyrinthine type construction in Figure 2.4 to achieve a preferred acoustic behaviour. A design

variation of mixed length channels of 4, 6, 8 an 10 resonators inside a depth of 7 cells is presented in Figure 2.3. Mixing different lengths added a parallel type behaviour by overlapping different lengths which led to a broader absorption spectrum. The

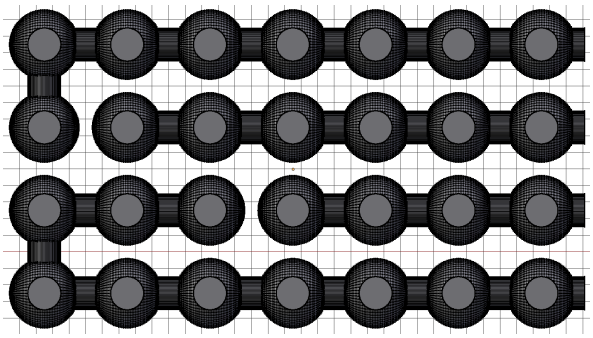

Figure 2.3: DENORMS space coiling of mixed length [53].

labyrinthine variation made good use of available space by effectively doubling the length of resonators in order to reduce the first resonant peak. The tortuous path created resulted in a longer channel by closing off every second cell as in Figure 2.4. This variation essentially doubled the number of resonating chambers within the same length in Figure 2.4 from a depth of 2 to 4.

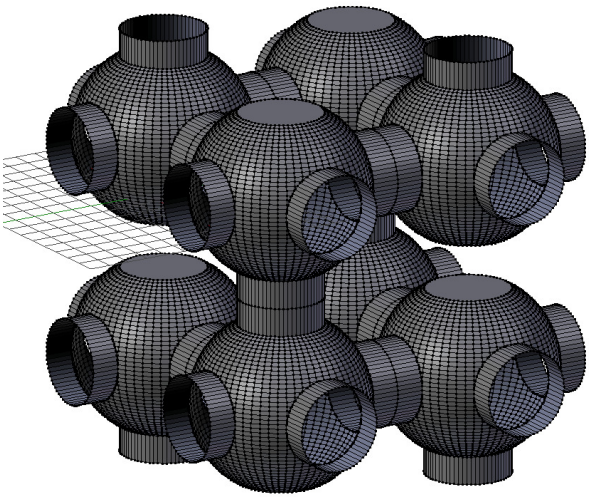

Figure 2.4: DENORMS labyrinthine structure [53].

2.4.2 Model configuration

The unit cell shown in 2.2 was constructed in COMSOL Multiphysics. As part of the study in [53], a three dimensional model of up to 10 layers deep of the basic cell was developed including some design variations shown previously. Two separate domains

were specified in all models, one which is governed by the Helmholtz equation in blue in Figure 2.5 where the loading was included and the other by a full viscothermal formulation in red to capture the losses in the resonating chambers as is shown in Figure 2.5. The thermoviscous component is capable of modelling the dissipation from viscous shear and thermal conduction. However, as full viscothermal formulation came at a high computational cost, reduced order models are often required to model complex systems [101, 106]. This study published in [53] was, notwithstanding, restricted to full viscothermal modelling in order to remove potential error due to modelling simplification. In order to represent the physical system we wished to test, a model of the

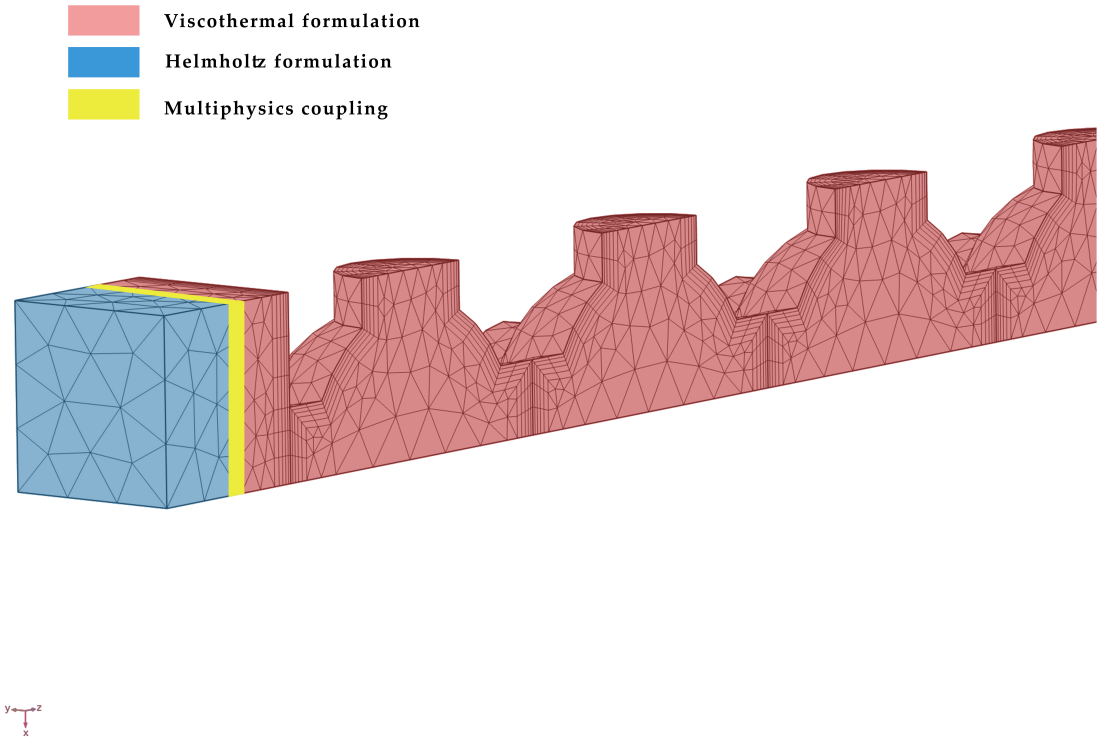

Figure 2.5: Model set up of the 10 layer deep DENORMS cell

physical environment was created for the finite element method within COMSOL. The geometry and material properties were assigned and boundary conditions were imposed to model the system. To reduce the computational effort required it was important to simplify the model as much as possible. This was achieved by using different symmetry boundaries or having a one or two dimensional models.

Visco-thermal modelling

To eliminate unphysical effects at the entry, a waveguide was modelled to precede the resonating chambers. A multiphysics approach within COMSOL was well suited for the type of problem under investigation, as a radiating boundary could be imposed at the inlet surface of the waveguides which ensured that backward reflected waves were effectively absorbed. The finite element formulation of the governing equations 2.10 to 2.12 were implemented within the cells and the fluid parameters used are defined in Table 2.1. The bulk viscosity, μ_b, was neglected and set to zero [104]. A lot of diverging

Symbol	Value	Unit
T_0	293.15	K
p_0	101325	Pa
ρ_0	1.2043	kg/m^3
μ	1.8140e-05	$Pa.s$
μ_b	0.6μ	$Pa.s$
C_p	1005.4	$J/(kgK)$
κ	0.0258	$W/(mK)$

Table 2.1: Properties of air used in the study on the influence of additive manufacturing effects on the produced acoustic behaviour [53].

views exist on the value of the bulk viscosity should take, for monotatomic gases it is practically negligible. Rajagopal showed that for most realistic fluids μ_b cannot be zero [107]. However, good results were obtained for compressible fluids neglecting this value [86]. Therefore, both are seen as valid for modelling purposes and the divergence observed in absorptivity was assessed for one of the system under consideration as can be seen in Figure 2.14. The system was excited by a unit plane wave pressure excitation p_i at the inlet of the manifold which was a radiating boundary. The depth of the manifold was 3.5 mm, the inflow section in blue in Figure 2.5 was modelled using a lossless Helmholtz model that transitioned to a full viscothermal model within the pore structure in blue. At the fluid-solid interface a no-slip isothermal condition was applied, **u=0** and $T = 0$. Second order Lagrangian elements with quadratic shape function interpolation were used for the three velocity and temperature nodal variables and linear interpolation for the pressure variable [78]. Using the average velocity $\overline{u}$ at the inlet face, the system impedance could be estimated.

$$Z = p_i/\overline{u} \tag{2.29}$$

The impedance at the entry to the cells can also be estimated through the impedance translation theorem [108]. The absorptivity of the system which refers to the energy loss which occurs as a sound waves comes into contact with a material, can be obtained through the following relationship, where c is the sonic speed, $c = \sqrt{\frac{\gamma P_0}{\rho_0}}$ and the ratio of specific heats γ was set at 1.41.

$$\alpha = 1 - \left| \frac{Z - \rho_0 c}{Z + \rho_0 c} \right|^2 \tag{2.30}$$

As was mentioned in Section 2.3.5, attention was required when meshing close to the boundaries; as the frequency dependent boundary layer becomes thinner at higher frequencies. As the study was performed on a large frequency sweep, it was important to create a frequency dependant mesh. Parametrisation of element sizes and boundary layer thicknesses are possible and should be used. Different procedures were explored to address this, keeping in mind the computational expense involved. However, when performing this on a larger frequency range it demanded large computational resources as the mesh was reconstructed at each frequency step. A trial viscothermal simulation was performed on a 10 mm cylinder of 2 mm diameter to realise a parametric mesh and assess its feasibility. The frequency dependent viscous boundary layer's thickness evolved from thick to thin with increasing frequency. Figures 2.6 and 2.7 shows the velocity profile at 410 Hz at different values of the frequency step parameter defined as $f_0 = 10Hz$ used to control the mesh. It can be seen that for $f_0 = 10Hz$ the boundary layer is much thicker than for $f_0 = 410Hz$. A frequency dependent mesh for the range desired at different values of f_0 was achievable but its implementation within COMSOL was inefficient. To compute the plane wave radiating in this cylinder it took 38 hours and 12 minutes on a Xeon CPU 14 Cores, 2.6 GHz and 64 Gb RAM workstation. Using this mesh implementation was thus not feasible for more complex geometries. No adaptive sweeping methods were implemented for this trial study due to the necessity of reconstructing the mesh at each frequency step.

An alternative approach was chosen where multiple meshes were used with a specified viscous boundary layer thickness and a maximum element size based on a reduced frequency range. Multiple studies were performed and results were subsequently compiled together. The meshing settings in COMSOL have been explored for some designs, and have informed how best to operate simulations by mitigating between sensitivity

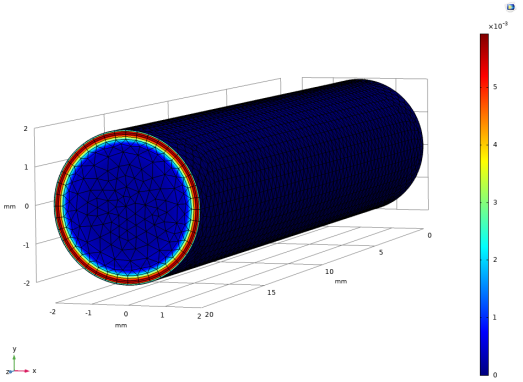

Figure 2.6: Velocity profile at 410 Hz for $f_0 = 410H_z$

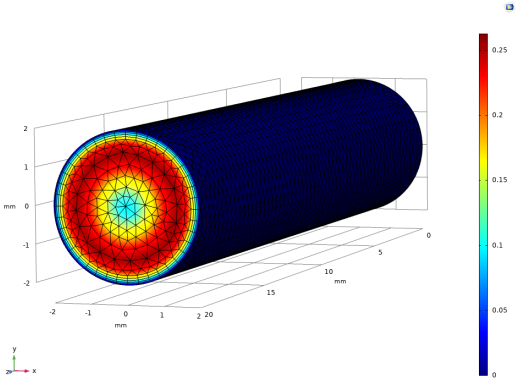

Figure 2.7: Velocity profile at 410 Hz for $f_0 = 10H_z$

and available computational resources. For acoustic meshing within COMSOL a minimum of six elements per wavelength should be specified for the maximum element size. The viscous boundary layer depth was used as a meshing control parameter at the boundaries. The constructed meshes were composed of tetrahedral elements and a boundary layer thickness was chosen for each reduced frequency range. The maximum element size was kept at six elements per wavelength and boundary layer thicknesses were changed for every 500 Hz increment. However, for viable run times it was not possible to keep this to a minimum for certain designs. In the case of the space coiling system the maximum element size parameter had to be increased due to computational resources available. As such, convergence studies must be performed with a parameter metric to assess the sensitivity to further refinement. Figure 2.8 shows result of convergence analysis performed for the baseline 10 layer deep DENORMS configuration. Within COMSOL some automatic meshing parameters may be used which detect critical areas to be refined. As the viscothermal 3D model was computationally quite expensive, a simple convergence analysis was first performed using automatic settings which prescribed levels of refinement by specifying sizing parameters based on the geometry and level of refinements in simple terms from normal to finer [78]. The ultimate automatic meshing setting used, level 4, included an automatic boundary layer adjustment factor. Once the highest level of predefined refinement setting after which a solution could not be solved due to lack of memory during LU factorisation was reached, user-defined refinements were prescribed. The description of the number of nodes used for the different refinement levels is provided in Table 2.2. The elements used in this

geometry were mainly composed of linear and quadrilateral tetrahedral elements. The mesh which was used in the study corresponds to level 5 where multiple meshes were divided on a reduced frequency range in order to ensure a frequency-dependent mesh while ensuring the computational expense involved. It was not possible to test for further refinement on the workstation used during this study due to out of core memory limitations. Even though it can be seen from Figure 2.8 that full convergence has not been reached in the sensitivity analysis. However, as it was not possible to solve for further refinements, refinement level 5 was selected.

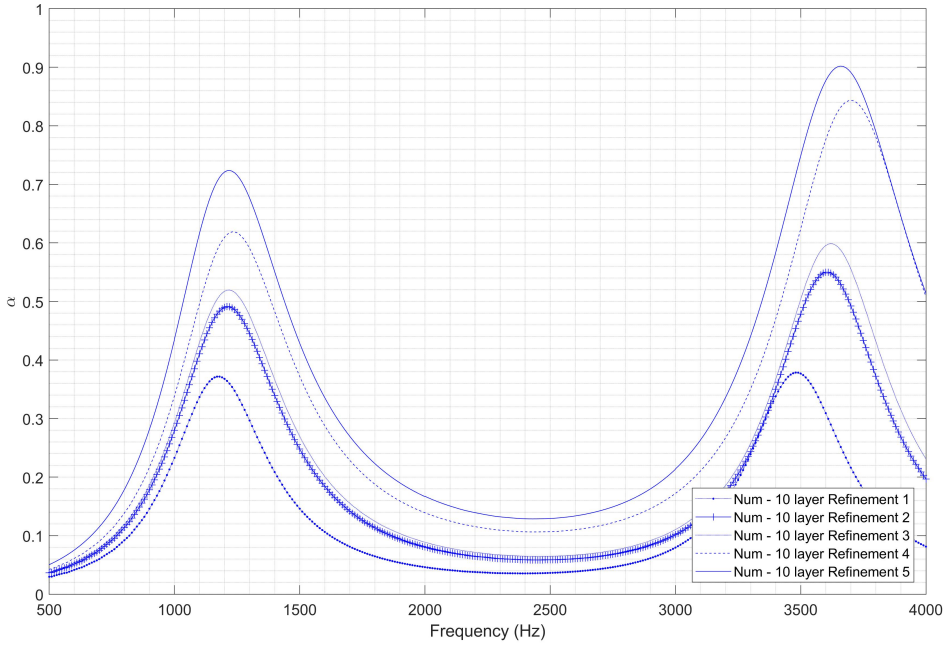

Figure 2.8: Mesh convergence analysis for 10 layer deep DENORMS cell configuration.

Refinement level	Number of nodes
level 1	2243
level 2	9680
level 3	17869
level 4	23216
level 5	52957

Table 2.2: Baseline 10 layer deep DENORMS cell - levels of mesh refinement.

For the largest space coiling system, this was set up using an automatic boundary layer setting available in COMSOL and absorptivity results were compared to user specified boundary layer thicknesses at every 500 Hz step. A number of convergence

studies showed the reported absorptivity to be relatively insensitive to further refinement. Where possible, the usage of symmetry was availed of to reduce the size of the model. The mesh structure for some sample temperature and velocity plots at 500 Hz are shown in Figure 2.9 and 2.10 [53]. It should be noted that when comparing numerical predictions with experimental data obtained from 3D printed materials the surface roughness may increase the acoustic boundary layer thicknesses [109] and thus have an effect on the absorptivity. That increase was not modelled in this study as no definitive roughness measurements were available. In addition Padé based frequency sweeps were availed of to deliver a resolution of 50 Hz for the mixed length space coiling and 10 Hz for the other models with run times of 24 hours using a modest workstation (Xeon CPU 14 Core, 2.6 GHz and 64 Gb RAM).

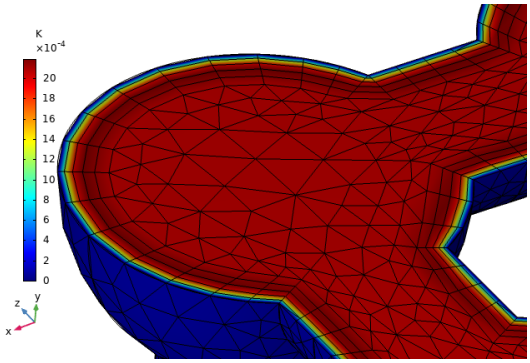

Figure 2.9: Temperature variation (K) unit cell at f=500 H_z [53].

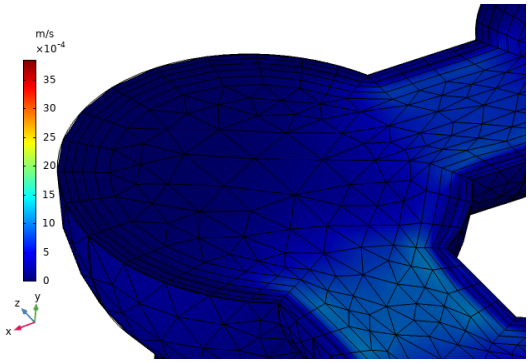

Figure 2.10: Axial component of velocity (m/s) unit cell, at f=500 H_z [53].

2.4.3 Experimental method

The numerical strategy used to predict the behaviour of the DENORMS designs was outlined previously. An acoustic validation of the designs and the printing technology employed for manufacture was performed through experimental measurements within the Aerialist project [53]. Normal incidence absorption properties were obtained using an impedance tube following the ISO 10534-2:2001 standard [110], which describes the test rig and procedures for estimating the complex acoustic impedance of a material under normal incidence using the two-microphone method. The impedance tube used has a 40 mm internal diameter, the lower frequency limit at 300 Hz is determined by the speaker, a BMS 4591. In practice the upper frequency limit is reduced to approximately 4200 Hz due to signal to noise limitations in the calibration and setup

and to ensure that we are still under the plane wave assumption. The microphone spacing is 26 mm and the distance of the closest microphone to the sample is 45mm. This speaker is driven by the output signal of a National Instruments DAQ which has been amplified by a power amplifier. The speaker bolts on to the end of the tube to provide a tight seal with little leakage of sound. GRAS 40 PL array microphones were chosen to instrument the rig as they have a frequency response (± 1 dB) in the region of 50 Hz - 5 kHz and upper limit of the dynamic range of 142 dB re 20 μPa allowing for testing up to high pressure amplitudes. The microphones are connected to the National Instruments DAQ and the signals are recorded in Matlab. The microphones are calibrated using the switching methods described in ISO 10534-2:2001. The square section on the right of figure 2.11 is composed of the sample holder where the different 40 mm diameter manufactured samples are placed. The impervious surface in the experimental rig is produced by a 20 mm thick piece of aluminium bolted on the end of the tube.

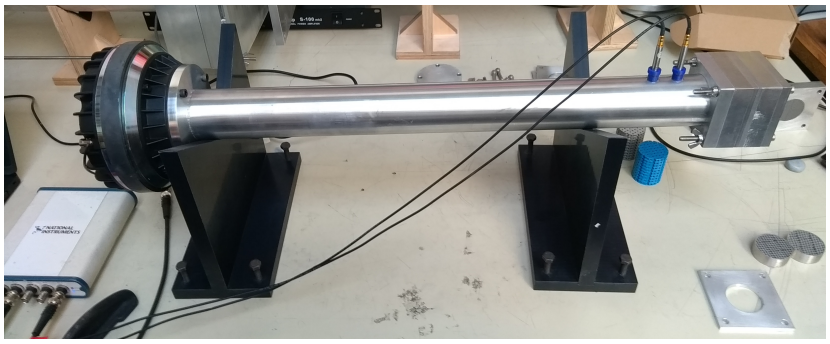

Figure 2.11: Impedance tube rig

The reflection coefficient is given by the ratio of the reflected wave amplitude (B) to the incident wave amplitude (A)...

$$R = B/A \tag{2.31}$$

The absorption coefficient α is calculated from the reflection using:

$$\alpha = 1 - |R^2| \tag{2.32}$$

In the experimental set-up, white noise is produced through the speaker and the acoustic pressures p_1 and p_2 are measured by microphones 1 and 2. The complex sound pressures at the two microphones are given by the sum of the forward and backward

travelling waves in the tube:

$$p_1 = Ae^{jkx_1} + Be^{-jkx_1} \tag{2.33}$$

$$p_2 = Ae^{jkx_2} + Be^{-jkx_2} \tag{2.34}$$

where x_1 and x_2 are the distances from the face of the sample to microphone 1 and 2 respectively. The complex pressures are used to find the transfer function H_{12}, from which the reflection factor can be identified.

$$H_{12} = p_1/p_2 = \frac{(Ae^{jkx_1} + Be^{-jkx_1})}{(Ae^{jkx_2} + Be^{-jkx_2})} \tag{2.35}$$

Using $R = \frac{B}{A}$ we get

$$H_{12} = \frac{(Ae^{jkx_2} + RAe^{-jkx_2})}{(Ae^{jkx_1} + RAe^{-jkx_1})} \tag{2.36}$$

Rearranging, we find

$$R = \frac{(H_{12}e^{jkx_1} - e^{-jkx_2})}{(e^{-jkx_2} - H_{12}e^{-jkx_1})} \tag{2.37}$$

The reflection factor can then be used to calculate the absorption coefficient and acoustic impedance. Energy can be lost in the system during experiments by factors such as porosity or internal friction in the material. This will affect the reflection and absorption coefficients evaluated. In this study [48], the resulting spectral resolution of the tests was 2Hz with 1000 averages used for the estimation of the frequency response functions. All measurements were repeated three times with complete dismounting of the sample between measurements to ensure repeatability of the test procedure.

2.4.4 Sound absorption for periodic DENORMS structures

The numerical predictions obtained for the different configurations of the DENORMS cell are reported in this section, some of which were published in [53]. An experimental validation is also presented, different additive manufacturing techniques were used to create the samples and their impact on the material's performance was examined. The basic 10 cells deep DENORMS configuration was used as a baseline to inform how best to model these structures. A full viscothermal numerical solution for this configuration producing a depth of 50 mm is reported in Figure 2.12, where it can be observed that the lattice of cells produced peaks in the absorption coefficient in the region of 1200 Hz

and 3500 Hz. In comparison with a quarter wavelength resonator which would require a length of 143 mm.

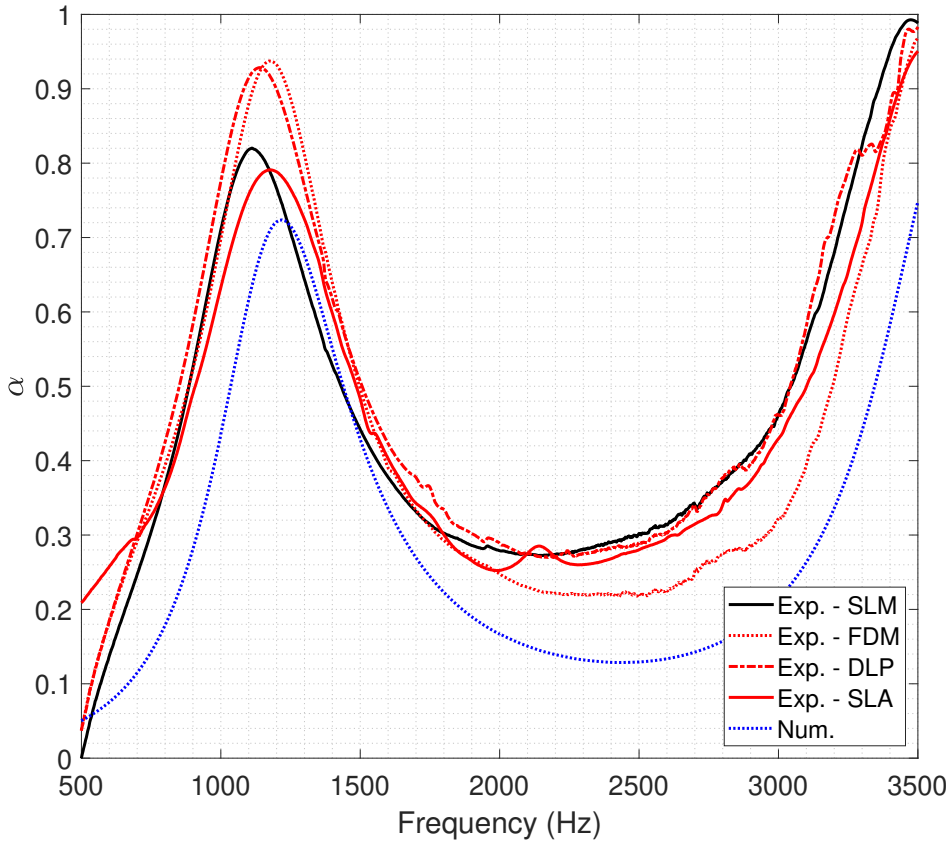

Figure 2.12: Absorption coefficient of the 10-layer-deep DENORMS cell using different printing technologies [53].

All four printing technologies used in this study whose functioning principles have been described in Section 1.6 are also shown in Figure 2.12 for the baseline design. A double absorptive peak can be seen in the regions of 1150 Hz and 3500 Hz. The 3D Systems SLM machine was considered the best standard of geometric accuracy and surface finish. The cobalt chrome sample is denoted by the black line. The other three printing technologies visible in red are polymer samples which were produced using more economical desktop printers. The numerical result plotted in blue underpredicted the absorption across the tested frequency range. The numerical models were based on an idealised unit cell, therefore no quantified metric arising from the impact of surface roughness which can be seen in the different samples in Figure 1.19 were included in the modelling. Within the polymer prints, SLA print technology would produce samples with higher design fidelity. The SLA sample produced by the Form 2 printer showed good accord with the SLM sample in both amplitude and frequency

peak occurrence. While the resonant frequencies were in the same region for the FDM and DLP prints, the resultant amplitude of their absorption peaks was of a higher amplitude. The FDM print was manufactured from an Ultimaker desktop printer, in this technology material spurs may remain in the channels as is visible in Figure 1.19. This created internal defects within the channels that may have contributed to the introduction of supplementary losses visible in the absorptivity plot. The staircase effect which was previously discussed in relation to DLP samples also contributed to additional losses within the system. The numerical model underpredicted these losses as it was assuming an idealised system, and surface roughness produced an enhanced viscous dissipation effect. An allowance for surface roughness could be made in an unpolished manner by simply adjusting the viscosity in the model. However, it was difficult to obtain a correct factor to adjust the viscosity by. The quality of the surface finish is also technology and print dependent. There is a lack of repeatability within additive manufacturing technologies which makes predicting the acoustic behaviour of printed samples difficult. When performing an experimental validation of printed acoustic metamaterials it would therefore seem more desirable to opt for a SLA printer which produces prints of superior quality in polymer samples and even though it is more expensive than the other two technologies, it is relatively low-cost. Due to the computational expense and solution time associated with performing viscothermal simulations alternatives are desired. From a design point it is preferred, and when dealing with predicting the acoustic behaviour of printed metamaterials there are many effects which lead to deviations in the results obtained. This compiled with surface roughness, interior defects as well as repeatability complexifies the prediction of the acoustic performance of samples. Hence, reduced-order models are preferable as a modelling tool for design. These models include losses through analytic expressions based on the geometry considered. These losses are included in a complex wave number in the Helmholtz equation, details which were previously described in Section 2.3.6. Absorptivity results presented in Figure 2.13 used a wide duct approximation which assumed a constant cross-section where the cells hydraulic diameter was prescribed, $H_d = 4A/P$. Even though, for the cells that were being modelled the cross-section was not constant, the prediction given was satisfactory so deviations observed were to be expected. This model had the advantage to produce results in a computationally

inexpensive manner as only one dependent variable was being solved for versus five for a viscothermal model. Another significant benefit of using this propagation model which is of important value in FEM is that detailed mesh refinement near boundaries is not necessary.

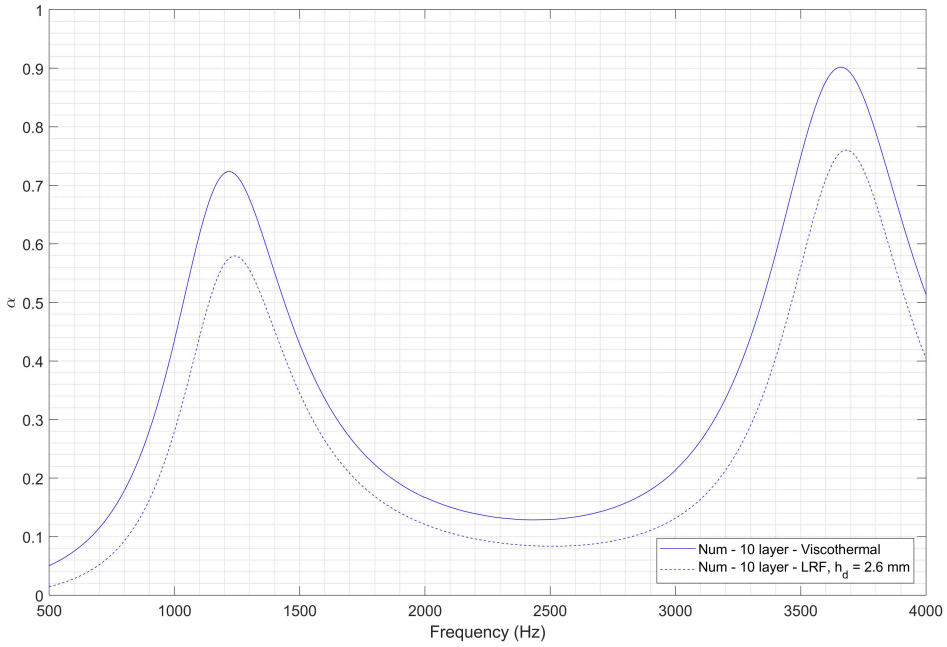

Figure 2.13: Absorption coefficient for 10-layer-deep DENORMS cell determined using LRF - wide duct approximation.

It was previously mentioned that there were a lot of diverging views on how to take into account bulk viscosity, it is firstly difficult to measure, default values within COMSOL's thermoviscous module propose $\mu_b = 0.6\mu$ for air [111]. The bulk viscosity characterises the fluid's resistance to volume change. As such the effect of adding bulk viscosity in the model should reflect additional losses within the model that control sound attenuation. Figure 2.14 shows the effect of the bulk viscosity on the absorption for the 10-layer deep DENORMS configuration, the experimental results from the SLA print sample was included for comparison. The inclusion of bulk viscosity did not seem to widen the "Gaussian" shape of the absorption coefficient obtained numerically. The amplitude of the resultant absorption was lower than when the bulk viscosity was set to zero. This would confirm Stokes's hypothesis and the rationale behind neglecting that term. Using Stokes hypothesis, the effect of dilatation on the viscous stress tensor was neglected in the model. However, the default value set by comsol does not have an unfailable base, it is taken from an estimated temperature dependent value exper-

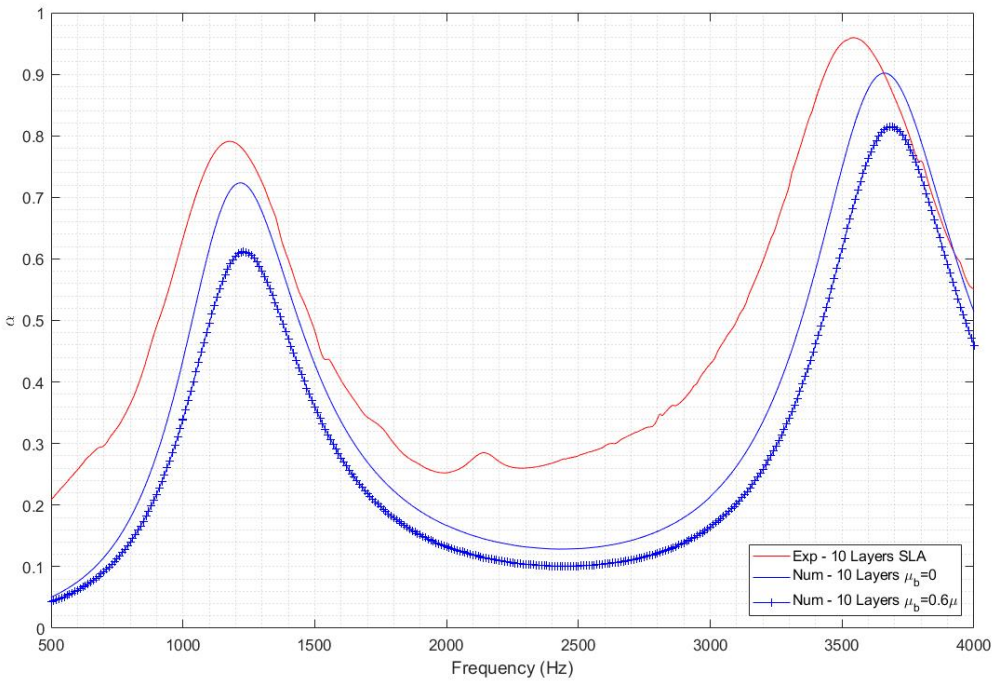

Figure 2.14: Effect of bulk viscosity on absorption coefficient for layers deep of the DENORMS cell. (Red - Experimental Results from sample printed on the SLA Form 2, Blue - Numerical Results)

imentally determined for air. As the inclusion of additional losses incurred through compression and dilatation of the fluid should lead to further energy dissipation. This baseline configuration motivated design alterations with an objective to operate at lower frequencies and increase the band of absorption. The design modifications were constructed while considering the limits imposed by additive manufacturing technologies available. This limited the coiling of the structure to single and double layer with the SLA printer. Analysing the response to different layer depths of the DENORMS cell configuration in Figure 2.15 led to the development of a combined mixed length design. Increasing the depth lowered the occurrence of the first peak of absorption and produced a double absorptive peak in the frequency region of interest. The modified lattice of DENORMS cells presented in Figures 2.4 and 2.3 are a result of this observation. The effect of the layer depth of cells on the first resonant frequency, f_{α_1} followed the power law relationship described in Equation 2.38 [112]. This effect is represented in Figure 2.16 and was analysed up to doubling the length of the baseline configuration which had for effect to half the frequency of f_{α_1}.

$$f_{\alpha_1} = 12015 \times D^{-0.995} \tag{2.38}$$

Where D is the number of cells deep. It can also be noted that f_{α_1} is proportionnal to $\frac{1}{D}$.

A validation of the absorptivity is provided in Figure 2.17 with experimental normal incidence results obtained from SLA prints of the corresponding structures of differing length depths. Experimental and numerical results provided a reasonable match even though some frequency offsets are present which are most likely due to geometric inaccuracies. And the amplitude difference observed could be due to the increased wall roughness in the printed components which enhanced the energy dissipation.

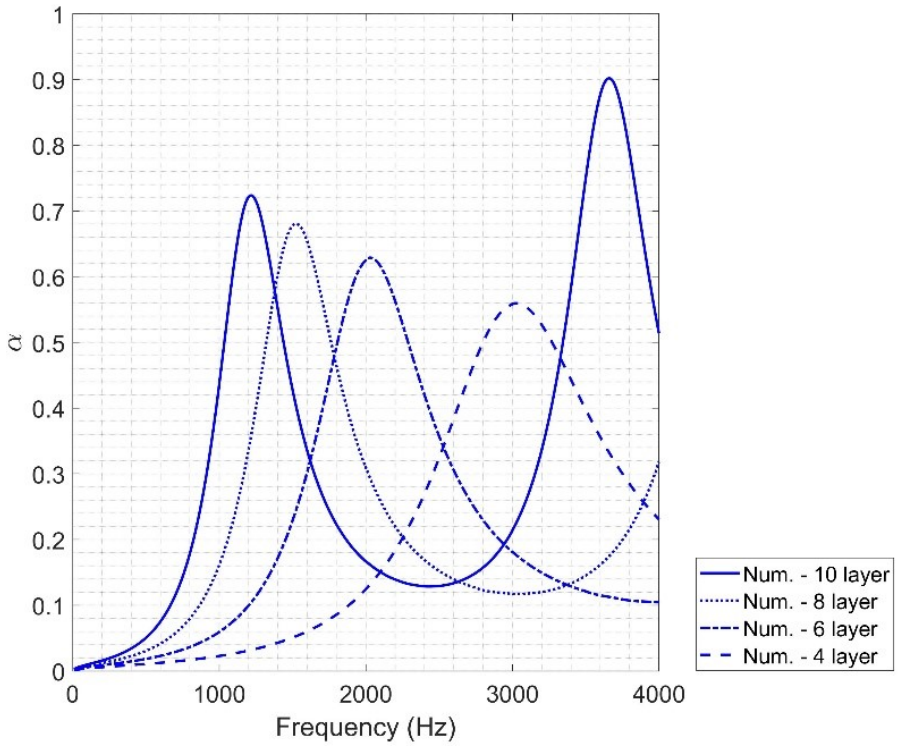

Figure 2.15: Absorption coefficient for 4, 6, 8 and 10 layers deep of the DENORMS cell.

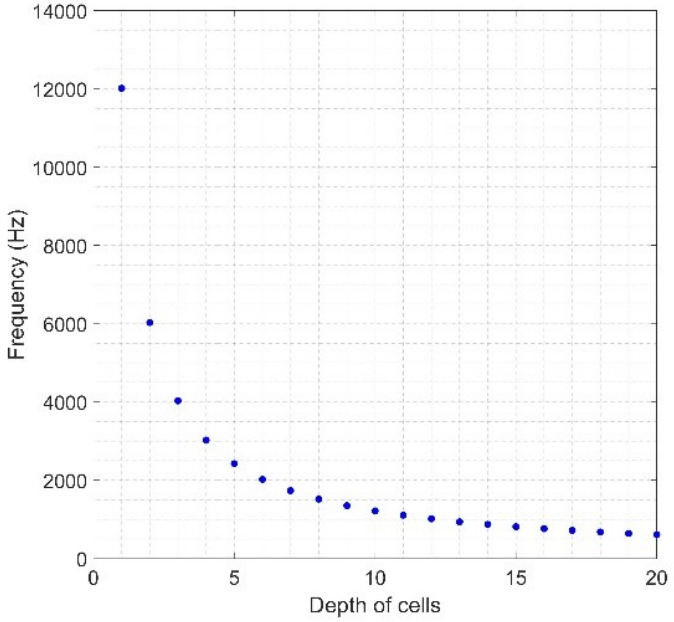

Figure 2.16: Depth of cells and its effect on resonant frequency.

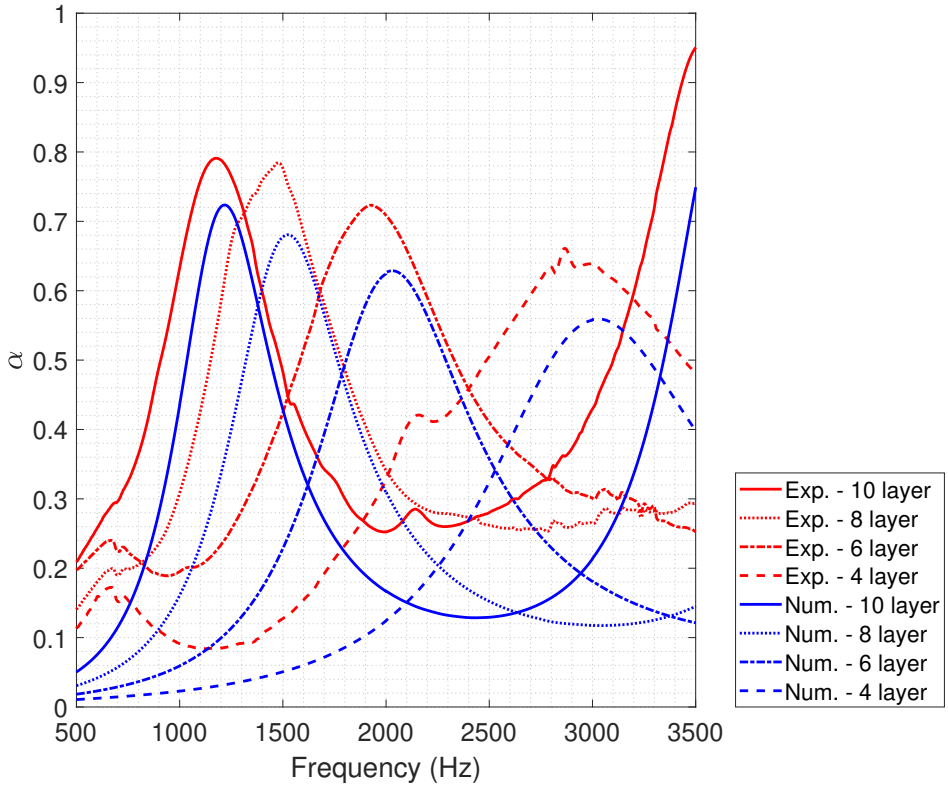

Figure 2.17: Absorption coefficient for 4, 6, 8 and 10 layers deep of the DENORMS cell printed on the SLA Form 2 (Red - Experimental Results, Blue - Numerical Results) [53].

The effect produced by the mixed length design inspired the combination of multiple length depths of the DENORMS cell. Numerical results obtained through viscothermal modelling as well as experimental measurements carried out on different print technologies (SLM, DLP and FDM) used in this study are reported in Figure 2.19. Due to the nature of the SLA process, successful samples could not be manufactured with the Form 2 due to resin retention within the channels. The high viscosity of the polymer resin creates blockages and cannot be removed through post-processing methods. The combined length design includes connecting channels by making use of all available space. Velocity plots for the combined mixed length design are provided in Figure 2.18. These demonstrate the corresponding acoustic velocity associated with each numerically determined absorbing resonant peak. The contribution made by each depth length result in multiple resonant absorption peaks at the following frequencies 1250 Hz, 1550 Hz, 2050 Hz and 3050 Hz can be observed. This shows the effect of the channel length on the frequency response. Alternatively, this could potentially be

modelled analytically as a series of spring-mass system or using a model for periodic porous media.

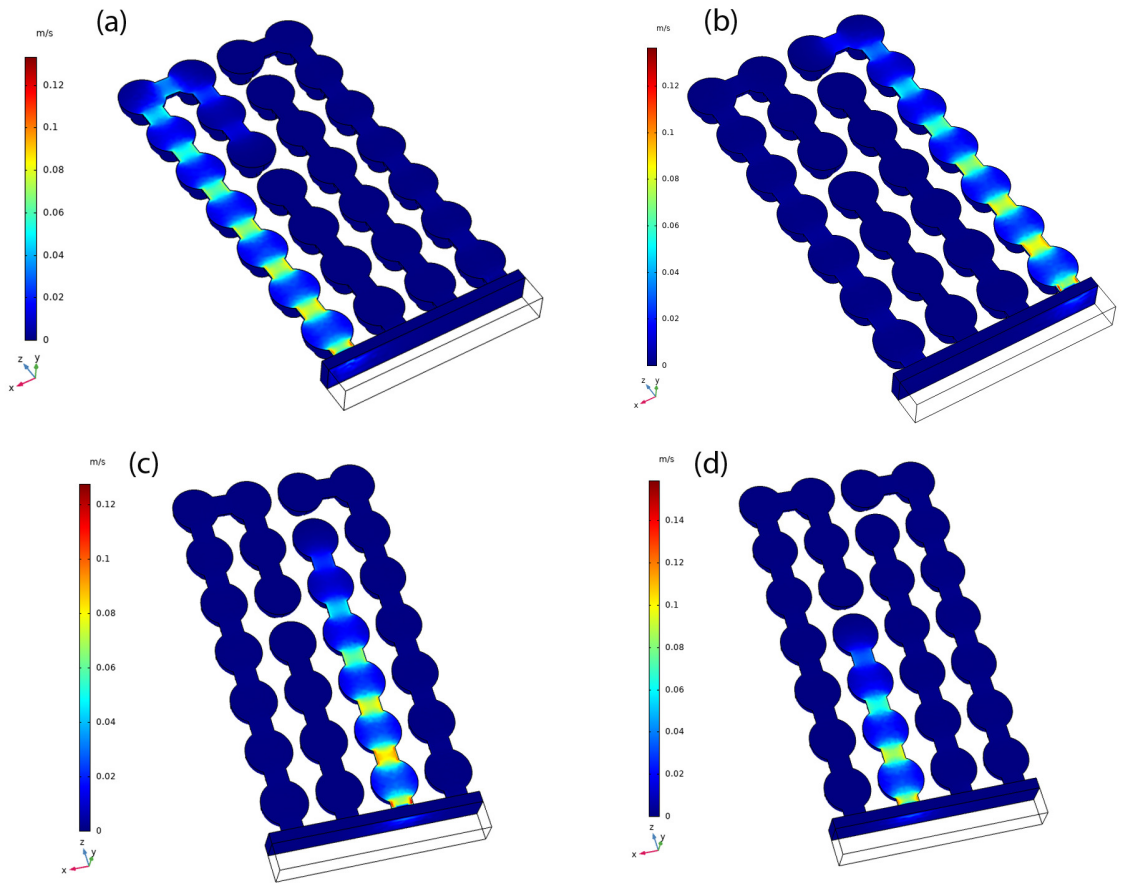

Figure 2.18: Axial component of velocity (m/s) within the lattice (a) f = 1250 H_z (b) f = 1550 H_z (c) f = 2050 H_z (d) f = 3050 H_z [53].

The numerically determined absorption results provided an estimation of the acoustic performance of this combined design. The absorption coefficient differed from all experimental results which can be explained by the geometry of the design and the manufacturing process used. The viscothermal simulations carried out for the space-coiling design were the most computationally demanding and it was mentioned previously that allowances had to be made for the computational grid (196131 nodes) which induced some errors. Furthermore the frequency step was increased from 10 Hz to 50 Hz so there are fewer points visible in the plot. However, the problem exposed with the possible entrapment of resin when using SLA technology can inform some other defects that occur with other technologies for the same design. The absorption measured on the FDM produced sample showed a more broadband behaviour and the

resonant peaks visible numerically were not shown as explicitly. The match between the DLP and SLM samples is much closer to the numerical predictions and the absorptive peaks are more clearly defined. Considering this design had a total depth of 7 cells which is equivalent to a thickness of 35 mm, its performance is good and shows a high broadband absorption spectrum in the frequency range of interest.

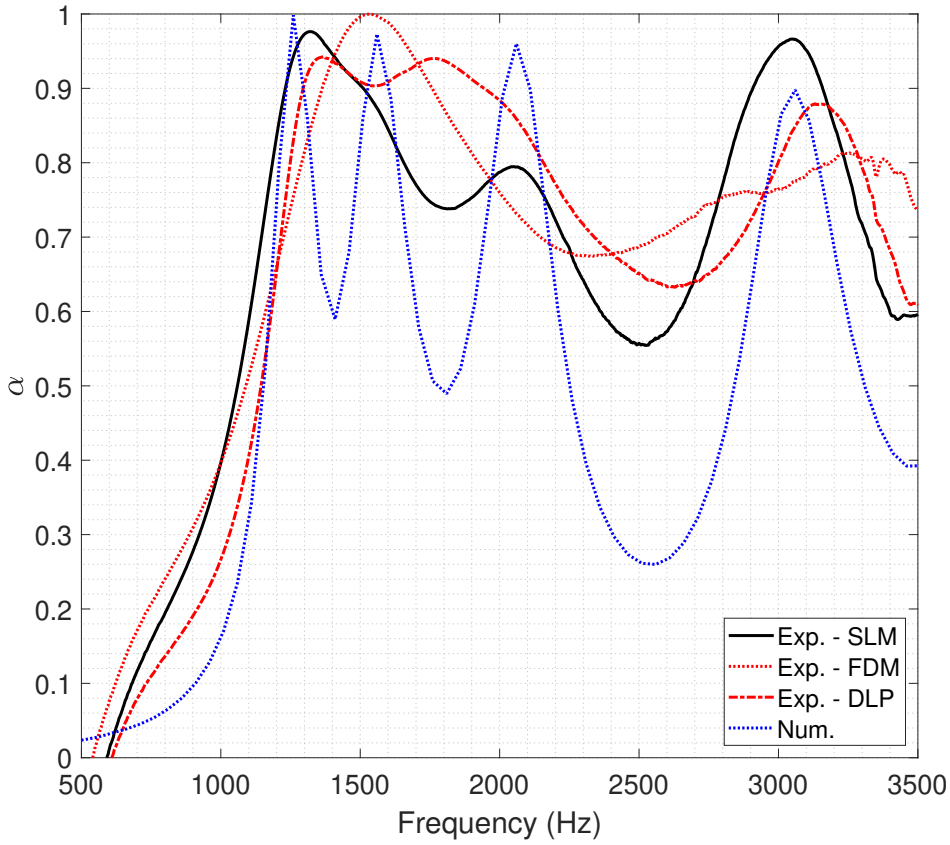

Figure 2.19: Absorption coefficient for combined 4, 6, 8 and 10 layer depths of the DENORMS cell [53].

The effect of surface roughness and defects from these prints on the acoustic performance of the combined layer depth sample could be incorporated in a pragmatic way by increasing the viscosity within the system. Due to the solution time taken for the combined mixed length structure composed of multiple frequency dependent grids, the effect of viscosity on the absorption within the system was analysed with a coarser mesh (83120 nodes). The results obtained are presented in Figure 2.20. The value for the dynamic viscosity given in Table 2.1 was increased in multiple values and the effect on the amplitude of the absorption coefficient was observed. In the presence of a rough surface, viscosity increases close to the walls. The boundary viscosity increase can be

heightened by the depth of the surface roughness [113]. Fundamentally this approach is necessarily pragmatic noting the difficulty quantifying roughness in the first instance.

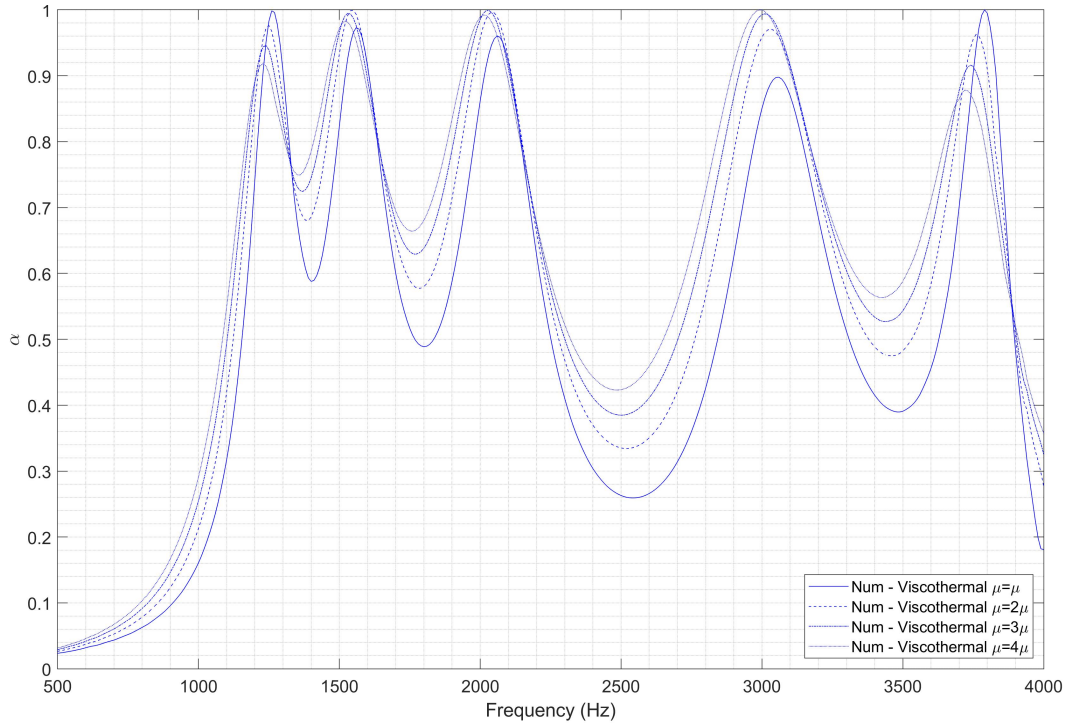

Figure 2.20: Effect of increased dynamic viscosity on the combined length DE-NORMS system determined numerically.

Some equivalent fluid models, use analytical expressions dependent on the geometry of the pore or slit to express dissipative losses in the model. An analogy can be made between increasing the viscosity and reducing the hydraulic diameter through the definition of static flow resistivity. This has been commonly used to characterise porous media. Through the use of reduced order models this is equivalent to reducing the hydraulic diameter assuming Poiseuille's law. The increase in surface roughness which is a result of the manufacturing technology employed increases the wetted perimeter of the geometry. Therefore the simplistic assumption of reducing the hydraulic diameter to demonstrate the effect of increased surface roughness would appear to be valid.

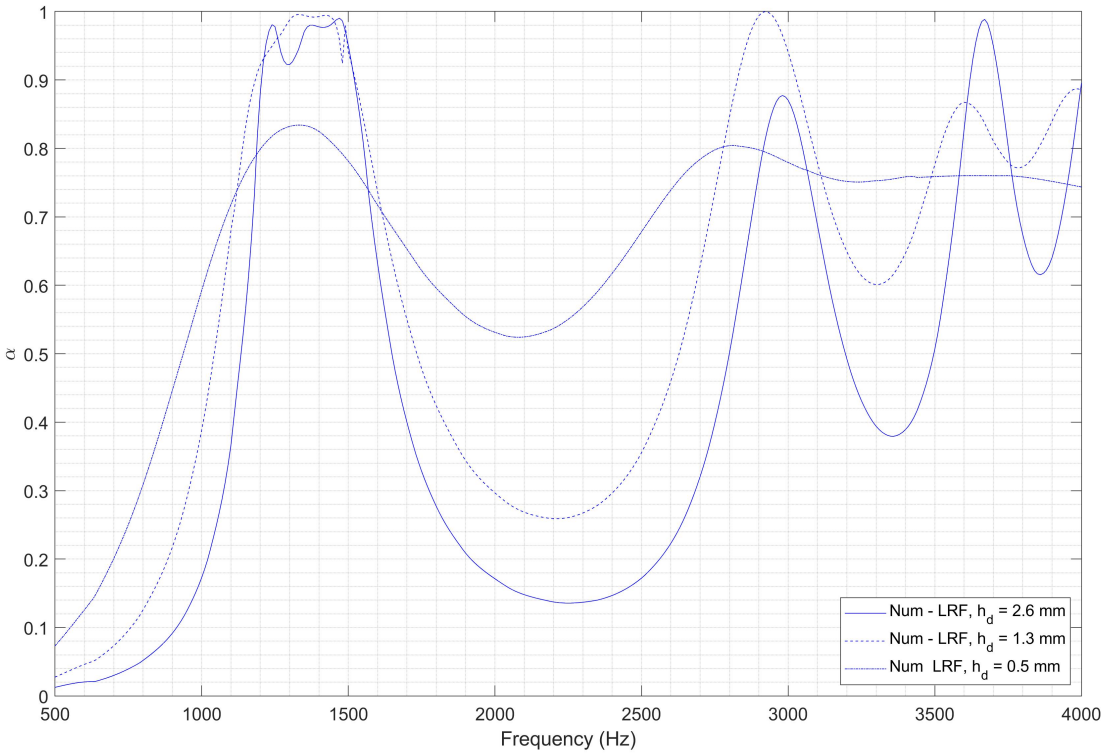

Figure 2.21: Absorption coefficient determined by LRF model at different values of H_d.

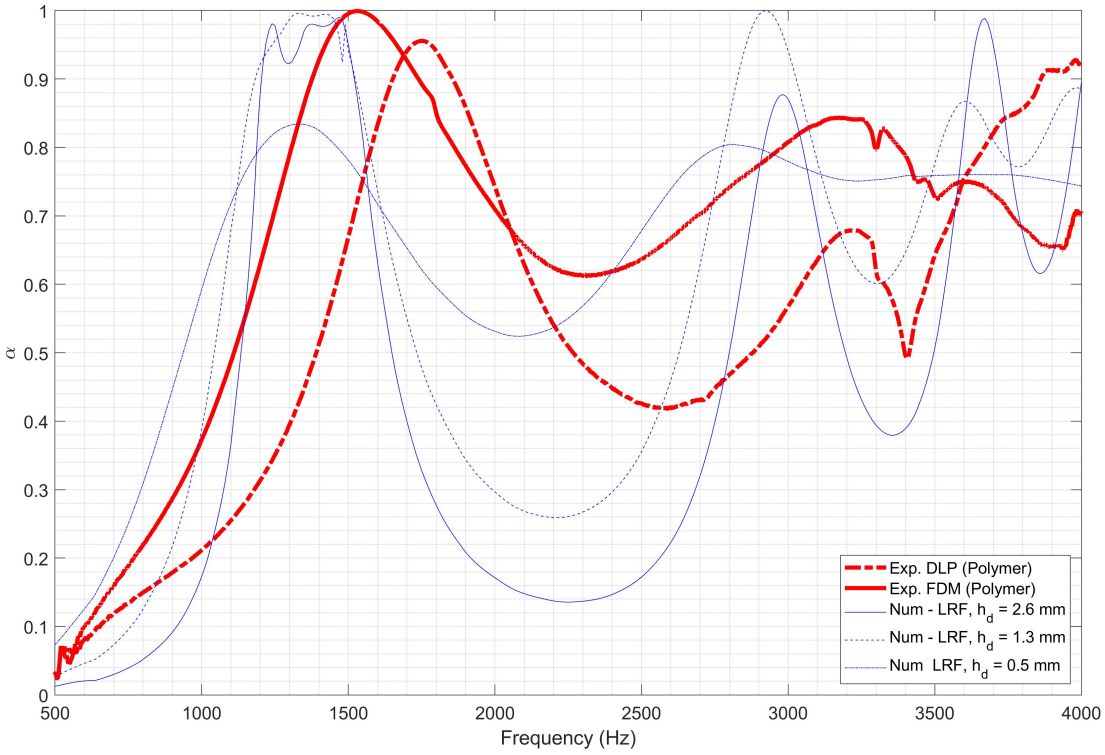

Figure 2.22: Comparison of experimental measurements from additive manufacturing with LRF models.

This rationale was used with the low reduced frequency model wide duct approximation model from Equation 2.39 to evaluate this effect.

$$k_{eq} = \frac{\omega}{c}\left(1 + \frac{B}{2}\sqrt{\frac{\pi}{\jmath\omega}}\right) \tag{2.39}$$

Where $B = \frac{4}{H_d}\sqrt{\frac{\mu}{\pi\rho}}\left(1 + \frac{\gamma-1}{\sqrt{Pr}}\right)$ and the Prandtl number is $Pr = \frac{\mu C_p}{\kappa}$.
The space coiling DENORMS system of mixed length depths is presented in Figure 2.21 starting from the nominal value of $H_d = 2.6mm$ and substituted in Equation 2.39 to compute the propagation via the complex wave number in the Helmholtz equation. The numerical results for different values of H_d plotted in blue were compared with different polymer samples in red in Figure 2.22. It can be seen that the most broadband absorptive behaviour was clearly visible in both the FDM and DLP samples which had lower printing resolution than the SLM technology used in Figure 2.19. The results obtained using the wide duct approximation available in COMSOL showed that for the nominal hydraulic diameter value, the absorptive peaks were merged together from 1200 Hz to 1550 Hz compared with a viscothermal formulation. As this value was reduced in the numerical simulation, the absorption obtained also became more broadband. The correspondence with experimental results became closer which confirmed that roughness increased the viscous dissipation in the system. The other design modification presented in Figure 2.4 is a labyrinthine structure where the path created doubled the number of resonating chambers of the baseline 10 layer deep DENORMS structure. Substituting D for the value of 20 yields a value of $f_{\alpha_1} \approx 610Hz$ in Equation 2.38. Figure 2.23 shows the absorption coefficient obtained for that system numerically and from experimental measurements obtained using other printing technologies. Cross-linking branches were included in the design to allow for resin removal in the DLP sample and excess powder in the SLM sample. The first resonant peak was concurrent for the SLM, FDM and DLP samples with the numerical result. However, the SLM sample deviated for the frequency of the second peak. The deviation observed for the SLM sample could be explained by the partial failure of the SLM sample which necessitated some post processing to ensure a clean fit inside the sample holder. The plot achieved for the viscothermal model matched the predicted first resonant peak of the system. The result suggested for the sample manufactured at the same depth size which was of 10 layer, 50 mm deep material, showed it behaved as if the depth was doubled. This

achieved an absorption coefficient of 0.85 for a low frequency of 610 Hz. Using thsi space-coiling labyrinthine structure it allows to obtain near perfect absorption at low frequency.

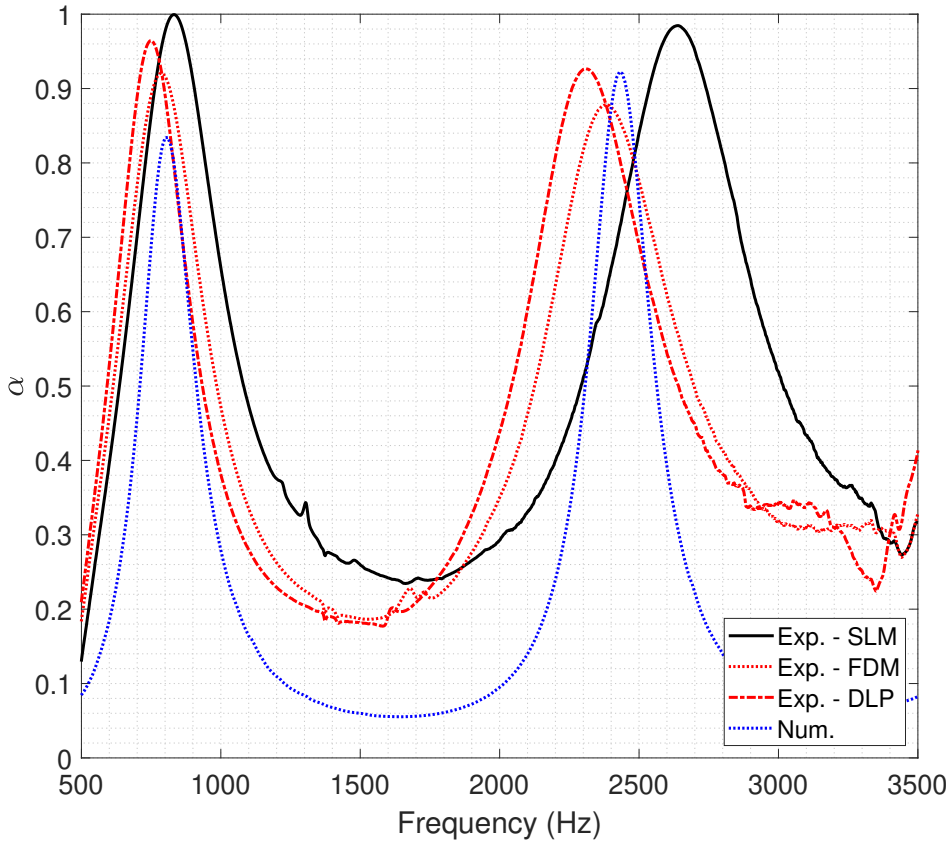

Figure 2.23: Absorption coefficient for a 10 layer depth of the labyrinth DENORMS cell (equivalent to a 20 layer depth) [53].

2.4.5 Conclusion

The study performed was part of a wider project across multiple laboratories to examine the suitability of 3D printing acoustic metamaterials using a benchmark design [74]. Experimental results obtained were shared and compared with other samples with the same cellular design. The deviations in the observed acoustic response could be due to a combination of shape and surface imperfections, as well as microporosity induced by some of the manufacturing processes. However this design was easily reproduced and was thus suitable for additive manufacturing. Four different additive printing technologies which range from low cost desktop printers to state of the art machines were used in this validation. These included three polymer based samples (FDM, DLP and SLA) and a cobalt-chrome SLM sample. While the numerical results matched well

with experimental measurements, deviations were to be expected due to effects which arise from the printing process employed. Explanations of these were provided as well as metrics that can be used to explain the impact roughness could have on the acoustic performance of the samples. From experimental measurements, the SLA sample was close to the SLM sample produced for different designs albeit it was significantly less expensive to produce. SLA technology is capable of reproducing complex designs of high fidelity. With respect to the locations of resonant frequencies both the SLA and SLM samples were in close agreement with the numerical models. As regards the amplitude of the absorption coefficient, the numerical models underpredicted it but the microporosity on the surface which existed in the printed materials was not included in the modelling strategy. The discrepancies between experimental and numerical became more significant with certain alterations in the design, explained by resin entrapment in additive manufacturing techniques. From this study it could be concluded that it was possible to realise validation materials using some low cost polymer printing technology. The achieved acoustic performance will differ depending on the additive technology employed. With greater complexity in the design other issues may occur that can create blockages and limit the obtained fidelity of the design. From a numerical standpoint, in such small geometries it is vital to accurately model the losses within the system which is preferably done through full viscothermal modelling. However this methodology comes with a substantial high computational cost. For this reason, it is of major interest within both the research community and from a design aspect to come up with efficient modelling alternatives to include viscothermal losses. Some models have been explored which are destined to be used for constant cross-sections and it was found that they perform well for the DENORMS design. This study considered an idealised unit cell which from the results observed led to underprediction of acoustic performance. Concentrating efforts on predicting the behaviour of printed acoustic metamaterials by including roughness metrics might be a vain attempt as there are many additional variables to take into account as well as a lack of repeatability of printing processes.

2.5 Summary

This chapter described all the physical theory of linear acoustics as well as the numerical modelling tools that are used to design acoustic metamaterials. A large part of this chapter reposed on a study of a benchmark acoustic metamaterial and to also assess its suitability to both numerical modelling and additive manufacturing. Viscothermal modelling was discussed as well as the importance of using more efficient modelling tools which include dissipative losses. The development of additive manufacturing has allowed the exploration of more complicated shapes but a difficulty resides in predicting their behaviour. Although their performance is desirable, it may be possible to achieve similar broadband behaviour at low frequency using more traditional manchining. This would eliminate some of the manufacturing issues which were discussed and be more suited for large scale industrial production.

Chapter 3

Numerical characterisation of a sub-wavelength acoustic "metaliner" including viscothermal losses

3.1 Introduction

In this chapter, the sound absorptive performance of a proposed "meta-liner" was investigated. It was discussed previously that there can be difficulties in predicting the acoustic response of 3D printed metamaterials. Therefore in this section a structure which could be manufactured using more traditional manufacturing methods without compromising on the desired acoustic response was investigated. The structure was composed of closely placed aluminium plates connected by openings at alternating locations in a stacked format. The majority of the energy dissipation in this design was provided by the gaps between the plates instead of the pores. Results obtained from this study were published in [50]. Wieglhofer and Lakhtakia defined metamaterials as "macroscopic composites having a man-made three-dimensional, periodic cellular architecture designed to produce an optimised combination not available in nature of two or more responses to a specific excitation" [34]. Attractive low-frequency acoustic metamaterials feature a cellular size which is significantly smaller than the wavelength [114]. In recent times there has been a strong focus within the research community on the development of acoustic metamaterials for sound mitigation. Noise reduction in aeronautical applications through the use of acoustic metamaterials is being explored [37]. This development has been aided by continued advancements in additive manufacturing technologies, which has made it more accessible to experimentally assess the acoustic characteristics of complex printed geometries. Nonetheless, additive manufacturing technologies such as selective laser melting (SLM) remain expensive. With SLM, the printed sample can exhibit inconsistent material properties due to powder fluctuations[72]. Therefore the measured acoustic response of the structure created via additive manufacturing technologies, such as SLM, may not conform with numerical predictions. In particular the surface roughness inherent to the printed component can be challenging to model. For these reasons, exploring designs that can be manufactured with traditional methods is interesting, such as multi-degree of freedom liners that show promising absorption performances at low and broadband frequency. The "meta-liner" structure explored in this work targeted sub-wavelength behaviour which was achieved by the tortuous path created through the perforated layers. The suitability of the transfer matrix method for obtaining absorption performance of multiple layers of staggered perforated plates was assessed. The transfer matrix approach was

based on detailed numerical simulations of a unit cell composed of a perforated plate, air gap and the subsequent perforated plate of differing hole location.

3.2 Numerical modelling

The perforated panels were represented by a unit cell composed of a first plate of 1 mm thickness with same sized 3 mm diameter holes and a 2 mm thick air gap, the next adjoining plate was composed of the same thickness and perforations sizes with a different perforation pattern as is presented in Figure 3.1. This design was chosen

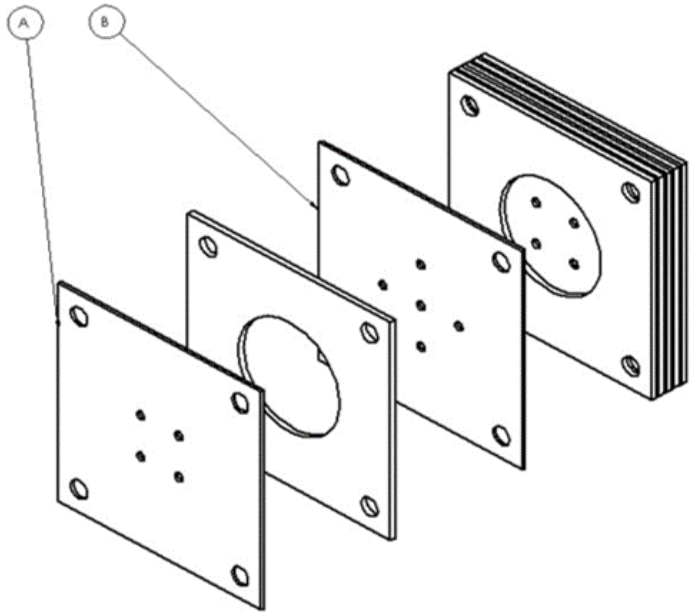

Figure 3.1: Perforated plates configuration, 40mm diameter sample. Plates labelled A (4 holes) and B (5 holes) to represent the different hole pattern on the plate.

as it maximised the usage of available space, the tortuosity lowered the first resonant frequency. Numerical models were developed on a 16 mm deep structure of the chosen design and compared with 16 mm structures where hole locations of cavity separated plates were in phase. Results obtained from Figure 3.2 confirmed the effectiveness of this design in lowering the resonant frequency peaks.

A 3D numerical model of the representing unit cell was created using COMSOL Multi-physics [78]. Numerical models of the unit cell up to a 16 mm deep structure were developed in COMSOL. Two different modelling approaches were taken, one which included a 5 mm manifold which acted as a waveguide and preceded the entrance into the resonator and one which replicated the unit cell adjusting for porosity.

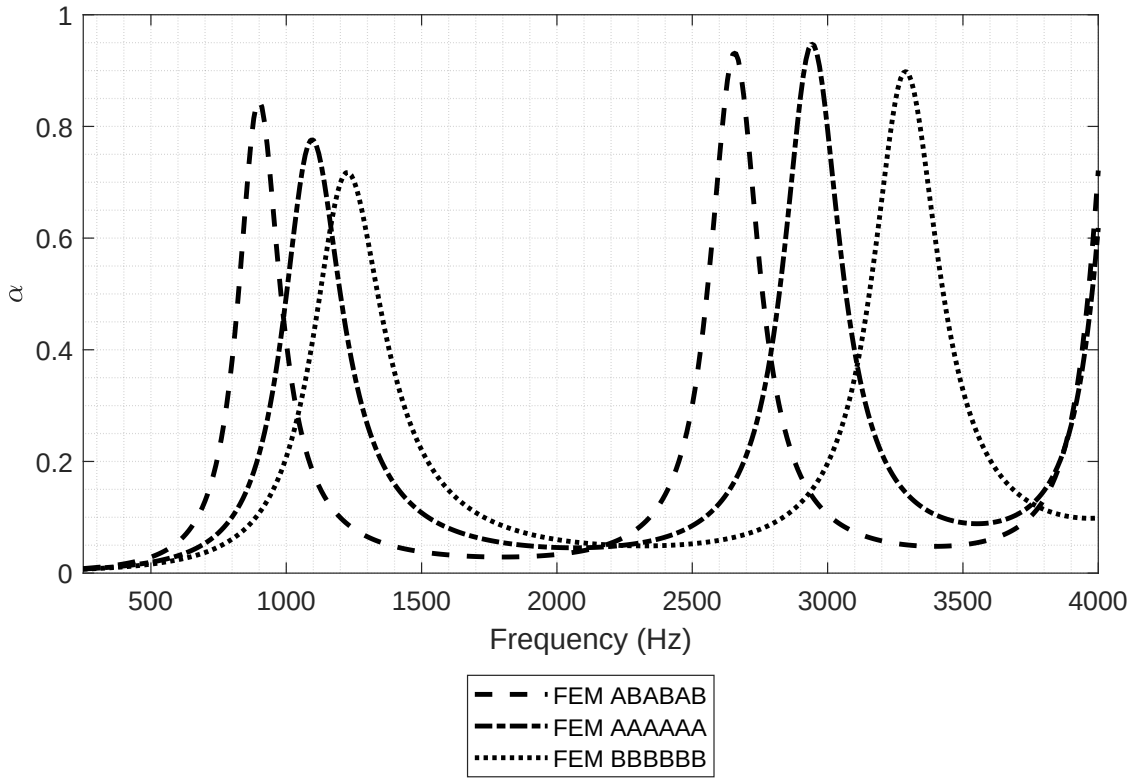

Figure 3.2: Comparison of calculated absorption coefficients for a 16 mm deep structure of plates labelled A and B as per figure 3.1 with porosity correction and a reflective backing termination for a staggered design (ABABAB), and direct paths (AAAAAA) and (BBBBBB)[50].

These models are based on the linearised Navier-Stokes equations without flow which includes viscothermal losses. Acoustic losses need to be considered for metamaterials in the millimetre scale where viscous effects are dominant. In the case of multiple layers of perforated plates, the viscothermal formulation on built up models becomes computationally unfeasible. The viscothermal formulation of sound propagation includes 5 degrees of freedom (DOF), $(p, T, \mathbf{u})$ versus 1 DOF (p) for a helmholtz equation.

3.2.1 Finite Element Modelling

The linearised version of the Navier-Stokes equations describing acoustic propagation were discretized using second order Lagrangian elements with quadratic shape function interpolation for the velocity field and temperature nodal variables and linear interpolation for the pressure variable as previously described in Section 2.3.1. The air

parameters used in this study are detailed in Table 3.1. In both modelling approaches

Symbol	Value	Unit
T_0	293.15	K
p_0	101325	Pa
ρ_0	1.2043	kg/m^3
μ	1.8140e-05	$Pa.s$
μ_b	0.6μ	$Pa.s$
C_p	1005.4	$J/(kgK)$
κ	0.0258	$W/(mK)$

Table 3.1: Properties of air used in 'metaliner' study.

used, a quarter model of the unit cell was designed using symmetries. Two test cases were used at the outlet for both modelling approaches, one with a no slip wall where **u**=0 and T=0 and in second instance with an outlet pressure of 0 Pa. In one approach, a 5 mm long manifold was used in front of the resonator excited by a plane wave with a pressure field of 1 Pa, Figure 3.3 reports the velocity distribution at 3500 Hz for this set-up. The manifold was governed by the Helmholtz equation (no loss modelled). And the cell domain was governed by a viscothermal formulation. At the cell entry, the governing physics were coupled between the two domains. The system impedance was

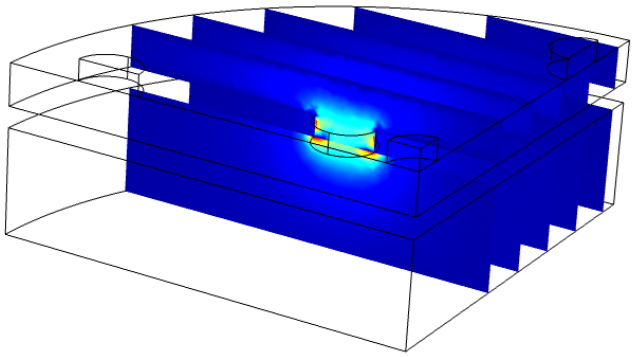

Figure 3.3: Velocity distribution of unit cell including a manifold at 3500 Hz, no slip wall outlet[50].

obtained from the surface averaged velocity $\overline{u}$ reported at the inlet of the manifold.

$$Z = p_i/\overline{u} \tag{3.1}$$

When using a manifold, the impedance translation theorem [108] was used to report the impedance and reflection coefficient at the entrance to the resonator. The manifold allows to take into account some entry effects that can otherwise be ignored. In a second approach, where no waveguide was used, a velocity loading of 1 m/s was used on the entry surface of the perforate. The system impedance obtained through surface averaged values of pressure and velocity field was corrected by the surface porosity from plate A, $\sigma = 0.022499$ [100].

$$Z = \frac{p_i}{\overline{u}}/\sigma \tag{3.2}$$

The absorptivity can then be reported using

$$\alpha = 1 - \left| \frac{Z - \rho_0 c}{Z + \rho_0 c} \right|^2 \tag{3.3}$$

where c is the sonic speed given by

$$c = \sqrt{\frac{\gamma p_0}{\rho_0}} \tag{3.4}$$

and the ratio of specific heats γ is set at 1.41.

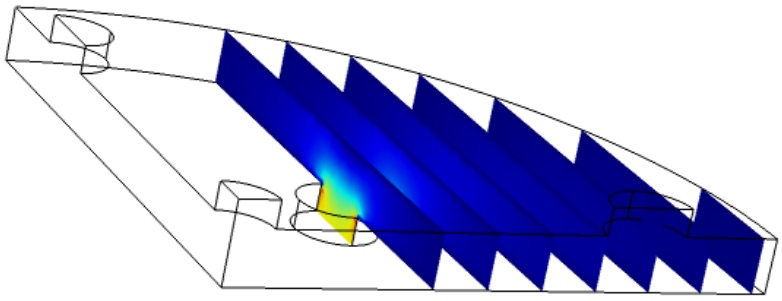

Figure 3.4: Velocity distribution at 3280 Hz, no slip wall outlet

Figure 3.4 reports the propagation velocity through the unit cell with a no slip wall boundary at the outlet. When modelling narrow cavities it is important to incorporate boundary loss mechanisms. Kirchhoff [81] and Rayleigh [98] investigated sound propagation through infinitely long narrow tubes. It was determined that boundary

layer effects on the tube's walls emerging from the air's thermal and viscous properties should be included in the solution. As sound propagates through a fluid cavity bounded by rigid walls, a no-slip boundary condition applies at the wall where the tangential velocity particle at the wall is zero. The viscous boundary layer which exists has a characteristic thickness δ_{visc}.

$$\delta_{visc} = \sqrt{\frac{2\mu}{\omega\rho_0}} \tag{3.5}$$

The thermal boundary layer is the resultant of heat exchanges between the fluid and the walls which has for characteristic thickness δ_{therm}.

$$\delta_{therm} = \sqrt{\frac{2\kappa}{\omega\rho_0 C_P}} \tag{3.6}$$

In air, the Prandtl number is the ratio of these lengths $P_r = \delta_{visc}^2/\delta_{therm}^2$ and is $\sim$ 0.7.[99]. The viscous boundary layer thickness is used as a meshing control parameter at the boundaries. A mesh convergence study was performed where the nodes were increased from 12,506 nodes to 242,992 nodes, see Figure 3.5. The reported absorptivity was used as a metric to assess the sensitivity to further refinement, no further refinement was possible on the workstation used due to out-of-core memory. The study performed showed that the solution had yet to converge however due to computing power available no further refinements were possible. All results reported were based on the simulations carried out with refinement 3 in Figure 3.5. To optimise computational run time in a wideband sweep, a model order reduction technique available within COMSOL was used. It calculates a low-order Padé approximation on small frequency intervals for a chosen output expression. The approximation is calculated for the limits of the interval and the result is then evaluated and compared with different points in that interval [115, 116]. If the result is within an accepted tolerance the interval is approved, if not then the interval is bissected and the procedure is repeated.

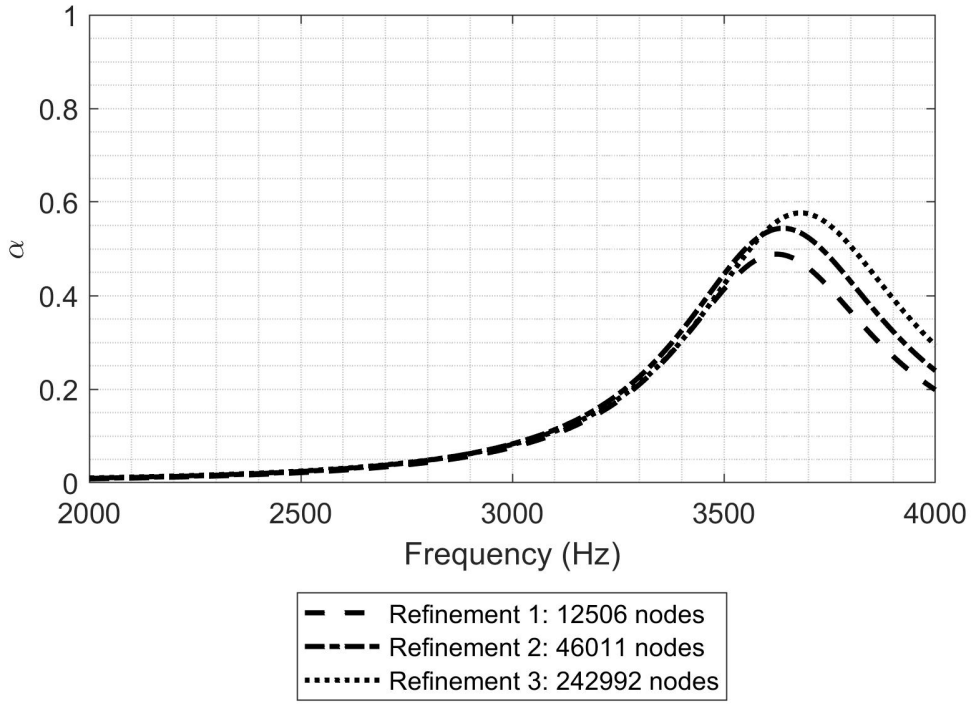

Figure 3.5: Mesh convergence study - Single unit - Absorption coefficient α

3.3 Transfer matrix method

The transfer matrix method (TMM) involves relating input and output acoustic variables of a medium by use of propagation equations.[104, 117]. The acoustic field in the fluid medium can be represented by a two-port network in Figure 3.6, where the variables p and u can be associated by the following matrix relation.

$$\begin{bmatrix} p_i \\ u_i \end{bmatrix} = \begin{bmatrix} T_{11} & T_{12} \\ T_{21} & T_2 \end{bmatrix} \begin{bmatrix} p_o \\ u_o \end{bmatrix} \tag{3.7}$$

Where $\begin{bmatrix} p_i & u_i \end{bmatrix}$ is the state vector at the inlet and $\begin{bmatrix} p_o & u_o \end{bmatrix}$ at the outlet of the fluid layer. And **T** is the system transfer matrix. By imposing end conditions for the outlet velocity and in a second time for the outlet pressure, it allows the transfer matrix parameters to be written as ratios of the acoustic variables. In the case of the resonator in Figure 3.7, a normal velocity of $u_1 = 1m/s$ was imposed on the system. Two test cases were performed numerically, one where $u_2 = 0m/s$ and another where $p_2 = 0Pa$. The surface averaged acoustic variables upstream and downstream of the

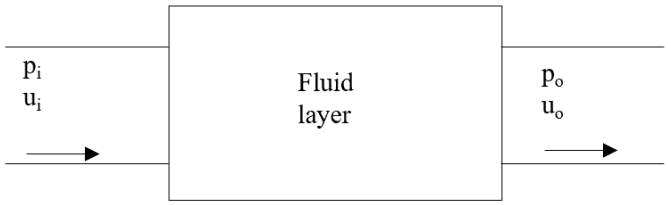

Figure 3.6: Block diagram of the unit cell - Notations for pressure and velocity fields for an incoming plane wave propagating in the fluid medium

system in Figure 3.7 were recorded to determine the parameters of the transfer matrix $\left[B\right]$.

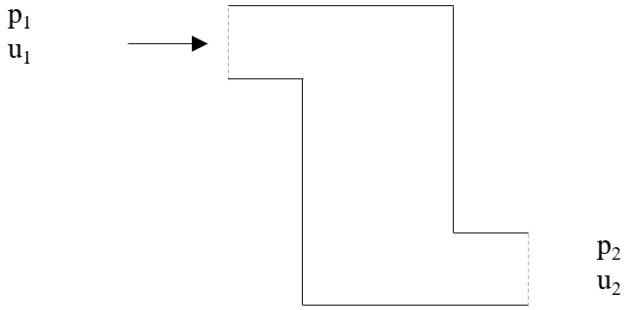

Figure 3.7: Schematic of the unit cell

The parameters of the B matrix are defined as follows...

$$B_{11} = \left.\frac{P_i}{P_o}\right|_{u_o=0} \qquad B_{12} = \left.\frac{P_i}{u_o}\right|_{p_o=0}$$

$$B_{21} = \left.\frac{u_i}{P_o}\right|_{u_o=0} \qquad B_{22} = \left.\frac{u_i}{u_o}\right|_{p_o=0}$$

A global transfer matrix can be constructed from adjacent systems of the same nature as per Figure 3.8. In this case continuity conditions are applied [104]. In the model, the unit cell chosen was comprised of air gaps and perforations so it could be treated as a single entity. Therefore the assembly of the global matrix will depend on the number of subsystems, n, which leads to the following relation.

$$T = \Pi^{n}{}_{i=1} B_i \tag{3.8}$$

The system impedance dependent on the end condition of the system is evaluated as a

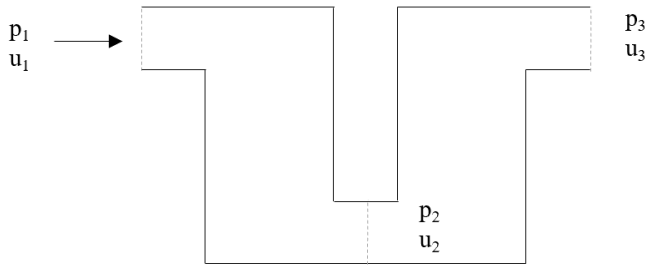

Figure 3.8: Multilayered system

ratio of the the elements of the global matrix $\left[T\right]$. Where the n$^{\text{th}}$element is backed by a hard wall, the system impedance is denoted by Z_c and in a hypothetical case where its open by Z_o in the following equations.

$$Z_c = \left.\frac{T_{11}}{T_{21}}\right|_{u_o=0}^{\text{n}^{\text{th element}}} \qquad Z_o = \left.\frac{T_{12}}{T_{22}}\right|_{p_o=0}^{\text{n}^{\text{th element}}}$$

The system impedance obtained was corrected by the porosity which in this design depended on the first plate configuration A in Figure 3.1. The absorption properties of the built up system using the TMM method, based on numerical simulations of a unit cell were evaluated and compared with experiments in the Results section.

3.4 Experimental set-up

The perforated plates were made from a 1 mm stainless steel sheets for the perforation panel labelled A and B in Figure 3.1, and a 2 mm thick aluminium hollow plate for the airgap. Normal incidence absorption properties α were obtained by impedance tube testing in accordance with the international standard ISO 10534-2:2001 [110]. The sample was placed in the impedance tube as shown in Figure 3.9. A detailed approach of the experimental procedure for the metamaterial study was outlined in Section 2.4.3 and the same procedure was used in this Chapter. The unit cell was tested with a hard backing termination. The tests were repeated for a series of 5 multi-layered systems.

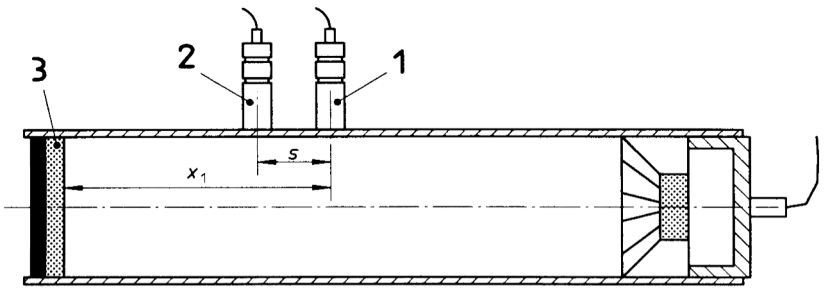

Figure 3.9: Scheme of the impedance tube used to measure the absorption coefficient. 1 and 2 are the two microphones, 3 is the sample, s the inter-microphone distance and x_1 the distance from microphone 1 and the tested sample. From ISO 105345-2:2001[110]

Energy can be lost in the system during experiments by factors such as porosity or internal friction in the material. This will affect the reflection and absorption coefficients evaluated.

3.5 Results

The experimental and numerical results for the closed end test-cases are reported in Figures 3.10 and 3.11. A validation of the TMM approach is also presented.

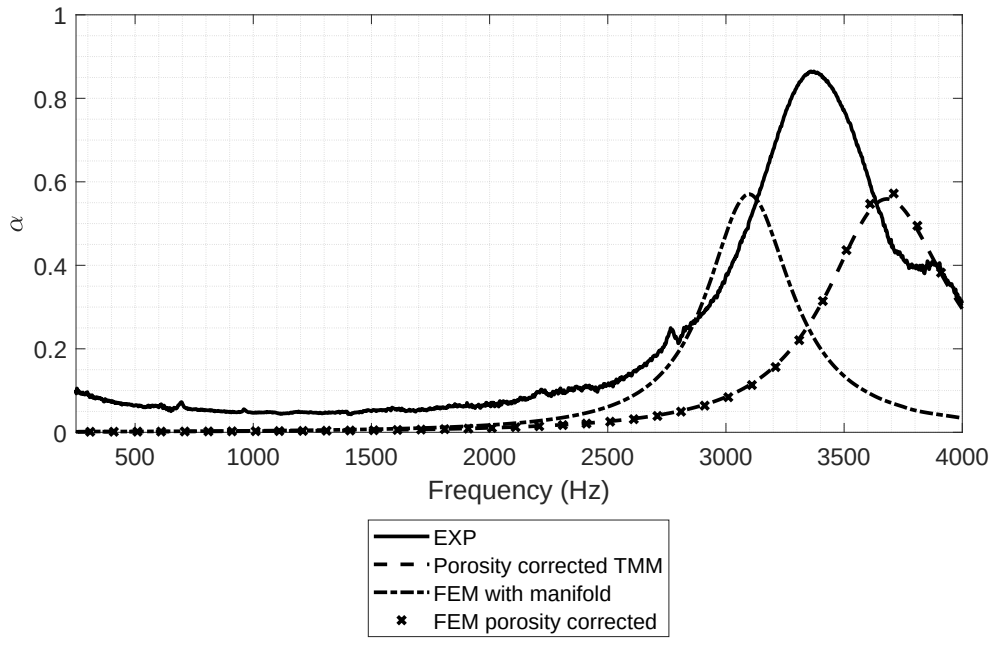

Figure 3.10: Comparison of measured and calculated absorption coefficients via porosity corrected TMM and FEM including a manifold, reflective backing termination

The absorptive properties for the baseline unit cell geometry shown in Figure 3.4, along with FEM results which included a manifold preceding the pore as shown in Figure 3.3 with a hard reflective backing are presented in Figure 3.10. The results from the transfer matrix approach were compared with experimental results which had a resonant frequency $f = 3370H_Z$. There was a shift in frequency between the porosity corrected impedance approach and the FEM model which included a manifold. The shift in frequency between the porosity correction and the FEM model which included a manifold could be explained by the physical set-up of the system. It was separated into two regions, one where the manifold present was governed by the Helmholtz equation, and the other composed of the studied cell governed by a viscothermal formulation. Furthermore there are constriction effects from the waveguide into the entry pore which can explain some differences as well. The loading condition in the FEM model with the manifold was a plane wave with an incident pressure field of 1 Pa whereas the porosity corrected simulations were loaded by a velocity condition. Furthermore the coupling of the equations at the entry to the cell could give rise to a non-physical increase in velocity. The results from the porosity corrected FEM and TMM were almost identical, with a slightly higher amplitude for the TMM method. This was to be expected since the surface averaged state variables were used to construct the transfer matrix. Furthermore, the mesh used in these simulations did not fully converge which is another potential source of error between the experimental and numerical results. The numerical results underpredicted the loss in the system, the losses from the multiphysics approach and porosity corrected model were equivalent. The shift in frequencies could both be explained by some experimental errors and geometric inaccuracies of the manufactured panels. The nominal diameters of the holes measured using a micrometer showed that they vary from 2.93 mm to 3.02 mm, which could explain some of the amplitude difference observed between measured values and numerical results. The introduction of the manifold seemed to lower the resonant frequency. Despite the small errors in peak frequencies, the "Gaussian" shape of the experimental curves are well reproduced by the model. When air flows in and out of the pores, the air surrounding the them will be disturbed on both sides of the plate, which is called the end effect. In the model presented no end correction length was applied. Some analytical solutions have been provided for the end correction. Rayleigh [98] described the correction as

$16r/3\pi$. In addition to this Fok provided a formula which takes into account the interaction of the air in the pore on either side of the plate, this formula multiplied by Rayleigh's definition takes into account the interaction [118].

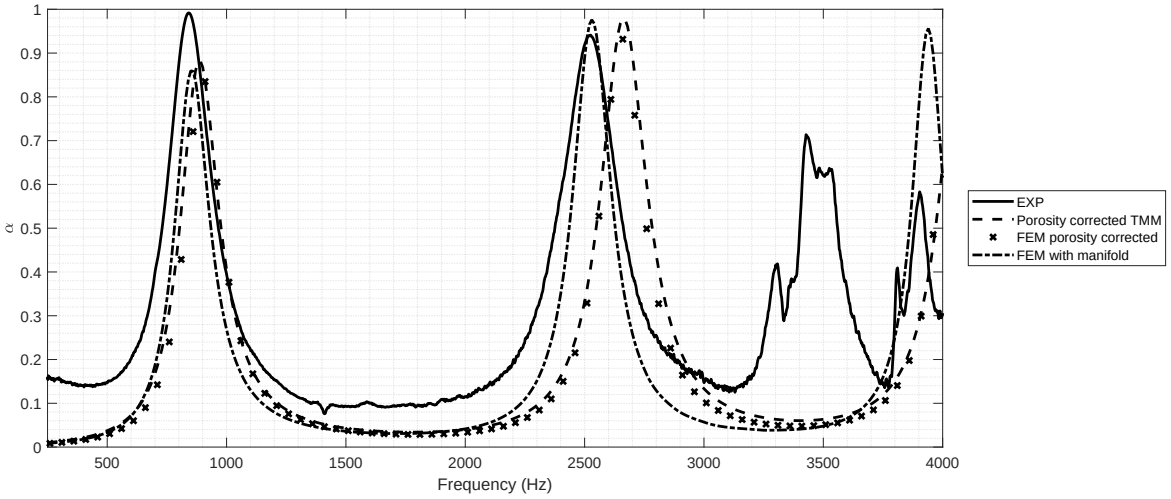

Figure 3.11: Comparison of measured and calculated absorption coefficients via TMM and FEM models for 5 multi-layered units, reflective backing termination

To evaluate the effectiveness of the TMM approach, the global matrix determined by the number of sub-systems required was constructed. The absorption coefficient determined from the TMM approach was compared with experiments and full numerical models of the equivalent built up system, both porosity corrected and with the inclusion of the manifold in Figure 3.11. For the multi-layered system, the absorption coefficient from the FEM with manifold and porosity corrected model showed good agreement with measured values at frequencies below 2000 Hz. Deviations in the experimental results around 3500 Hz are likely due to structural resonances in the plates. As the number of sub-systems increases the deviations observed for a single cell when using different entry assumptions become less important.

In general, the manifold approach underestimated resonant frequencies while the porosity corrected TMM overestimated them. Multiple simulations of various layer combinations were used to investigate this effect as shown in Figure 3.12. It was observed that for increasing cell count the relative error between the two modelling approaches decreased and the prediction for the resonance frequencies converged with the experimentally determined values. Figure 3.12 demonstrated that the influence of the condition used became negligible with increasing structure depth.

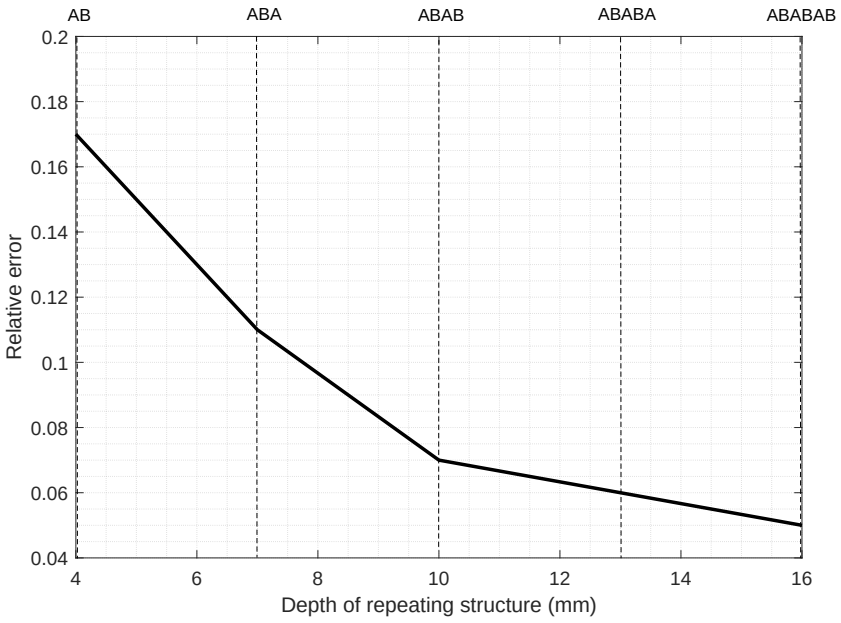

Figure 3.12: Relative error for the predicted value of the fundamental resonance frequency between porosity correction and manifold model as a function of cell depth and corresponding structure

3.6 Conclusion

The absorption performance of a staggered perforated plate system under normal incidence was examined. The system presented multiple resonant peaks with high absorption and sub-wavelength behaviour (sample thickness equals 0.04λ), achieved through tortuosity within the design. The transfer matrix approach based on the unit cell was validated with measured values in an impedance tube and FEM models in a multi-layered configuration. This approach is an efficient modelling tool to create a macro model based on the detailed viscothermal model of the individual unit cell. The FEM and TMM coupling is a viable method which can be extended to model any built-up absorptive structure. The influence of the modelling strategy for the system inlet was investigated. In general it was found that the use of a manifold on the inlet underestimated the resonance frequencies while the porosity corrected inlet gave an overestimate. The divergence in the numerical results deceased as a function of system depth and was found to be negligible for the fundamental resonance in a system of three cells deep. A divergence between the modelling approaches and the experimental results was still observed at the higher resonance modes and may partially be due to numerical convergence issues. The efficiencies obtained from the periodic structure

allows for the development of parametric searches. The present design makes good use of the available cavity space.

Chapter 4

Efficient modelling tools to design multilayered perforated plates

4.1 Introduction

In this chapter, a hybrid numerical methodology for approximating viscothermal dissipation in slits and ducts is presented and an application of this methodology to different multilayered plate configurations is investigated. The designs explored are an extension to the work provided in Chapter 3, in order to achieve more promising absorptive properties at low and broadband frequencies, parametric sensitivity analyses were performed. The hybrid analytical-numerical approach was considered to obtain a more efficient modelling process. This was carried out to accelerate the design loop and obtain sub-wavelength liner concepts which had the benefit of operating at low and broadband frequencies. A similar micro to macro approach was used to predict the sound absorption coefficient of the built-up structures for normal incident sound waves. In the type of geometry considered, the losses occurred predominantly in the air gaps between the plates. The viscothermal effects in the following models were included through simplified modelling of sound propagation for slits and cylindrical tubes. This accelerated the modelling operation as pressure was the only degree of freedom required to determine the sound propagation. The losses were included through an effective density and bulk modulus for the different cross-sectional shapes. To obtain the behaviour of a multilayered system, the transfer matrix approach was used and the response of the overall system was efficiently predicted from the unit cell model which included approximate losses for slits and pores. An optimal air gap thickness was sought which enhanced the dissipation effect created within the design. Several parameters of importance were determined and a sensitivy analysis was performed to enhance the metaliner's performance at low and broadband frequencies. It was concluded in the previous chapter that lengthening the path travelled by the incident sound waves both increased the energy dissipation and reduced the frequencies of the absorption bands in the design. Therefore the tortuosity was deemed to be a critical parameter for the design. This parameter was controlled by the locations of the perforations. The addition of partitions within the plates where hole diameters differ in the quadrants allowed a parallel type behaviour which merge the absorption peaks together. In this design loop the use of reduced order modelling significantly speeds up the design process and allows to explore more configurations. These results were compared with full viscothermal simulations and validated for normal incidence using

PLA printed multi layered plates. The deviations from the manufacturing process were explored with the aid of fluid-structure interaction models and eigenvalue analyses on standalone structural plate models.

4.2 Hybrid analytical-numerical modelling method

Estimating the viscous and thermal interactions between the air and porous materials is not trivial. Allard and Atalla [104] provided a comprehensive description of sound propagation in cylindrical pores which includes parameters to model cylindrical pores in porous materials. When dealing with geometric length scales which are comparable or less than the viscous or thermal boundary layers, there are large velocity gradients thus significant losses which need to be accounted for. A detailed explanation of this occurrence was provided in Chapter 2 which also covered the computational cost associated with the usage of a full viscothermal formulation. Therefore there is merit in using simplified models for circular ducts such as those developed by Zwikker and Kosten [100] and Tijdeman [101] for smaller radii. The model was used by Allard to describe the viscosity effects in cylindrical pores and slits, the thermal conduction can be determined from the viscous effects as worked out by Stinson [119]. The effect of viscosity in a tube with a circular cross-section represented in Figure 4.1 can be evaluated from the momentum equation [104]. The axis of the cylinder is $0x_3$ and the problem is axisymmetrical. At the surface of the cylinder the velocity must vanish which occurs at $r = R$. The velocity across the arc is then given by Equation 4.1.

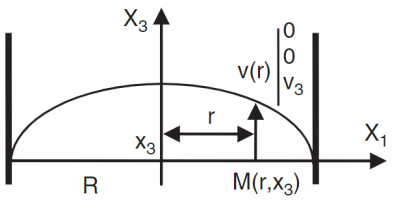

Figure 4.1: Tube with a circular cross-section of radius R [104].

$$v_3 = -\frac{1}{\jmath\omega\rho_0}\frac{\delta p}{\delta x_3}\left(1 - \frac{J_0(lr)}{J_0(lR)}\right) \tag{4.1}$$

where J_0 is the Bessel function of order zero and l is given by the following.

$$l = (-\jmath\omega\rho_0\mu)^{1/2} \tag{4.2}$$

A comparison between the analytical model provided by Allard [104] and a viscothermal model is provided in Figure 4.2. The results are shown for a cylinder of circular cross-section with a nominal pressure loading of 1 Pa at the inlet and 0 Pa at the outlet over 10 mm with a 1 mm radius represented in Figure 4.3. The analytical model only includes viscous effects whereas the numerical model includes both thermal and viscous effects in Figure 4.2. At 10 Hz, the boundary layer observed in Figure 4.3 was

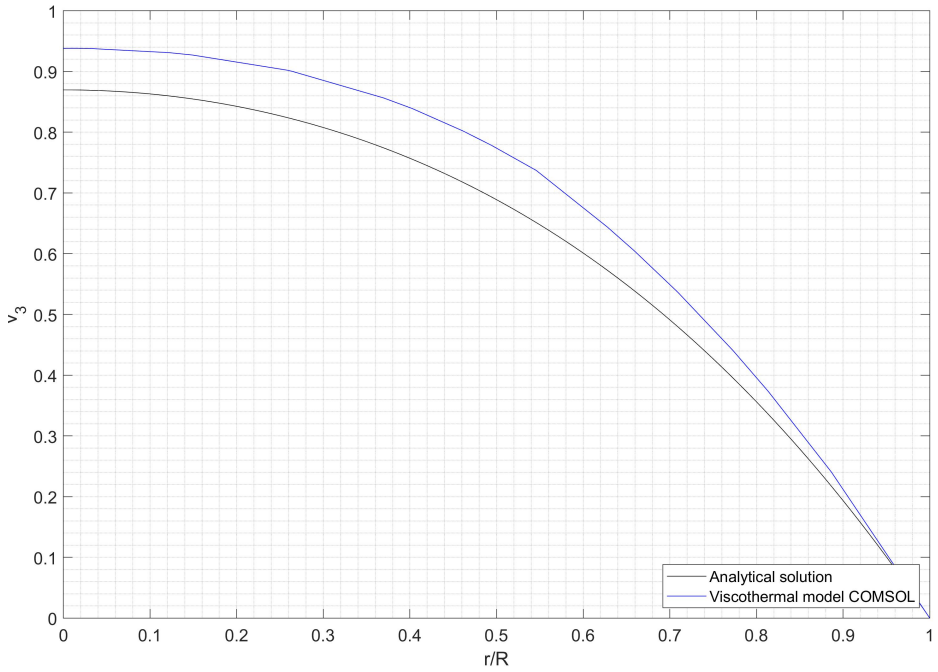

Figure 4.2: Velocity vanishing at $r = R$ determined from Equation 4.1 and compared to a numerical viscothermal model for 10 Hz.

not negligible and the dissipation is homogeneous across the cylinder as it's a frequency domain analysis. From the average value of v_3 over the cross-section it is possible to obtain the effective density of the air in a cylindrical pore as in Equation 4.3 [104].

$$\rho(\omega) = \frac{\rho_0}{1 - \dfrac{2}{s\sqrt{-\jmath}} \dfrac{J_1(s\sqrt{-\jmath})}{J_0(s\sqrt{-\jmath})}} \tag{4.3}$$

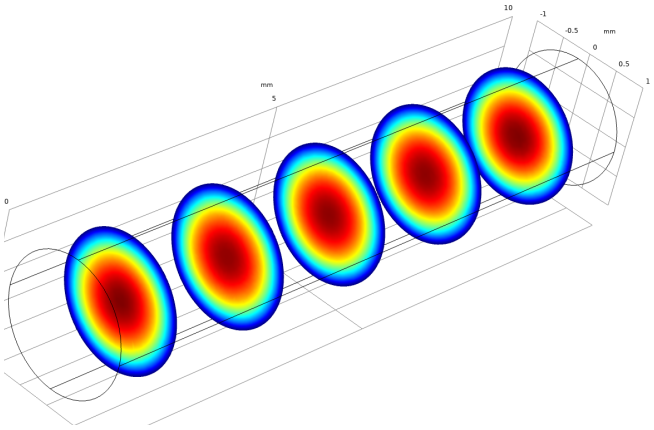

Figure 4.3: Velocity plot of numerical viscothermal model of air propagating through a cylinder of circular cross-section at 10 Hz.

The value of s for a cylindrical pore is,

$$s = \left(\frac{\omega \rho_0 R^2}{\mu} \right)^{1/2} \tag{4.4}$$

The thermal effects associated with the temperature variations in the tube can be evaluated through the bulk modulus. In the case of thermal conduction, the acoustic temperature T vanishes at the surface of the cylinder or slit. The bulk modulus can then be determined through the displacement potential and the continuity equation. For a cylindrical tube of circular cross section it is calculated from the following Equation 4.5. The Prandtl number is defined by $B^2 = \dfrac{\mu}{(\rho_0 v')}$ and $v' = \dfrac{\kappa}{\rho_0 C_p}$.

$$K(\omega) = \frac{\gamma P_0}{1 + (\gamma - 1)\dfrac{2}{Bs\sqrt{-\jmath}}\dfrac{J_1(Bs\sqrt{-\jmath})}{J_0(Bs\sqrt{-\jmath})}} \tag{4.5}$$

The same approach can be used in the case of a slit to obtain the effective density where the velocity vanishes at its surface, in such a scenario the value of s will be different and can be evaluated knowing the porosity and flow resistivity [104].

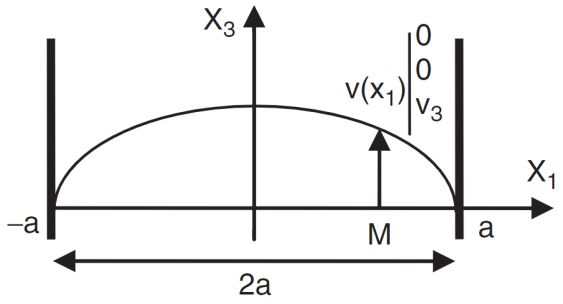

Figure 4.4: Flow propagation in slits with delimited by a and $-a$ in plane $x-1$ [104].

The effective density can be retrieved by integrating the mean velocity in the slit between the bounds represented in Figure 4.4 which results in Equation 4.6 which is used to determine the viscous effects in the models that were investigated in this chapter [104].

$$\rho(\omega) = \frac{\rho_0}{\left[1 - \frac{tanh(s^{'}\jmath^{1/2})}{s^{'}\jmath^{1/2}}\right]} \tag{4.6}$$

The value of $s^{'}$ for a slit is,

$$s^{'} = \left(\frac{\omega\rho_0 a^2}{\mu}\right)^{1/2} \tag{4.7}$$

The bulk modulus for slits equates to the following;

$$K(\omega) = \frac{\gamma P_0}{\left[1 + (\gamma - 1)\frac{tanh\left(Bs^{'}\sqrt{\jmath}\right)}{Bs^{'}\sqrt{\jmath}}\right]} \tag{4.8}$$

The value of the bulk modulus in cylindrical pores and slits respects low and high frequency limits corresponding to its isothermal and adiabatic behaviour [104]. An extension of Equations 4.3 and 4.5 was put forward by Allard [104] which allows to obtain effective mass and air compressibility for cylindrical pores of arbitrary cross-sections through the hydraulic radius, flow resistivity and porosity. An analytical-numerical approach was used in this study in order to have a more efficient modelling tool to design low frequency broadband metaliners. The losses in the gaps were included from the analytical solutions provided by Allard [104]. The losses in the pores in the plate configurations studied don't predominate and taking into account the additional

losses in the pores results in a minimal amplitude increase. The effect of adding the losses occurring in the pores was verified in one of the configuration studied. The effect of describing the effective parameters for both the slits and the pores from the equations outlined in this section provides a minimal squaring process of the amplitude of the absorptivity. An analysis of this effect was numerically investigated with the two loss approximations and compared with experimental values for unit cell AC in Figure 4.5. As it is a simple squared process of the amplitude and the difference was minimal, it was decided that including the losses in the region where their occurrence predominates was the most efficient and valid approach.

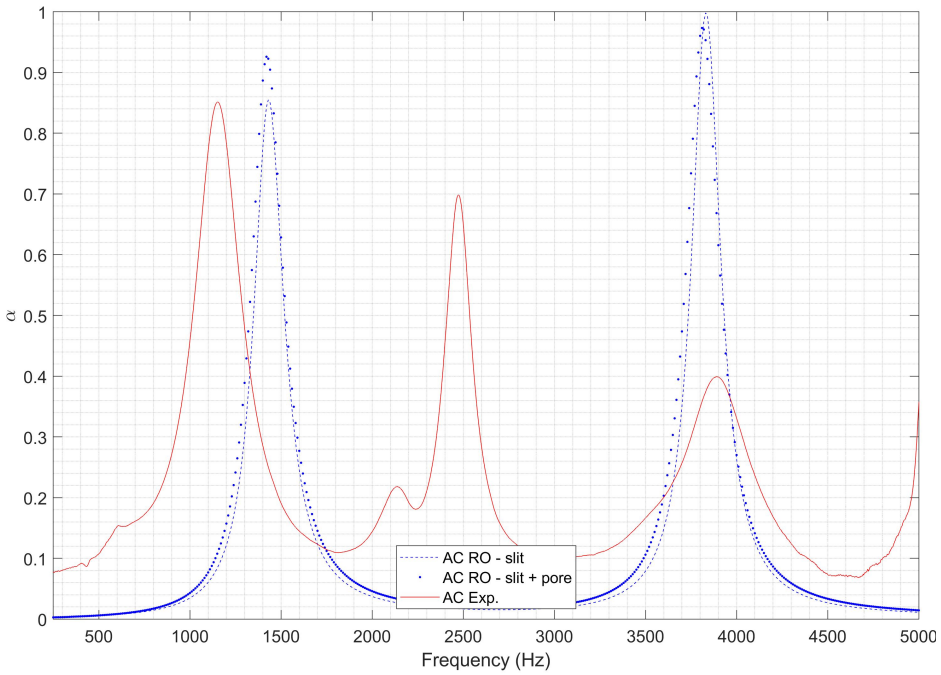

Figure 4.5: Approximation for losses in slits and applied to slits and pores in a unit cell AC.

These losses were included into the model by specifying the speed of sound $c = K/\rho$ and the effective density for the slit. These losses are included through the wave number, $k = \omega \left(\rho/K\right)^{1/2}$ into the Helmholtz equation, where the variational problem is constructed with the appropriate boundary conditions and numerically solved.

$$\nabla^2 p + k^2 p = 0 \tag{4.9}$$

This approach resembles the approach followed to model anisotropic acoustics where the fluid is modelled with an anisotropic density or for metamaterials in a homogenised way [78].

4.3 Description of the designs investigated

The initial design put forward in Chapter 3 showed that by changing the location of the pores on the alternating plates and the number of holes, the first resonant peak occurred at a lower frequency. This staggering of hole locations resulted in a more desirable acoustic behaviour when compared to a direct pathway where hole locations are aligned. As a general objective within the industry, there is an emphasis in developing acoustic liners with increased attenuation at low frequencies for turbofan engines. The multilayered plate designs presented had for objective low frequency-broadband operation. And as such, parameters were controlled to enhance this behaviour in the subsequent studied design configurations. As the losses within the design occur primarily in the gaps between the plates, an optimal thickness was evaluated for the design. Once this was established, other parameters were then analysed to improve the design.

4.3.1 Effect of air gap thickness on energy dissipation

An eighth-2D-model of a plate design shown in Figure 4.6 was constructed to investigate the effect on the absorption produced by the thickness of the air-gap. The approximation of the slit-induced losses derived by Allard [104] were included in this model, by specifying the density and speed of sound of the linear elastic fluid model. The thickness of the air space was specified by Equation 4.7, simulations were performed on different air gap thicknesses. The transfer matrix parameters were retrieved applying appropriate the boundary conditions for the pressure loading of $P_i = 1$ Pa and two outlet test cases. One where the outlet velocity was null and the other where the outlet pressure was $P_o = 0$ Pa. The field variables obtained on a single layer could then be used to construct a transfer matrix to determine the acoustic behaviour of a number of stacked units. The corresponding geometrical dimensions which describe the unit are detailed in Table 4.1, the location of the pores from the plate's centre and their radii are shown in Figure 4.6. As the normal impedance tube used to carry out these experiments had a circular cross-section of diameter 40 mm, this was selected as

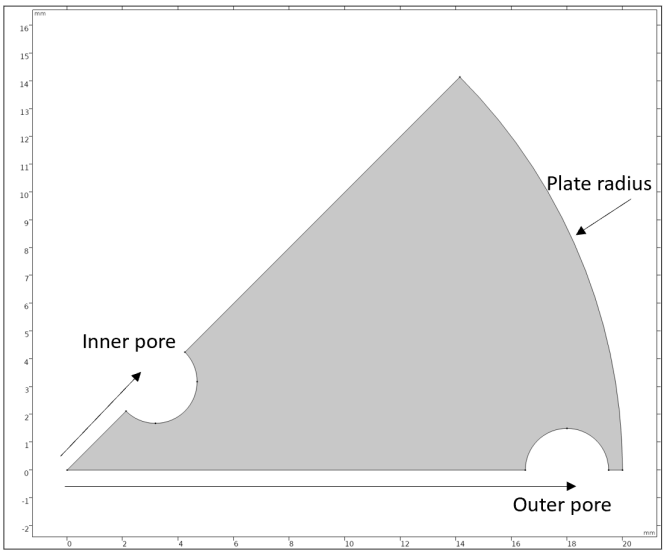

Figure 4.6: Initial 2D geometry which shows the location of the pores (inner and outer holes on different alternating plates).

the circular plate diameter. Simulations were performed with the boundary conditions prescribed above for different air gap heights ranging from 1 mm to 2.5 mm in increments of 0.5 mm. The air parameters which were used in this study are detailed in

Parameter	Value	Unit
Hole radius	1.5	mm
Position of outer pore	18	mm
Position of inner pore	4.5	mm
Plate thickness	1	mm
Spacing between plates	[1.0:0.5:2.5]	mm
Plate radius	20	mm

Table 4.1: Geometric parameters of unit cell in Figure 4.6 used to maximise dissipation in the slit.

Table 4.2.

The transfer matrix method which was previously described in Chapter 3 was used to determine the absorptive behaviour of 8 cells using different spacing dimensions. The absorption coefficient obtained for the different spacing thicknesses between the plates are shown in Figure 4.7. It can be seen that there is an ideal spacing at 1.5 mm which maximises the absorption at around 600 Hz. Further step refinement could have been performed to establish the optimum spacing. The manufacturing constraints associated with this design limited the narrowness of the air gap particularly when 3D

Symbol	Value	Unit
T_0	293	K
p_0	101300	Pa
ρ_0	1.2043	kg/m^3
μ	1.81E-05	$Pa.s$
c_0	343.17	m/s
C_p	1005.4	$J/(kgK)$
κ	0.025756	$W/(mK)$
B	0.84131	-

Table 4.2: Properties used to determine the effective parameters to model sound propagation in the slits.

printing of the PLA plates. Even though the absorptive performance provided by the 1.5 mm air gap had better absorption at the same frequency, it was preferred to use a 2 mm gap spacing for future designs due to manufacturing constraints.

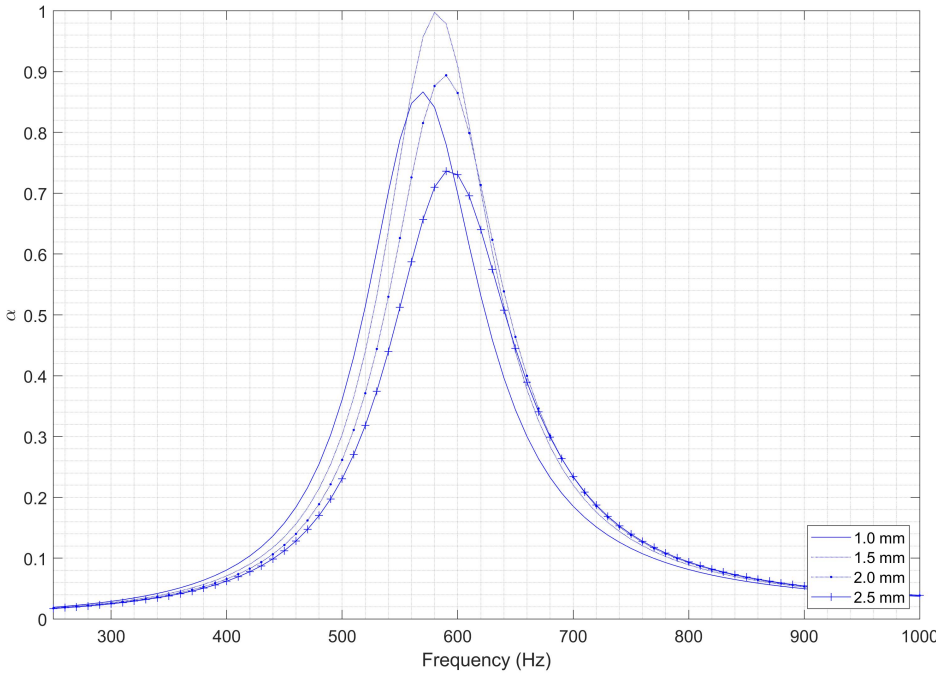

Figure 4.7: Effect of airgap thickness on the dissipation for a configuration of 8 cells deep, Plate design A.

4.3.2 Preliminary plate configuration: Design 1

A preliminary design configuration shown in Figure 4.8 with the geometrical dimensions outlined in Table 4.3 was printed using FDM technology. The location of the holes was chosen for ease of manufacture. A top and side view of the unit was provided as

the successive designs are based on similar units with slight geometric modifications or additional parameters. A hybrid analytical-numerical approach was followed to obtain the acoustic performance of this configuration using reduced order modelling to encapsulate the losses in the structure using Equations 4.6 and 4.8. A full viscothermal model was also constructed as a comparative measure to study the deviation between both viscothermal, reduced-order modelling and experimental data. The experimental procedure for normal incident plane waves was performed on the sample PLA plates in accordance with international standard ISO 10534-2:2001 [110] for impedance tube testing.

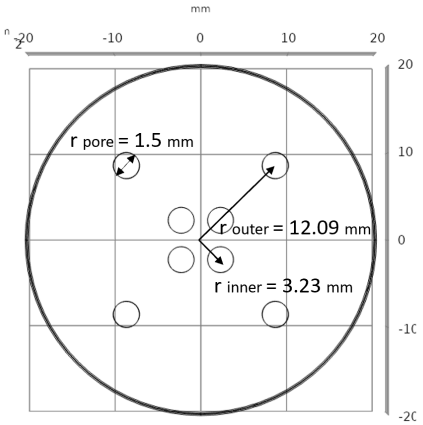

(a) Top view

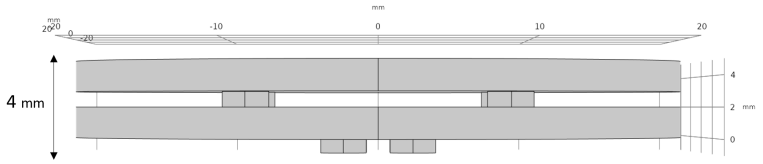

(b) Side view

Figure 4.8: Unit cell defined by the parameters from Table 4.3 with the hole locations refer to the distance from the disk centre to the pore centre.

The measured sound absorption coefficient for Design 1 are presented in Figures 4.9 to 4.11. These experimental measurements are compared with numerical sound absorption estimations obtained using analytical estimation for losses occurring in slits and a full viscothermal simulation. The plates were individually printed using the FDM Prusa Mini +, each PLA plate is a square section of 80 mm and 3 mm thick, a 40 mm diameter from the centre represents the sample under investigation where the thickness

Parameter	Value	Unit
Hole radius	1.5	mm
Position of outer pore	12.09	mm
Position of inner pore	3.23	mm
Plate thickness	1	mm
Spacing between plates	2	mm
Plate radius	20	mm

Table 4.3: Dimension of Design 1.

is 1 mm and the remaining 2 mm composes the airgap. In the experimental set up under normal incident plane wave in the tube, the plates were stacked together and bolted onto to the end of the square section of the tube backed by a solid 20 mm thick piece of aluminium. The same experimental procedure detailed in Section 2.4.3 was followed.

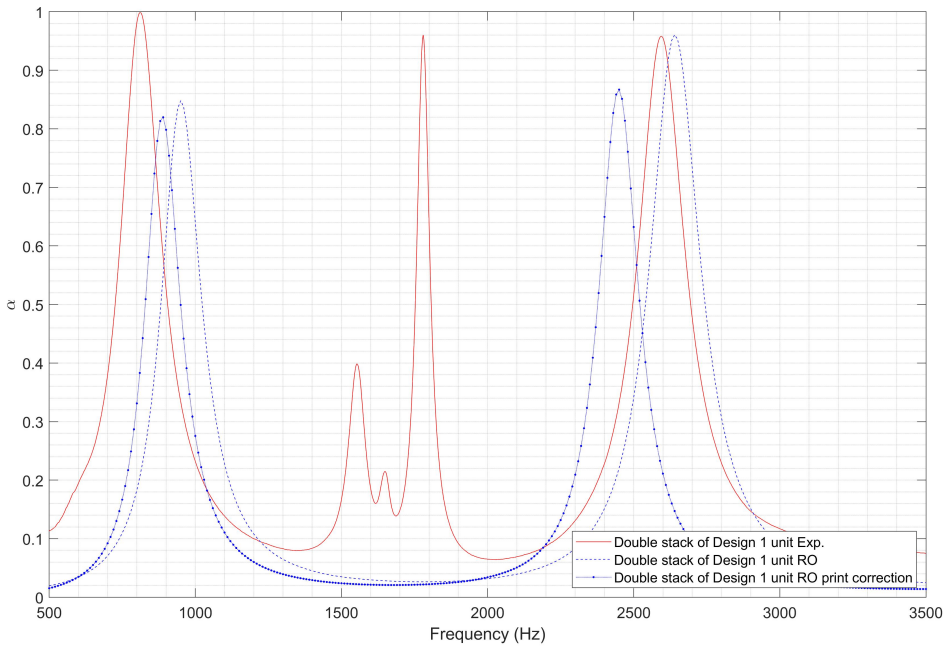

Figure 4.9: Absorption results determined for a two cell deep of Design 1 metaliner using reduced order modelling of energy dissipation in slits with experimental validation on PLA plates.

To account for deviations that arose during the FDM printing process, a print correction was applied to the pore diameter of 0.25mm as the nozzle of the printer is roughly twice that size. Also from user experience printing holes with FDM, the deviation with the prescribed diameter is usually in the 0.25 mm range but can be up to 0.5 mm. With FDM print technology holes printed on the vertical axis will usually

be undersized this is also caused by the nature of the process as a new material layer will be deposited on top of the existing layer, compressing it in the process. Figure 4.9 reports the numerically obtained absorption coefficient using Allard's expression for losses in the slits. The deviation with the print correction is expected and its purpose was to observe whether it had a major impact on the experimentally obtained results. The geometrical deviations are certainly a factor in these deviations but not solely. The numerical models only take into consideration the acoustic behaviour of the combined printed plates, these are measured on four individual units stacked together, they may be tightened in an uneven manner or contain a non homogeneous surface.

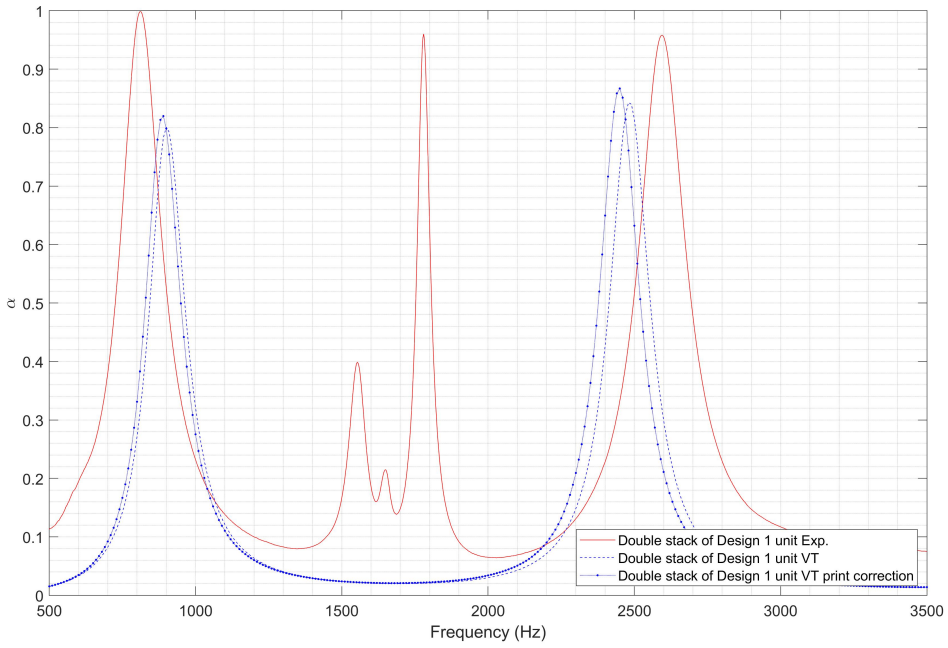

Figure 4.10: Absorption results determined using a numerical viscothermal model for a two cell deep of Design 1 metaliner with experimental validation on PLA plates.

The modes observed from 1500 Hz to 1800 Hz were thought to be of a structural nature which was not modelled at this point. This nature of these modes will be reviewed and discussed in Section 4.5.2. The two acoustic modes at 800 Hz and 2600 Hz are predicted correctly by the numerical results. The first mode was better replicated by the original numerical model whereas the prediction of the second mode was not as reliable as the model may have been more susceptible to print correction. Figure 4.11 shows the absorption coefficient obtained using a viscothermal model that includes adequate meshing refinements around the boundaries with print correction as well as without. The difference between the estimation of the absorptivity using the reduced

order model and the viscothermal model seemed equivalent to adding the print correction, and with respect to the experimental measurements the reduced order model captured well the second acoustic mode which can be seen in Figure 4.11.

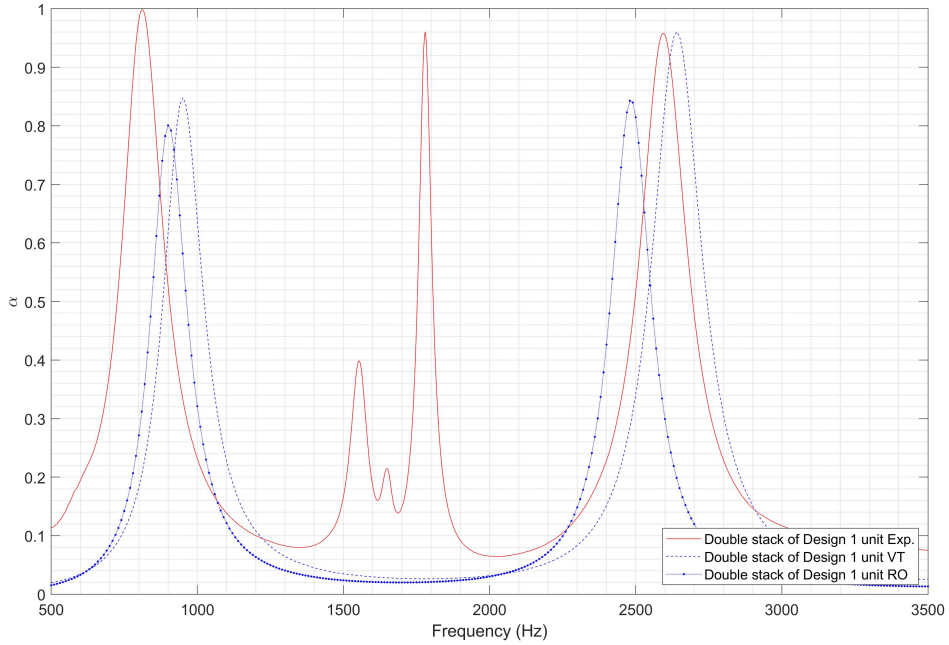

Figure 4.11: Comparison between numerical viscothermal formulation, losses included analytically and experimental validation from a PLA sample of the design.

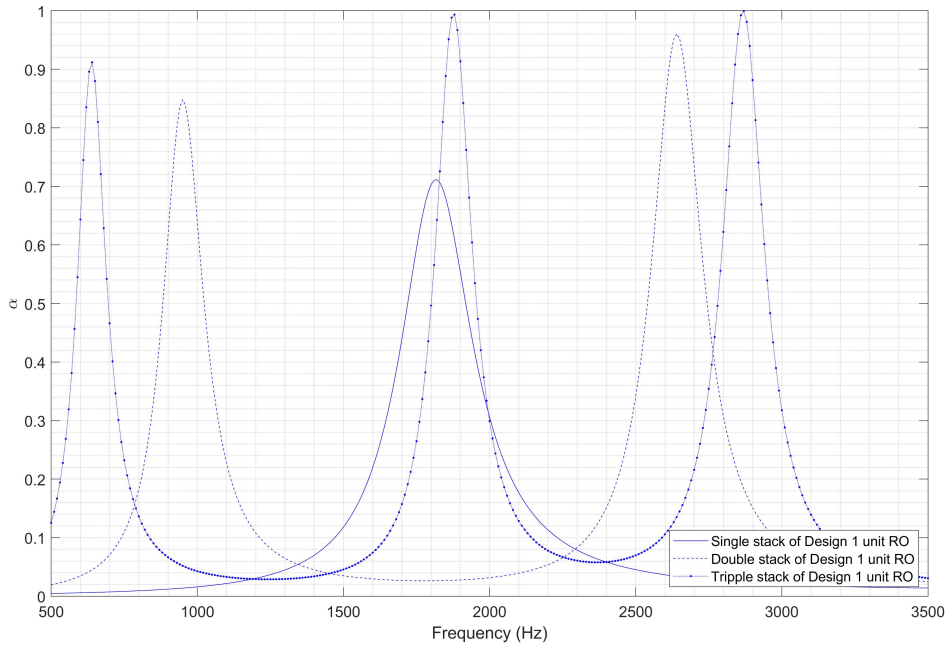

Figure 4.12: Numerically determined absorptivity for unit cell design 1 up to three layers using analytical slit model for the viscothermal losses.

This design was tested firstly using a single unit, and via the transfer matrix method its absorptive behaviour was evaluated for multiple stacked units in Figure 4.12. As the number of units was increased the first resonant acoustic mode occurred at a lower frequency and the peaks produced became increasingly narrow band. Furthermore within the studied frequency range it can be observed that we obtain further resonant absorptive peaks of higher amplitude as the number of units are stacked.

4.3.3 Multilayered panels

Earlier designs informed how best to proceed for future configurations. The parameters that were believed to be the most important were; the location and sizes of the pores as well as the thickness of the plate and air gaps. The following designs have used as naming convention the location of the the holes on the inner and outer plate, the first plate being the one exposed to the incident plane wave. All the plate configurations analysed in this section are similar to Figure 4.8(b), where the only parameters which are modified are the diameter of the pores and the location of inner and outer pores, the naming convention used for the different cells are outlined in Table 4.4.

Parameter	Value	Unit
Position of inner pore, A	4.5	mm
Position of outer pore, B	12.75	mm
Position of outer pore, C	17	mm

Table 4.4: Naming convention unit cells AB and AC refer to the distance centre of plate-centre of pore where A is the first plate and B and C are the outer plates in both separate configurations.

The dimensions for the unit composed of plates A and B are detailed in Table 4.5, where the position is described as the location centre to centre from the plate to the pore's centre. The effect of the pore diameter on the unit was analysed through its absorptive properties obtained through the reduced order model in Figure4.13. Decreasing the pore diameter by 1 mm of all the holes over the two plates decreased the first resonant peak by 400 Hz compared to the larger pore size. And the second resonant frequency in the model composed of holes with $r_{pore} = 1.0mm$ occurred at 3800 Hz whereas for $r_{pore} = 1.5mm$ it was located 5000 Hz.

Parameter	Value	Unit
Hole radius	1 ; 1.5	mm
Position of outer pore, B	12.75	mm
Position of inner pore, A	4.5	mm
Plate thickness	1	mm
Spacing between plates	2	mm
Plate radius	20	mm

Table 4.5: Dimensions of AB unit cell with $r_{pore} = 1.0mm$ and $r_{pore} = 1.5mm$.

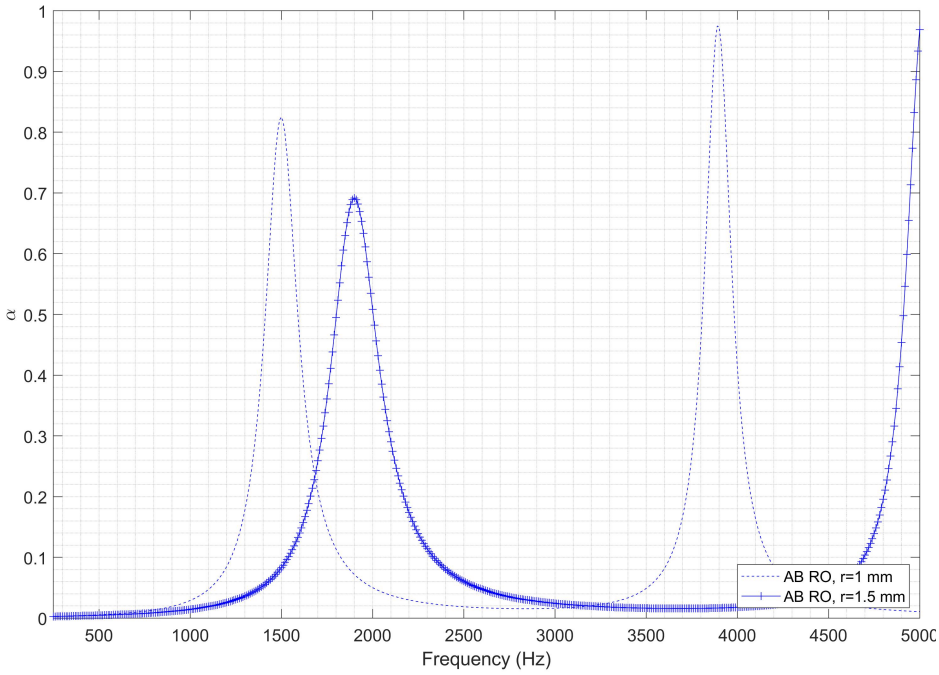

Figure 4.13: Numerically determined absorptivity using a reduced order model for losses in slits for the unit cell AB with $r_{pore} = 1.0mm$ and $r_{pore} = 1.5mm$.

The results obtained with the smaller diameter were compared with a viscothermal model of the same configuration in Figure 4.14. It was observed that the reduced order model slightly overestimated the occurrence of the resonant frequencies compared with the viscothermal model and the difference was more apparent for the second resonant mode.

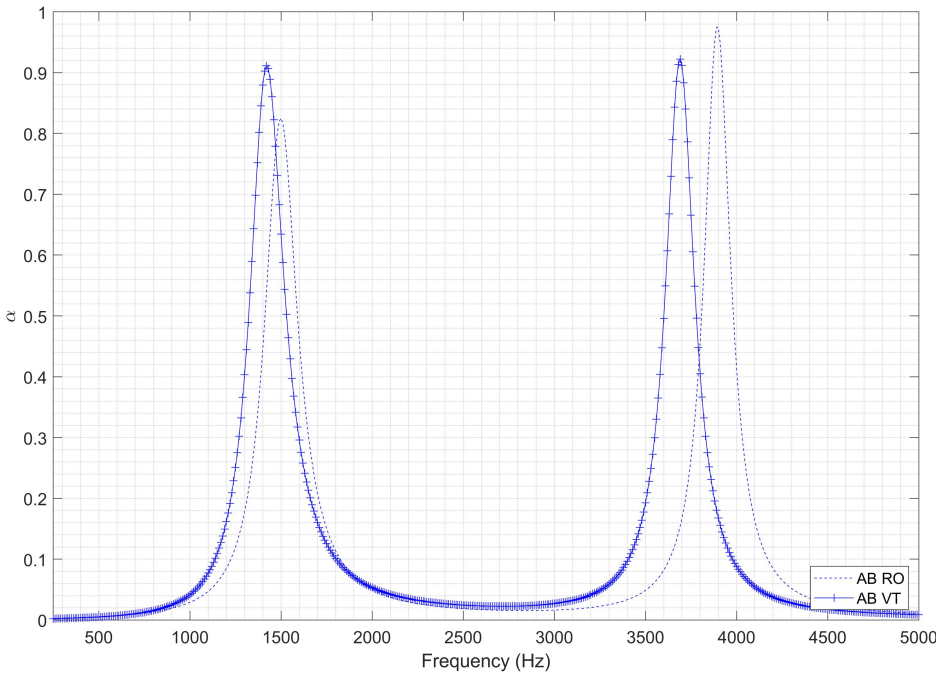

Figure 4.14: Numerically determined absorptivity for unit cell AB of $r_{pore} = 1.0mm$ using analytically determined losses versus a full viscothermal formulation.

Parameter	Value	Unit
Hole radius	1 ; 1.5	mm
Position of outer pore, C	17	mm
Position of inner pore, A	4.5	mm
Plate thickness	1	mm
Spacing between plates	2	mm
Plate radius	20	mm

Table 4.6: Dimensions of AC unit cell with $r_{pore} = 1.0mm$ and $r_{pore} = 1.5mm$.

The plate design which dimensions are specified in Table 4.6 had on the second plate, pores located further to the edge of the sample in order to increase the tortuosity within the design. The numerical prediction of the acoustic behaviour obtained using the outer plate labelled C are presented on a single unit and compared with the preceding AB cell result for the same pore diameter in Figures 4.15. From the numerically predicted absorption results it was observed that the distance increase from the centre of the plate to the centre of the pores located on the outer plate from $B \rightarrow C$ while keeping plate A composed of pores located at a distance of 4.5 mm from the centre had a minimal impact on the configuration in the current set-up. The absorption coefficient was also examined for two AC cells stacked together shown in Figure 4.16, the results obtained

with $r_{pore} = 1.0mm$ have lower resonant frequencies for the three acoustic modes. However, the frequency range difference increased for the second acoustic mode and its difference became larger again for the third resonant acoustic mode. Although the dissipative losses predominated in the gaps some additional minor losses did occur in the pores, the inclusion of such losses should only provide a slight increase in the magnitude of the absorption coefficient.

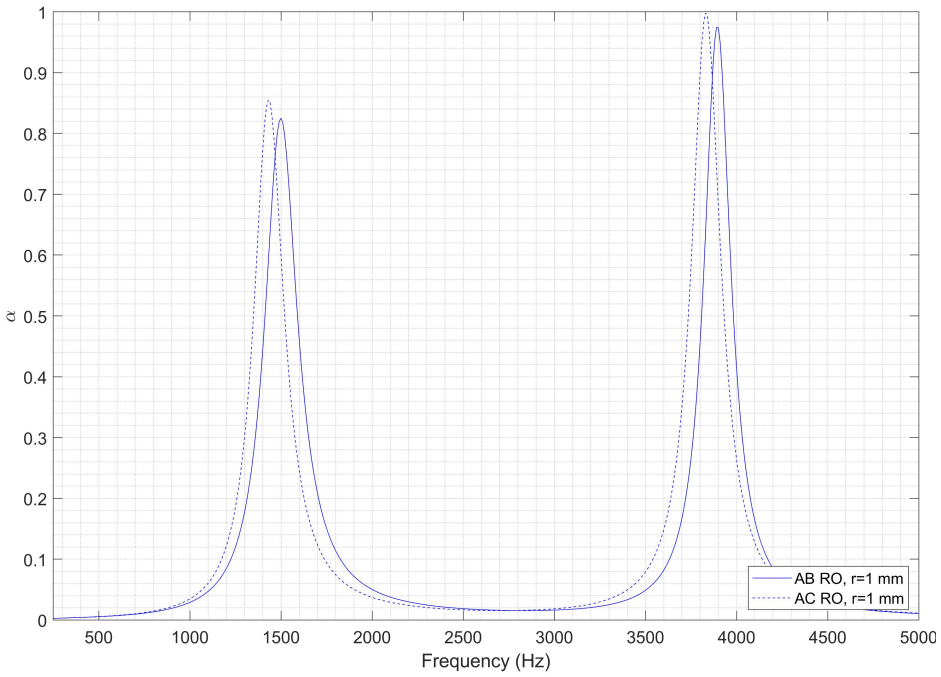

Figure 4.15: Numerically determined absorptivity for units AB and AC of $r_{pore} = 1.0mm$ with losses determined using an analytical expression.

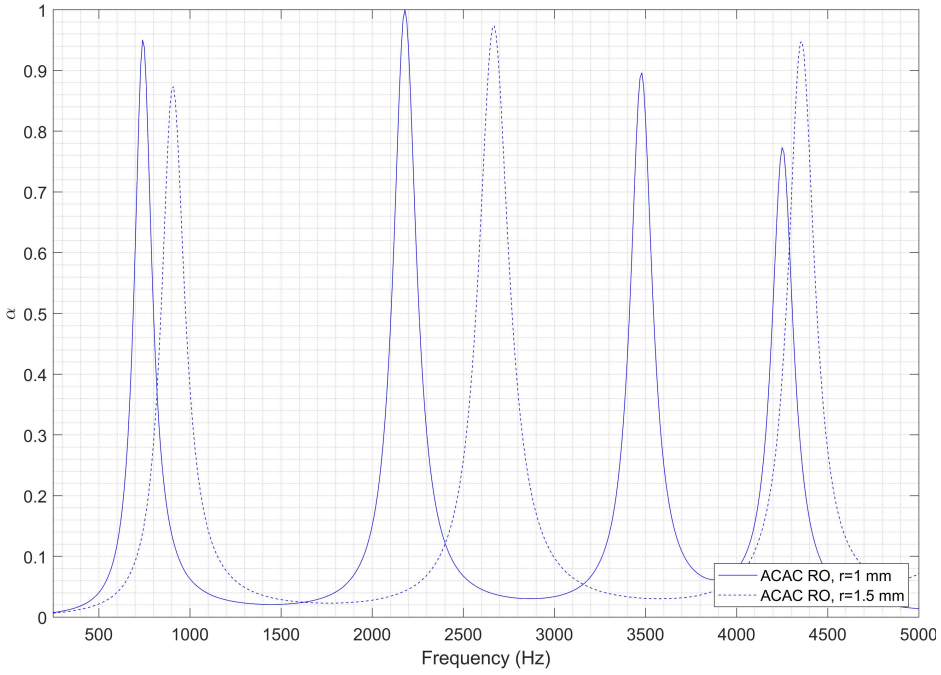

Figure 4.16: Numerically determined absorptivity for two repeated cells denoted ACAC of two different pore sizes, $r_{pore} = 1.0mm$ and $r_{pore} = 1.5mm$ with losses included analytically.

4.3.4 Design parametric study

The deviations observed between the experimental and numerical data needed further consideration. As such, it was deemed of interest to carry out multiple parametric studies so further conclusions could be drawn. It had for objective to examine the impact arising from the geometrical deviations caused by the printing technology. Carrying out such sensitivity analysis also allows to identify what parameters could be modified to obtain further absorption at lower frequencies. The unit plate AC with dimensions specified in Table 4.6 was modified to investigate the effects of four different parameters in the design, this plate was taken as a baseline as it had the desired acoustic performance. A first parametric study was carried out to observe the shift in absorptivity

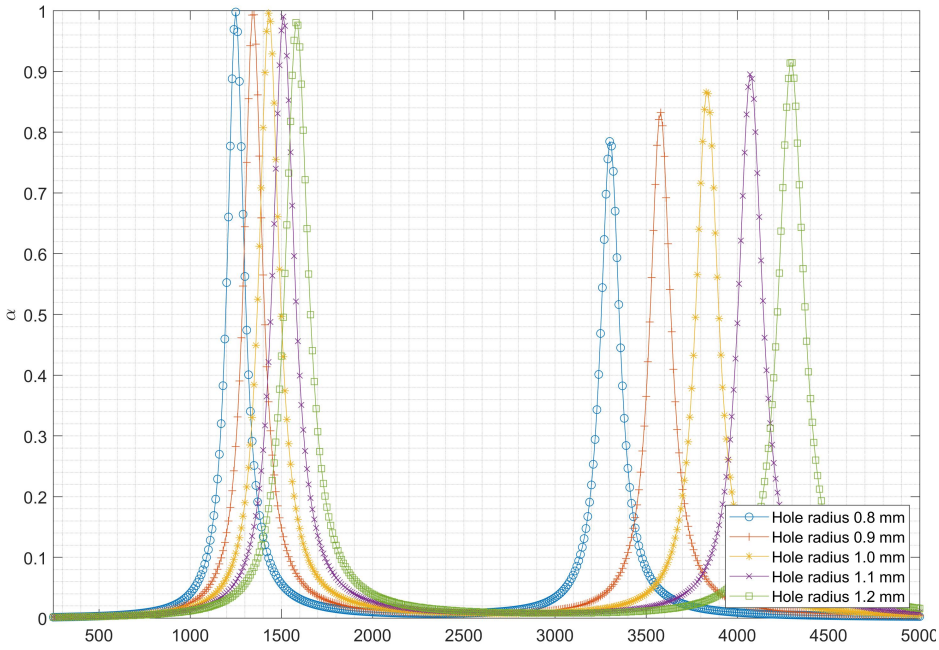

Figure 4.17: Parametric study to analyse the effect of pore radius on the absorptivity of the AC plate design, with $r_{pore} = 1.0mm$.

which could arise from changes in the hole radius. Reducing the pore radius shifts the absorptive peaks to lower frequencies. It was previously stated that a common trait of FDM technology when printing holes is to reduce the intended diameter size as the new deposited material compresses onto the previous layer. The parametric study that was realised using the hybrid analytical-numerical approach with the hole radius ranging from 0.8 mm to 1.2 mm in Figure 4.17 showed that for the smallest radius the first resonant frequency occurs at 1200 Hz and there was a shift of 100 Hz for each 0.1

mm increments. This pattern carried through for the second resonant acoustic mode. However, the frequency shift became larger, 300 Hz for each hole radius increase. The print correction factor that was used in the previous models of 0.25 mm seemed sensible from the experimental measurements in Figure 4.30 realised on this unit as the first resonant frequency occurs at 1150 Hz. For these studies as there was a need for remeshing after each parameter step, and in order to ensure stability the Padé asymptotic wave expansion solver embedded within Comsol was not used. It was observed that for some parameters the solution had not been resolved in appropriate intervals. Due to manufacturing capabilities it had been decided to keep the spacing between each plate with an airgap thickness of 2 mm.

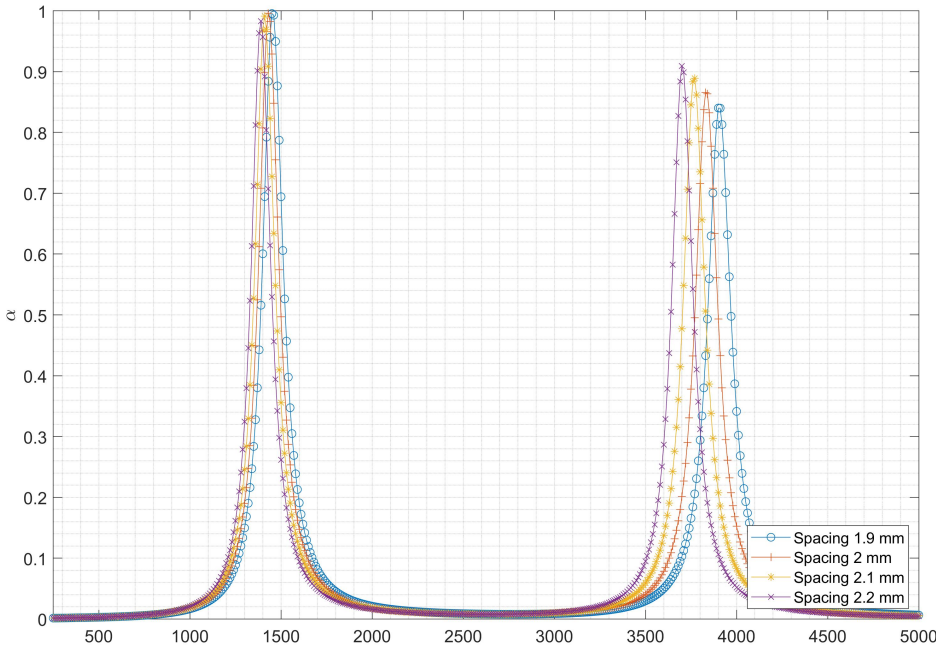

Figure 4.18: Parametric study to analyse the effect of slit size on the absorptive performance of the AC plate design, with $r_{pore} = 1.0mm$.

Absorption coefficient results obtained for the parametric study of the air spacing between the plates showed from Figure 4.18 that for the first resonant frequency there was little impact resulting from the change of spacing from 1.9 mm to 2.2 mm. The effect was more pronounced for the second resonance, however the overall impact seemed negligible as the dimensions selected for the study remained small and in accordance with the print deviation assumption that was made previously.

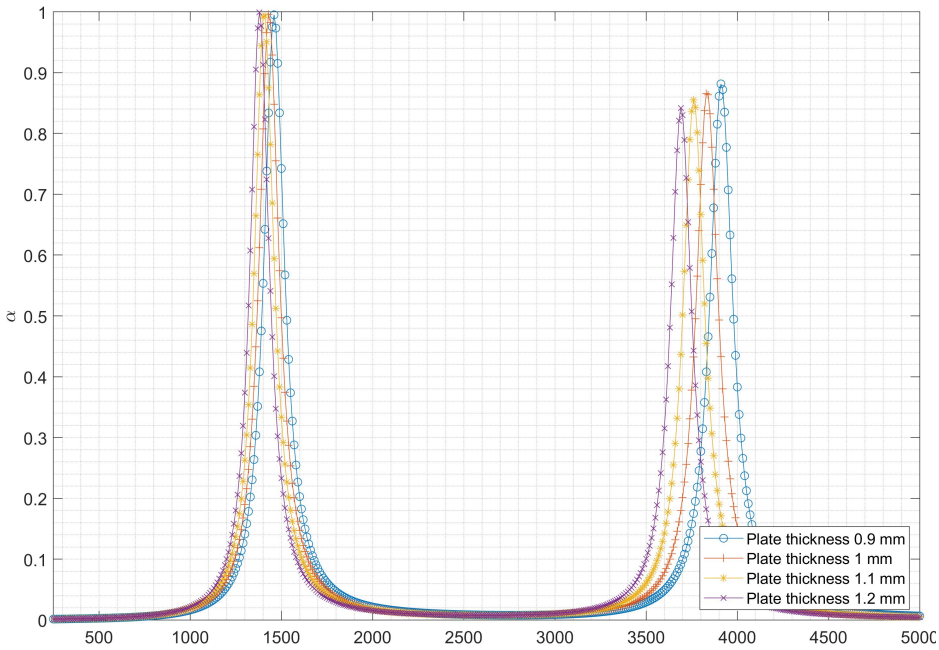

Figure 4.19: Parametric study to analyse the effect of plate thickness on the absorptive performance of the AC plate design, with $r_{pore} = 1.0mm$.

All the parametric studies realised, focused on modifying one parameter in order to isolate the parameter which was the largest contributor which modified the absorption results. The absorption coefficients obtained from the parametric studies displayed in Figures 4.18 and 4.19 were similar. To investigate the hole location difference, the location of the pores on plate A were kept at a distance 4.5 mm from centre while the following plate located after the first air gap were modified. The original 'C' position was located 17 mm from the plate's centre, that value was reduced in increments of 0.5 mm for visual clarity this was increased to 2 mm on the plot in Figure 4.20. It can be seen that the selected distance of 17 mm for the locations of pores on the second plate had the most desirable performance at the first resonant frequency. At the second resonant frequency it had the highest amplitude compared with outer pores located closer to the inner pores in the x-y plane. Therefore, the increase in tortuosity within the design acted on lowering the first resonant frequency compared with having the location of pores on both plates in phase with each other. With respect to the second acoustic resonant mode, it could be observed that when the distance of the pores on plate C were closer to the location of the pores on plate A the resonant frequency was at 3200 Hz compared with 3700 Hz for the original 17 mm from centre.

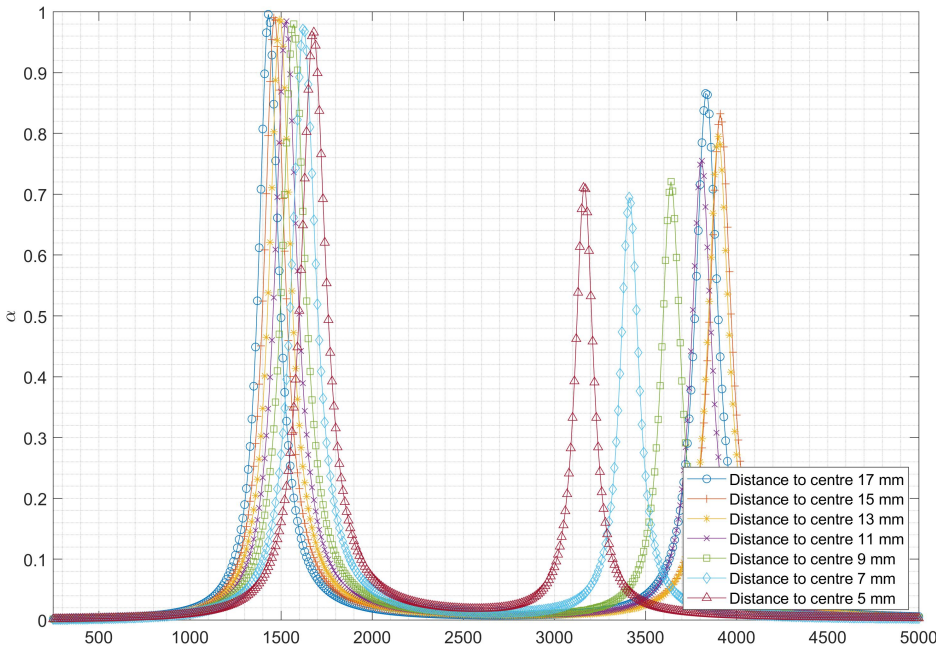

Figure 4.20: Absorptive performance of the plate design for different distance of C from centre while keeping A=4.5mm, with $r_{pore} = 1.0mm$.

The parametric studies were carried out in order to identify deviations that were seen with experimental data. They were presented solely for clarity and to emphasise what parameters were most important when designing these units in order to obtain structures exhibiting desirable low frequency absorption. The shift in resonant frequency between the hybrid analytical-numerical models and experimental were due to a combination of the four parameters studied above but not solely. Out of these parameters, the one which was the largest contributor was the pore radius which impacted on the location of the resonant frequencies.

4.4 Towards broadband absorption low-frequency liners

The acoustic performance of the AC plate with $r_{pore} = 1.0mm$ was analysed and the design which targeted low frequency absorption was satisfactory. However, as the number of units were stacked together multiple narrow resonant peaks occurred, there is a desire to obtain broadband absorption at low frequencies. From the parametric studies it was observed that the hole dimension was a strong contributor in lowering the resonant frequencies along with the increase of tortuosity within the design. Therefore,

the rationale of combining these two metrics could provide valuable results. The simple circular setup of the plate made it straightforward to divide these up into quadrants by creating partitions with differing pore sizes so they could act in parallel and thus merge resonant peaks together. The plates were divided up into four quadrants, in the first instance as per Figure 4.21 two different values of r_{pore} were chosen 1 mm and 1.5 mm and are located in different quadrants as is described in Table 4.7.

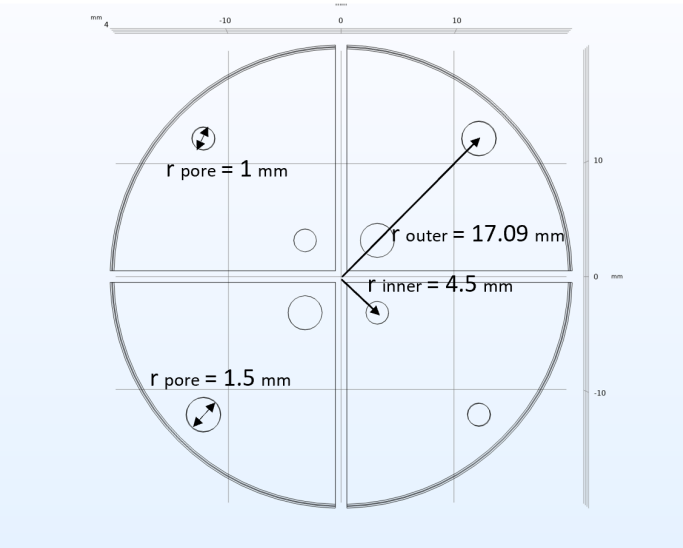

Figure 4.21: Two quadrant design with two differing pore sizes within each separate quadrant in the unit cell.

Parameter	Value	Unit
Hole radius in first and third quadrant	1	mm
Hole radius in second and fourth quadrant	1.5	mm
Partition thickness	1	mm
Position of outer pore, C	17	mm
Position of inner pore, A	4.5	mm
Plate thickness	1	mm
Spacing between plates	2	mm
Plate radius	20	mm

Table 4.7: Dimensions of the two quadrant cell depicted in Figure 4.21.

The absorption coefficient result for one unit cell of the plates displayed in Figure 4.21 are shown in Figure 4.22. The design with the two different quadrants shows that the peaks merge together at the first resonant frequency which produced a wider absorption band. The numerical results obtained through the hybrid approach over-predicted the absorptivity obtained through the viscothermal formulation.

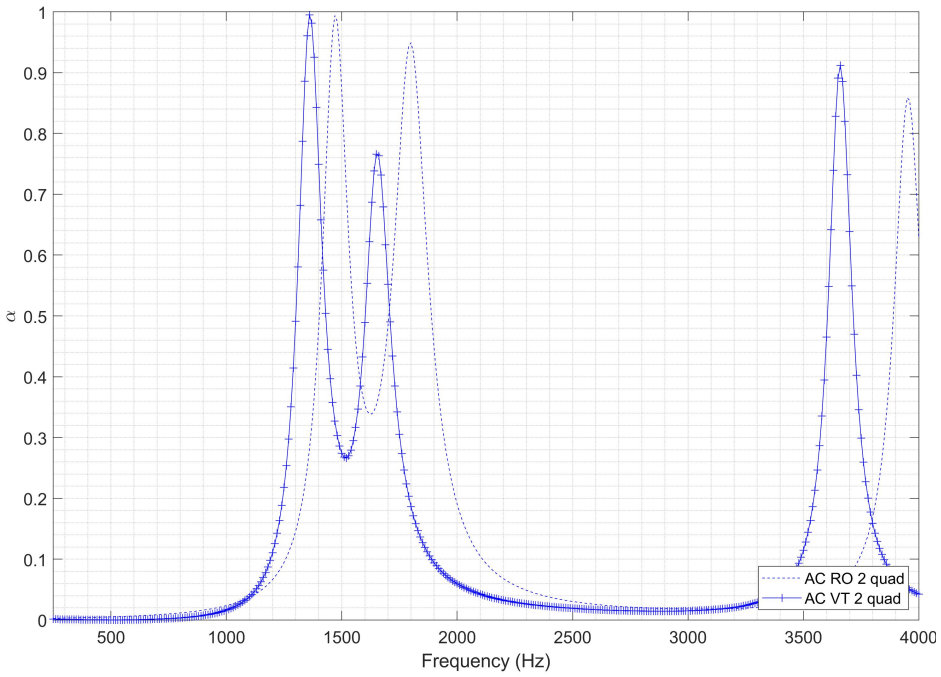

Figure 4.22: Numerically determined absorptivity for unit cell AC of dimensions specified in Table 4.7 with two quadrants using analytically determined losses versus full viscothermal simulation.

Using this design rationale which was applied in order to widen the range of absorption, it was then decided to have differing hole sizes in all four quadrants. The unit of the four quadrant design is shown on a plan view in Figure 4.23 with its geometrical dimensions specified in Table 4.8.

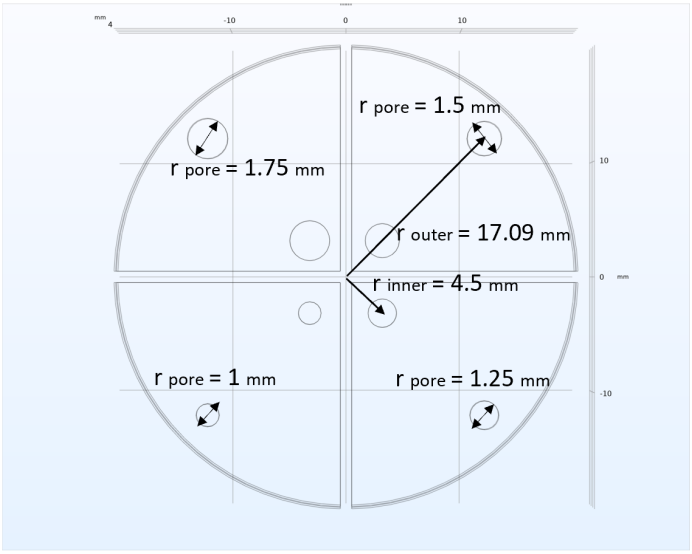

Figure 4.23: Four quadrant design with four differing pore sizes within each separate quadrant in the unit cell.

Parameter	Value	Unit
Hole radius in first quadrant	1.75	mm
Hole radius in second quadrant	1.5	mm
Hole radius in third quadrant	1.25	mm
Hole radius in fourth quadrant	1	mm
Partition thickness	1	mm
Position of outer pore, C	17	mm
Position of inner pore, A	4.5	mm
Plate thickness	1	mm
Spacing between plates	2	mm
Plate radius	20	mm

Table 4.8: Dimensions of the four quadrant cell depicted in Figure 4.23.

The results obtained for the absorption coefficient of the unit cell set-up in Figure 4.23 under normal incident plane wave using two different numerical approaches are displayed in Figure 4.24. It can be observed that there were multiple resonant peaks displayed, and the larger one located between 1000 Hz and 2500 Hz had four peaks merged together created by the parallel behaviour. The four different hole sizes operating in parallel due to the wall partitions between the quadrants contributed to this effect. As in the previous results the viscothermal model underpredicted slightly the hybrid approach. The parallel behaviour created by separating the original design into quadrants and having different sized pores in these contributed to widening the absorption band. This can be observed in Figure 4.25 which compared the best performing AC design with $r_{pore} = 1.0mm$ with the two other AC partitioned units. The four quadrant design with four different pore sizes had the widest absorption band for the first resonant frequencies compared to two quadrant design. The design which does not have any sort of parallel action between the pores had the narrowest resonant peak.

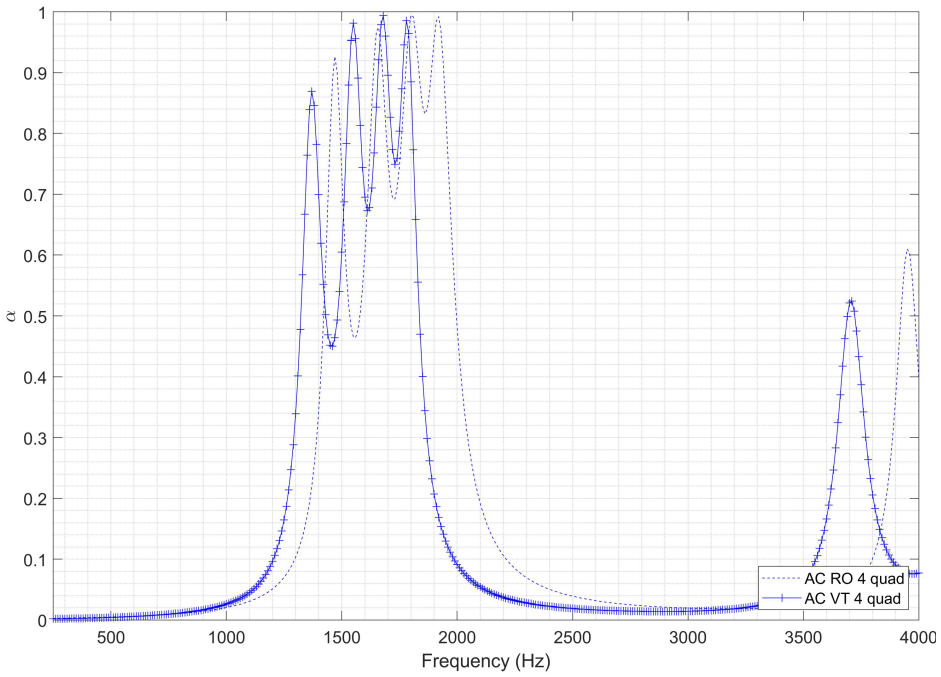

Figure 4.24: Numerically determined absorptivity for unit cell AC of dimensions specified in Table 4.8 with four quadrants using analytically determined losses versus full viscothermal simulation.

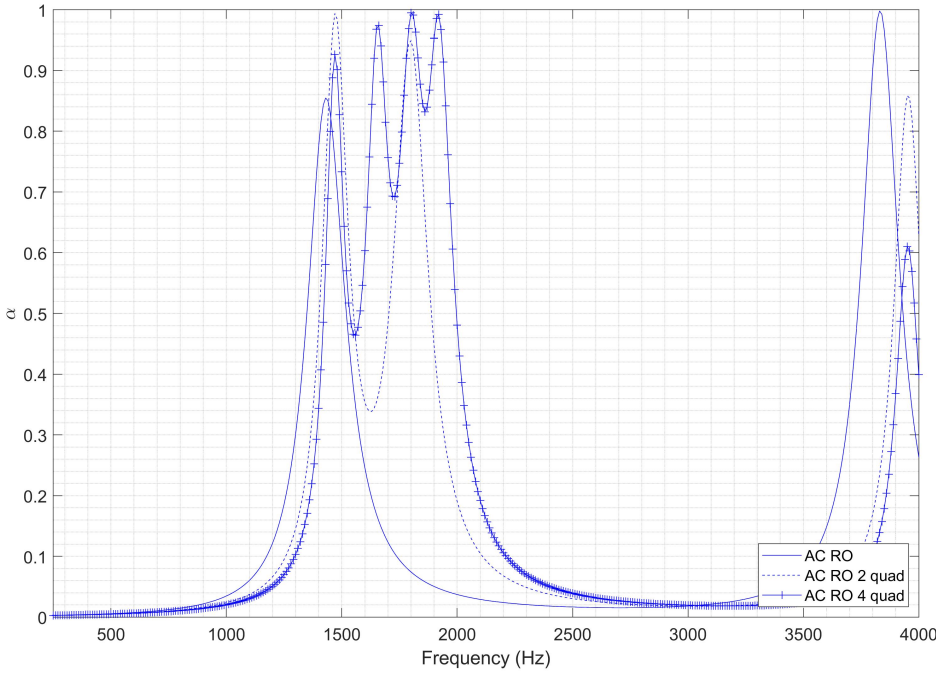

Figure 4.25: Comparison of using different hole sizes in quadrants versus AC cell in Table 4.6.

The parallel type behaviour shows promising results in widening the absorption band. However, in order to obtain designs that exhibit an absorptive spectrum which operates at a low frequency and with high amplitude across a larger band it would seem that some thorough optimisation would be required. Such reasoning can lead to a hypothetical design of which its structure is shown in Figure 4.26. The geometry presented is an exploded view of what the unit could look like and it is important to note that this structure is only 6 mm thick. There are just four different sized holes, except in this instance the design is rotated so the interaction in each quadrant produces a different behaviour. The absorption coefficient for this design was estimated on a unit and compared to double and triple stacked units to examine the benefit of a wider absorption spectrum produced by this configuration. It can be observed from Figure 4.27 that the absorption range for the one unit is much larger than the ones produced for two or three units stacked together. Although, the occurrence of the first resonant frequencies are reduced for multiple units, the peaks do get narrower. Through optimisation, these types of liner designs could be a solution to mitigate aviation noise. Preliminary results which attest of their stability in flight conditions can be seen in Appendix B. Additive manufacturing has allowed the exploration of these design concepts conveniently and in an inexpensive manner. However, there are still some issues that should be addressed to quantify the expected deviation between the produced and designed part.

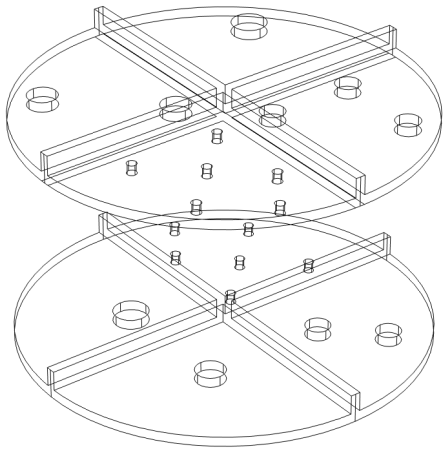

Figure 4.26: Unit cell geometry which shows the potential of parallel behaviour created with differing hole sizes, quantity and location.

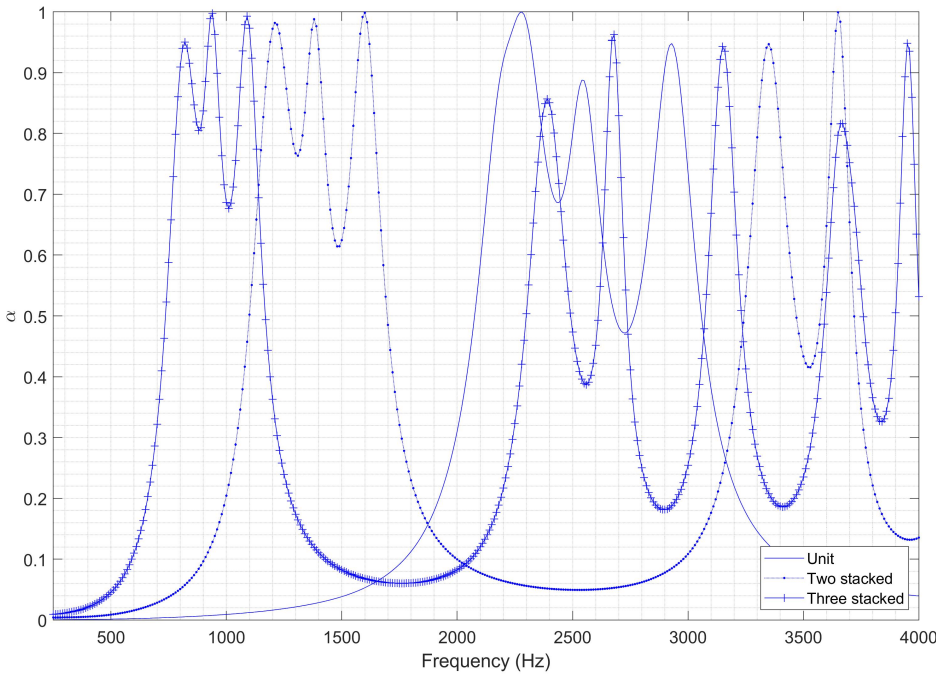

Figure 4.27: Numerically determined absorptivity for unit layer shown in Figure 4.26.

4.5 Validation from normal incident plane waves on additively manufactured PLA samples

(a) Outer face of printed PLA samples

(b) Inner face of printed PLA samples

Figure 4.28: Printed single plates that are stacked to evaluate performance *The following hole locations are determine from sample centre to pore centre and Q refers to a quadrant print with wall partitions of 1 mm thick (A01-4.5mm; B01-12.75mm; 2QA01-4.5mm; 2QB01-17mm (which should be labelled 2QC01)).*

All the sample units in this study were manufactured using PLA material printed with the FDM Prusa Mini plus printer. Images of six sample plates are displayed in

Figure 4.28 with the front face in 4.28(a) and its corresponding inner face in 4.28(b). There are no partition walls in the first sample, the addition of the partition walls in the second sample will not have much interference in the acoustic behaviour as there is just a minimal volume difference. The third sample 2QA01-2QB01 corresponds to the second quadrant which geometry is displayed in Figure 4.21. The addition of the 1 mm thick partition wall allowed to separate each quadrant in this display. There are two differing hole sizes which contributed to a parallel acoustic behaviour that resulted in merging absorption peaks together to widen the band. The following results provided aim to validate the numerical models previously presented, the AB and AC cells as well as some of the structures exhibiting parallel type behaviour. The manufacturing process and setup employed to construct and test the plates showed some uncertainty which will be addressed. The absorption coefficient results from the numerical models displayed in Figures 4.29 to 4.32, these were constructed modelling both the fluid and structural components with Comsol multiphysics. The material properties of the PLA were estimated from transmission loss measurements through a 1 mm thick piece of a material. Parametric studies varying the elastic modulus, density and Poisson's ratio were carried out to select the appropriate material properties of PLA which provided a good match with the transmission loss measurements. The acoustic loading was the same as in the previous models, described in Section 2.3.6 with a plane wave radiating with a pressure loading of $P_i = 1$ Pa and an outlet velocity of $u_o = 0$ m/s in contact with the impervious surface. The surfaces of the structure in contact with the sides of the impedance tube section should be restrained as well as the surfaces in contact with the backing aluminium block, therefore the partition walls on the outer plates. Following this, these surfaces should be fixed constraints. However, in reality this would result in an over constrained model, there is some movement and a simple support restricting motion in one direction is better suited. Damping which is dependent on the isotropic structural loss factor was added, its effect was seen to be negligible when ignored. A coupling boundary between the acoustic and structure was imposed at these interfaces. No other solid boundary conditions were applied on the interior of the unit. The experimentally obtained absorption coefficient is displayed in Figure 4.29 along with numerical results obtained from the reduced-order and viscothermal models for unit of plate AC. Both numerical results overestimated the first resonant frequency. However,

the location of the second acoustic mode was underestimated in the numerical models. The amplitude of the absorption coefficient observed experimentally was over fifty per cent lower than in the numerical results. The addition of the structure did not show any visible structural mode in the frequency range of interest.

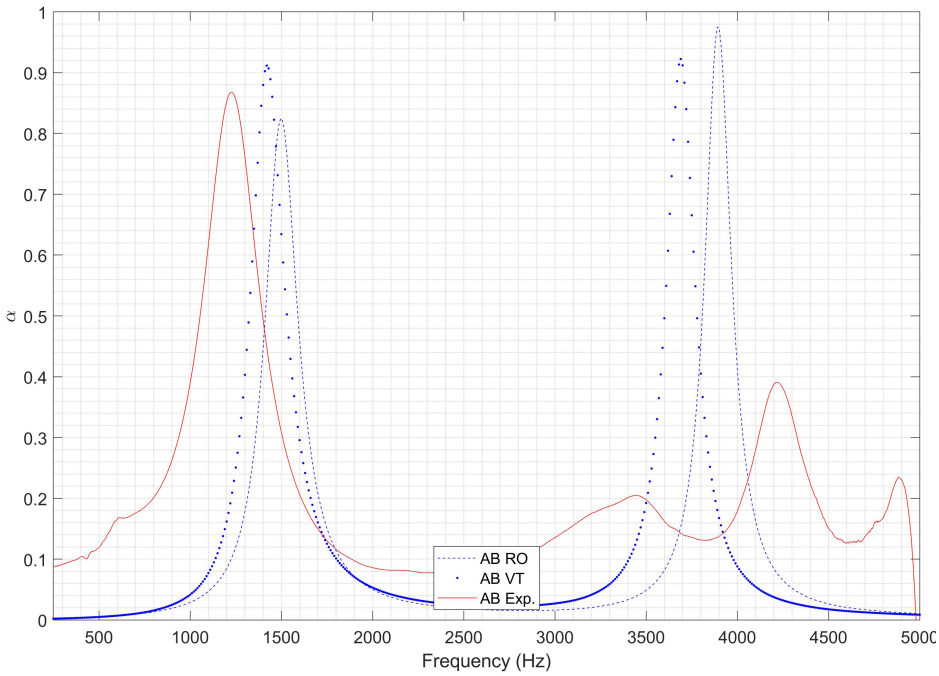

Figure 4.29: Absorptivity results from fluid-structure interaction numerical model compared with experimental measurements of a 3D printed AB cell, with $r_{pore} = 1.0mm$.

A model for the AC unit was set up in the same manner as for the previous geometry, the numerical results were compared with experimentally obtained data for the unit made from PLA. The results of these models are presented in Figure 4.30, a similar pattern could be seen with the over and under estimation of the first and second resonant acoustic modes with respect to experimental measurements. As previously, the addition of the solid mechanics modelling did not show any structural modes in the frequency range studied whereas there is a clear peak at 2500 Hz from the experimental measurements. This is certainly some structural resonant mode however, the manner in which the boundary conditions are applied to the solid structure in the model do not seem to represent what is actually occurring. The rationale for applying the boundary conditions in the structure is valid. However, in reality the unit was formed of two disconnected plates and the clamping of these at the end of the tube was provided

by four screws which were hand tightened so evenness in the applied force cannot be ensured.

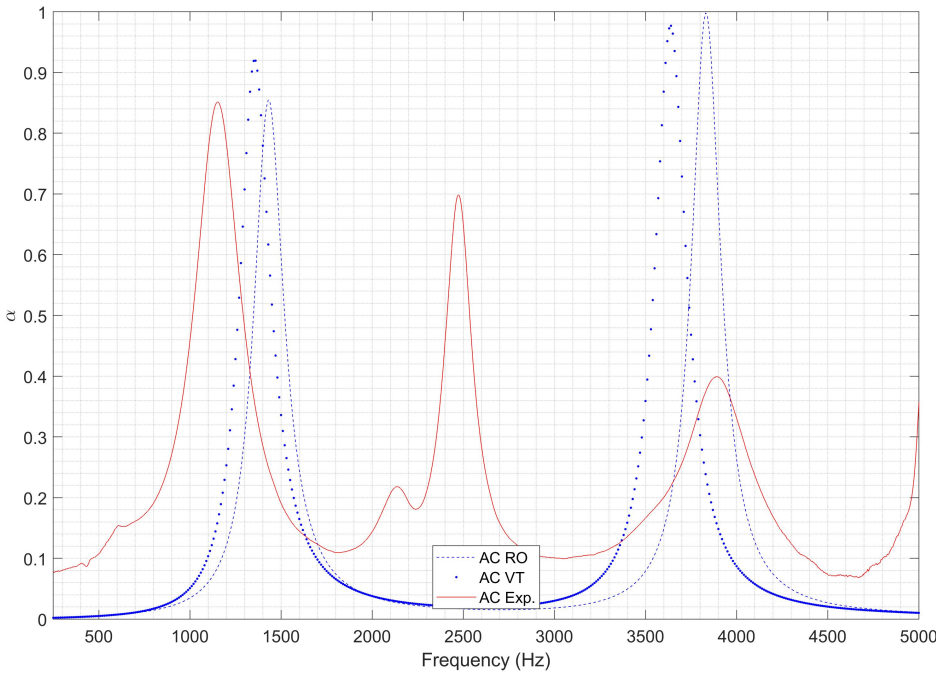

Figure 4.30: Absorptivity results from fluid-structure interaction numerical model compared with experimental measurements of a 3D printed AC cell.

The effect of two stacked units was also analysed, due to manufacturing limitations these were comprised of individual plates and they were mounted in the same manner. The experimental results can be seen in Figure 4.31 along with numerically obtained absorption coefficient for both reduced order and viscothermal models. It could be observed that the structure exhibited multiple narrow resonant peaks, as the structural modes were not detectable in the acoustic-structural model it is difficult to ascertain which modes are purely caused by vibrations within the model. It is suspected that the resonant mode located at 1800 Hz is due to some structural interaction. It can also be noted that the addition of further plates contributed to dampen the internal motion that may be occurring between the plates and as such the amplitude of that mode is lessened compared with Figure 4.30.

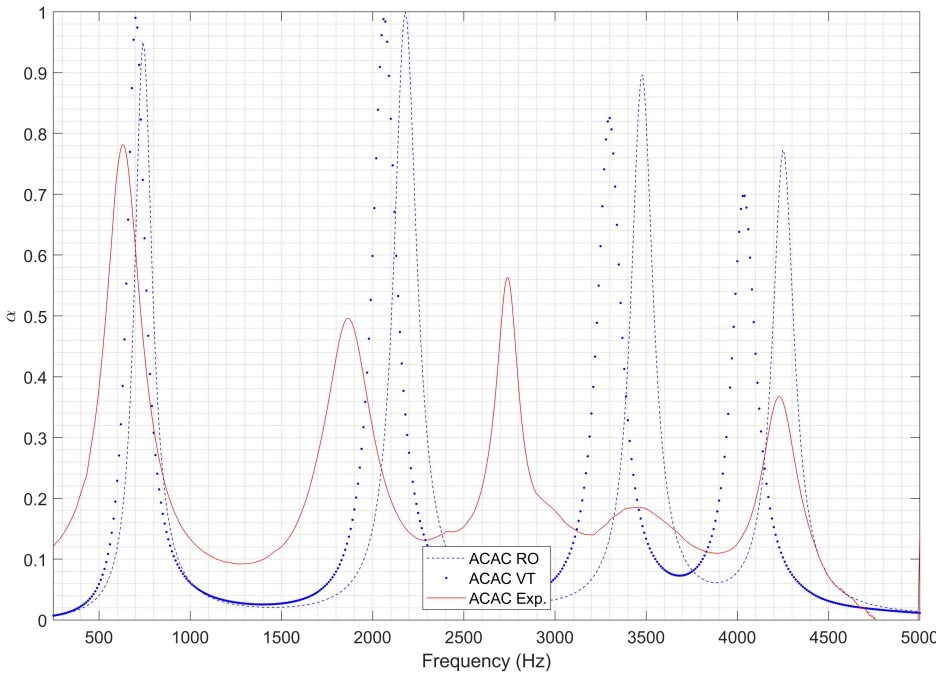

Figure 4.31: Absorptivity results from fluid-structure interaction numerical model compared with experimental measurements of two stacked 3D printed AC cells.

Experimental measurement and numerical results of two stacked units composed of differing hole sizes separated into quadrants as in Figure 4.23 previously are shown in Figure 4.32. It could be observed that there were multiple resonant peaks, utilising the different hole sizes separated into quadrants, allowed the resonant peaks produced to operate in parallel which merged them together to give a broader band result. The numerical results obtained replicate the location of the resonant peaks. However, the effect of the number of differing holes which was observed numerically is represented as a smoother curve experimentally. Through microscopy images which evaluated the pore sizes across a range of sample plates studied, there exists a strong deviation between what is intended and the actual produced part. The combination of all these deviations contribute to modifying the predicted behaviour and a certain amount of uncertainty should be taken into account when printing such structures.

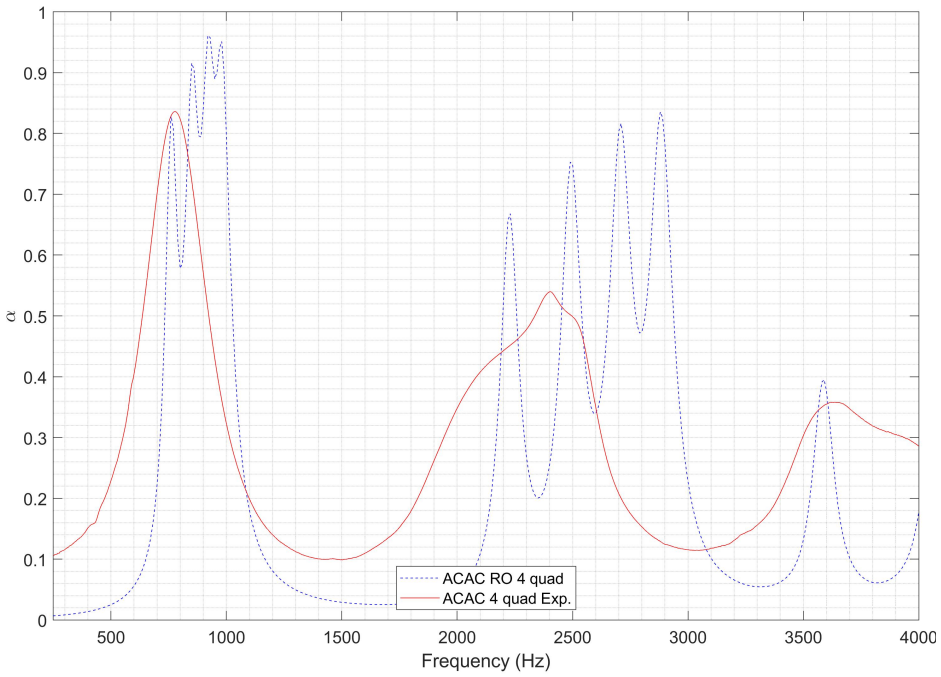

Figure 4.32: Absorptivity results from fluid-structure interaction numerical model compared with experimental measurements of two stacked 3D printed AC cells divided in four quadrants with different pore sizes in each quadrant.

The behaviour of these structures was also experimentally investigated under grazing incidence and under the presence of external flow at different Mach numbers in Appendix B. The acoustic behaviour obtained of the unit AC and AB are presented respectively as set A and Set B, in both instances the value of the holes was $r_{pore} = 1.5mm$.

4.5.1 Considerations when Validating from printed acoustic structures

Having investigated the geometrical deviations caused by FDM printing through microscopy imaging, experimental measurements were repeated on one structure, AC. As could be seen in Figure 4.28, the plates were printed individually instead of printing a unit cell that would have been composed of a first plate followed by an air gap followed by an outer plate and its subsequent air gap. The reasoning for this was due to the manufacturing constraints associated with the technology employed. Printing it as one piece could have caused entrapment of some of the PLA filament within the air gap. This could also have affected the inner pore sizes. Due to the structure, the second plate which would have followed the first air gap could have compressed that gap leading to stronger geometric deviations as well as distorting the pore shape resulting in

a more elliptical shape. The experimental measurements shown in Figure 4.33 show a combination of plates A and C which were all meant to be identical. They have been labelled A01, A02, C01, C02. The measured sound absorption coefficient was obtained from normal incident plane wave impinging on the samples. Multiple combinations of the plates were stacked together and the deviations between these can be seen clearly. The acoustic mode excited at the first resonant frequency is well captured by all the plate combinations. The divergence between the excited modes in the combinations examined occurred at around 2500 Hz which is suspected to be a structural excitation. The third mode visible in this Figure should represent the second acoustic mode in the frequency range displayed. For A01C01 and A02C01 the second acoustic peak occurs at 3400 Hz while it occurs at 3900 Hz for A02C02 and A01C02. There are certainly some geometrical deviations however, it is unlikely that they are the primary reason for such differences in their absorptive behaviour.

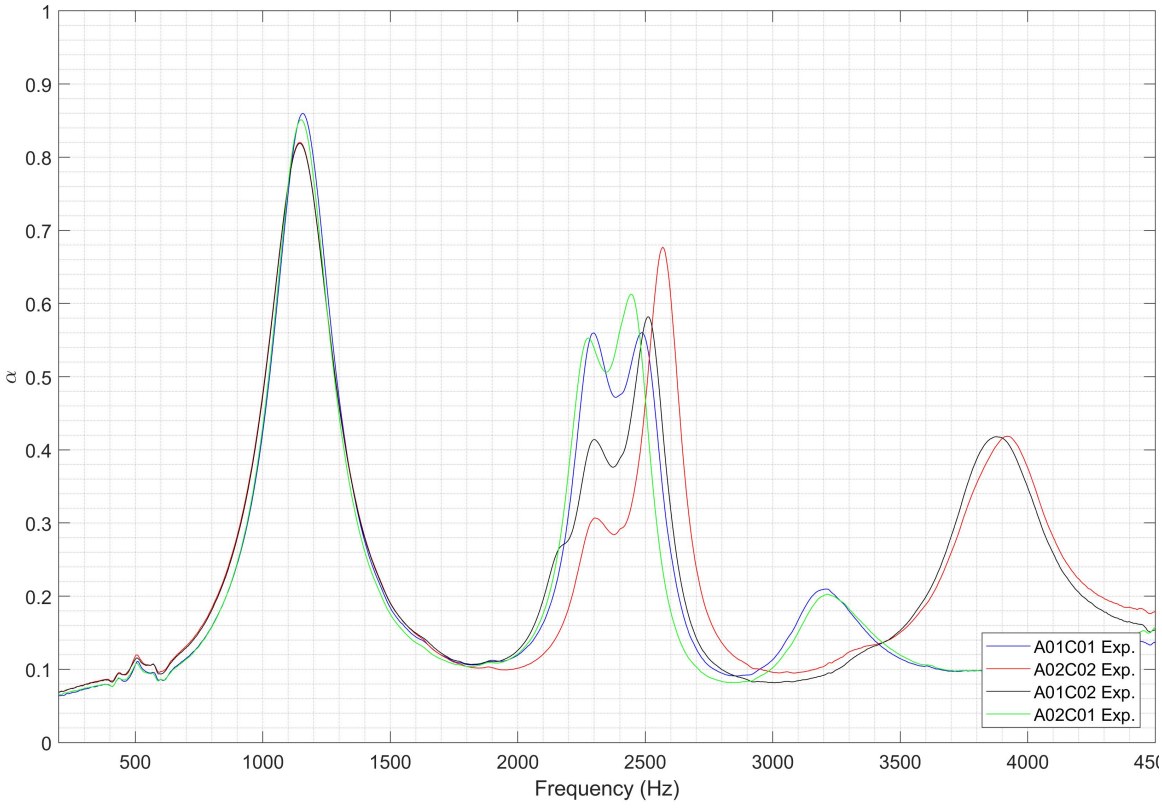

Figure 4.33: Normal incidence absorption results on PLA samples composed of plates A and C.

Numerical models were reproduced for each plate using the pore diameters obtained from microscopy images across all four holes on each plate. These were then combined

and their absorptivity was analysed, the results are shown in Figure 4.34. The acoustic-structural model as in the previous cases did not detect the structural mode which was thought to be present at around 2500 Hz. The shift produced in the narrow resonant peaks by the geometrical deviations was minimal. Therefore, it can be deduced that the differences observed experimentally lean closer to a structural nature. Due to the test setup, it was not possible to measure the vibrations experimentally that could be occurring between the plates. Although measuring that displacement would be sensible in order to include appropriate physical boundary conditions in the solid model.

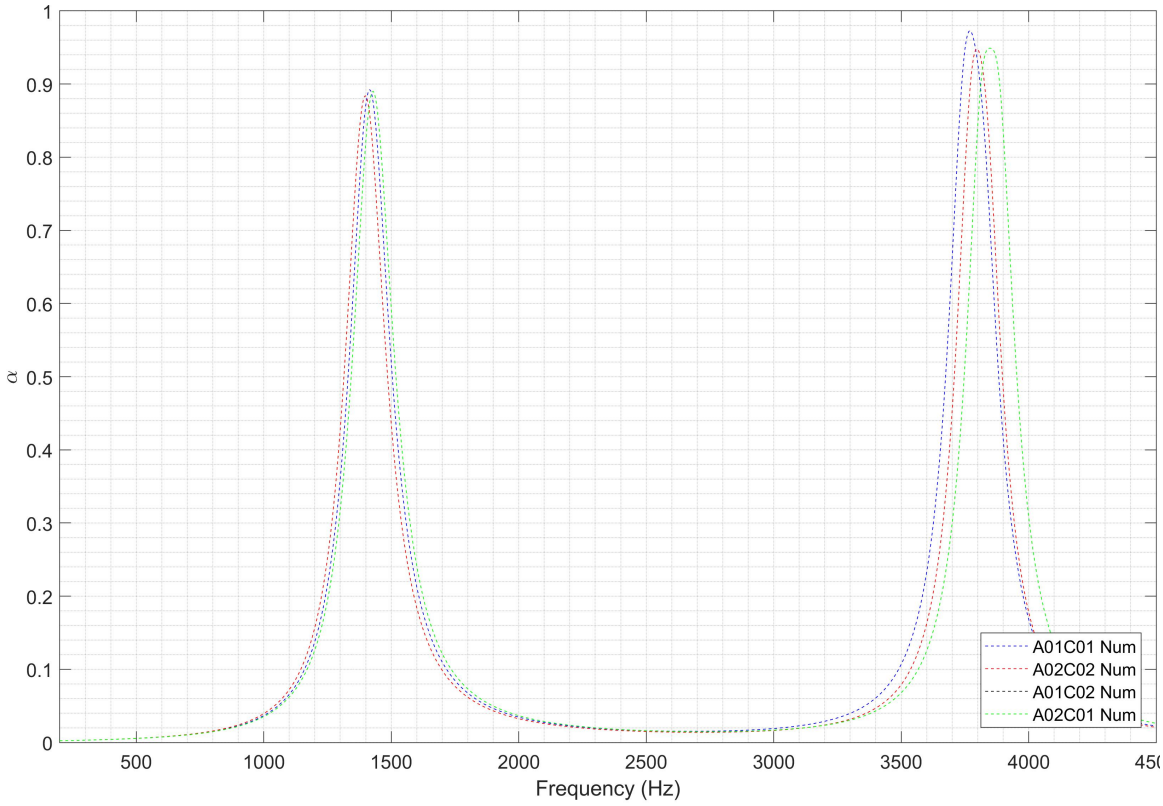

Figure 4.34: Numerical models of the corresponding samples taking into account resultant printed dimensions for the pore sizes obtained from microscopy images on different PLA samples of plates A and C.

Following this rationale, possible approaches are presented to confirm that the resonant mode which was not visible in the acoustic-structural models was not of an acoustic nature. One of the AC plate configurations tested was replicated in 3 different numerical models. The results obtained from this assessment on plate QA01QC01 are displayed in Figure 4.35. The numerical results obtained through the modelling of the acoustic solely, in blue overestimated the first resonant frequency whereas the absorp-

tivity results obtained from the acoustic-structural model were closer to the experimentally obtained results. The amplitude of the suspected second acoustic mode was a lot lower than both numerically obtained results. In order to rule out the existence of an acoustic mode at around 2500 Hz, the physicality of the problem was assessed as due to the experimental setup it would not be possible to measure the displacements which occurred between the plates. During the pressure perturbation which occurred as the wave was travelling down the tube there could be some displacement between the individual plates even though they were stacked together. The samples produced have partition walls which divided the airgap volume into separate quadrants. The partition walls connect to the subsequent plate in the test section therefore it is a strong possibility that when a phase opposition occurs the volume which is separated into quadrants becomes connected. This can explain the occurrence of this merged peak around 2500 Hz. A first hypothesis added to the acoustic-solid model was to impose a spring on the top surface of the partition wall which was connected to the following plate. However, imposing an arbitrary large value would be unreasonable considering that the displacements would be quite small. Another approach which tries to explain this phenomenon is presented in Figure 4.35 by the black dashed line. A leakage was imposed between the two connecting plates in the design analysed. The value of 0.2 mm was chosen as it corresponds to a layer height of material deposited by the FDM printer, this was subtracted from the height of the partition walls on plate A. A stress plot arising from the structural simulation of this setup at 2800 Hz can be seen in Figure 4.36(b). In the first test 4.36(a) which corresponds to the black line in Figure 4.35, the only structural boundaries were applied to the side surfaces and the top surface of the partition walls in contact with the tube's walls. In the second plate, where there was a leakage in between the plates there was a higher stress concentration, this induced leakage creates a structural resonance at 2800 Hz. Even though, the problem could not easily be quantified and there were numerous factors which would be needed to accurately model the physical problem. The goal was to rule out the existence of an acoustic mode at 2500 Hz.

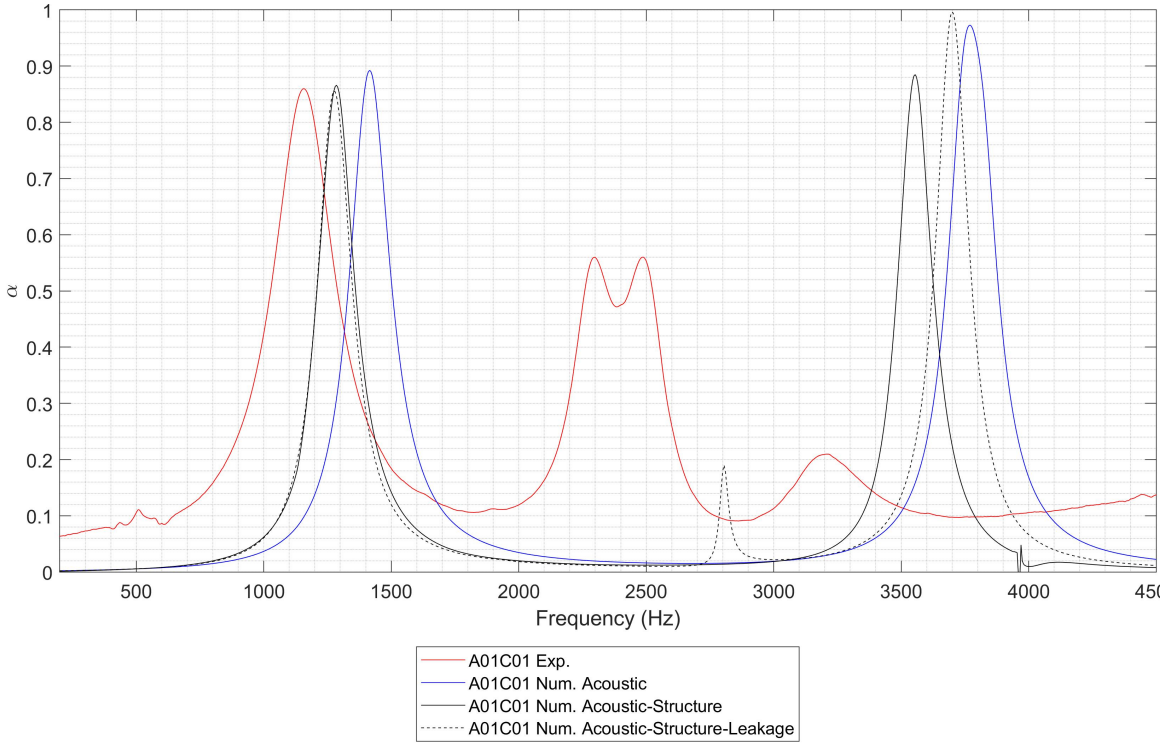

Figure 4.35: Experimental normal incidence results from unit QA01-QC01 compared with an acoustic and fluid-structure interaction models to detect structural mode.

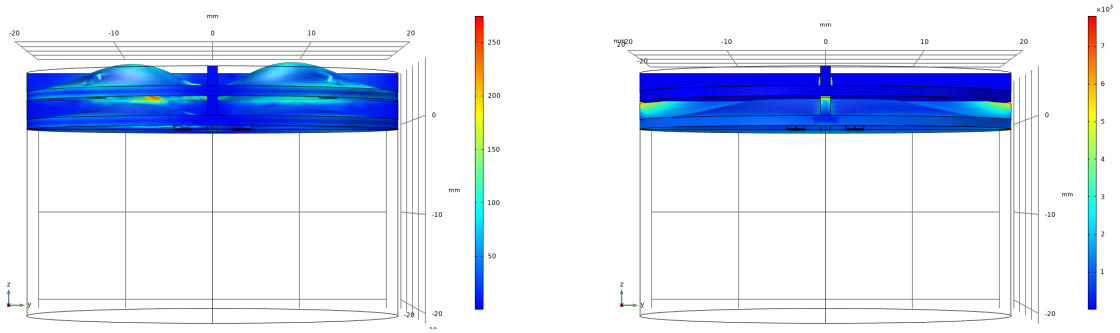

(a) Fixed plates (b) Gap in connecting plate

Figure 4.36: Stress plot at 2800 Hz for idealised stacked plates versus possible leakage corresponding to a layer height between the plates.

4.5.2 Free vibration models of individual plates and a combined unit

The acoustic-structural models did not capture all the possible vibrations occurring in the model and the plate motion could not have been directly measured in the current experimental setup. However, a simple eigenfrequency analysis on separate plates

which composed the unit and a combined set gave satisfactory results at the resonant frequencies of interest in Figure 4.35. Plates A and C have been analysed in a free vibration set up with the PLA material parameters that were determined previously. Plots showing the stress at the first and second resonant modes for plates A and C are shown in Figures 4.37 and 4.38. From the results obtained for both individual plates the resonant modes are very similar, so the location of the pores has minimal impact on the structural resonance in this system. The free vibration study on the combined

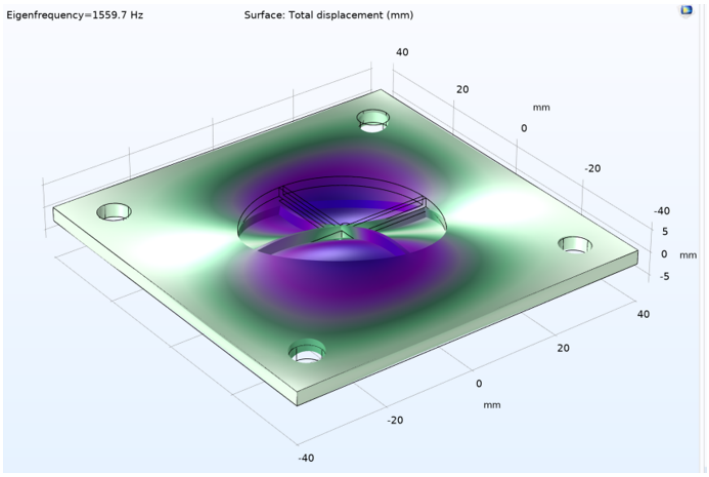

(a) Plate A 1st mode at 1560 Hz

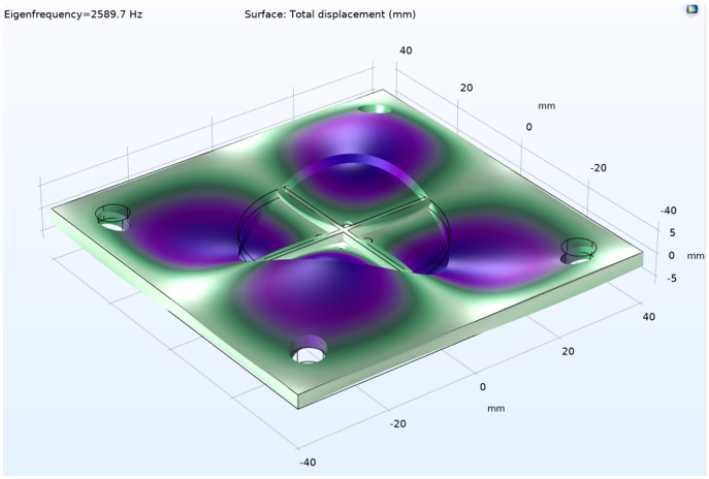

(b) Plate A 2nd mode at 2590 Hz

Figure 4.37: Structural resonant modes for plate A.

plates above which represented a unit AC had a first structural resonant mode at a frequency at 3449 Hz which was a little higher than the one observed in Figure 4.35. However, the model was represented as one stacked unit and in reality the plates do not have a homogeneous surface and they were not fixed together. If there were no issues with the printing process and entrapment it would be desirable to manufacture

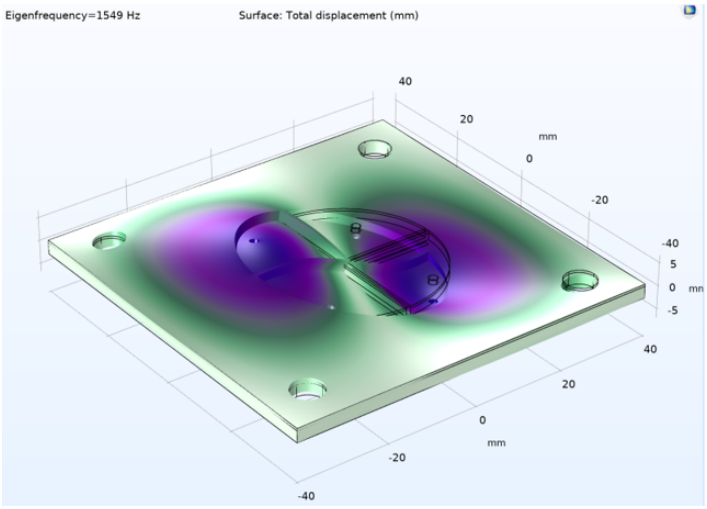

(a) Plate C 1st mode at 1550 Hz

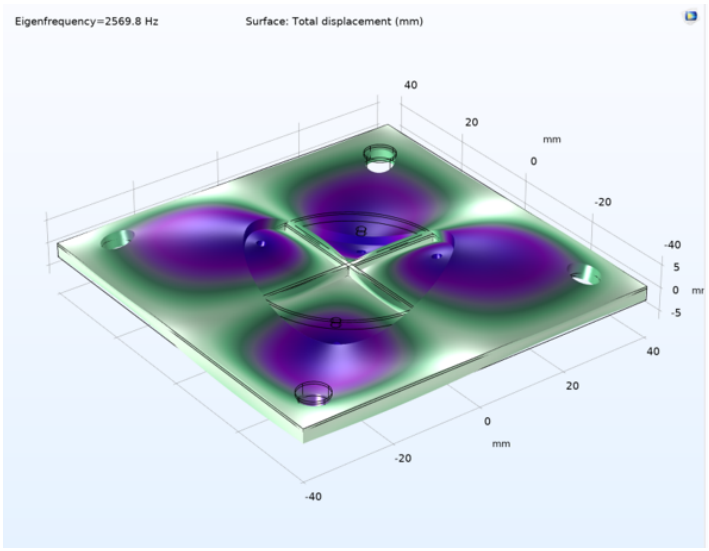

(b) Plate C 2nd mode at 2570 Hz

Figure 4.38: Structural resonant modes for plate C.

this as a single unit to disregard this structural resonance with the frequency range studied.

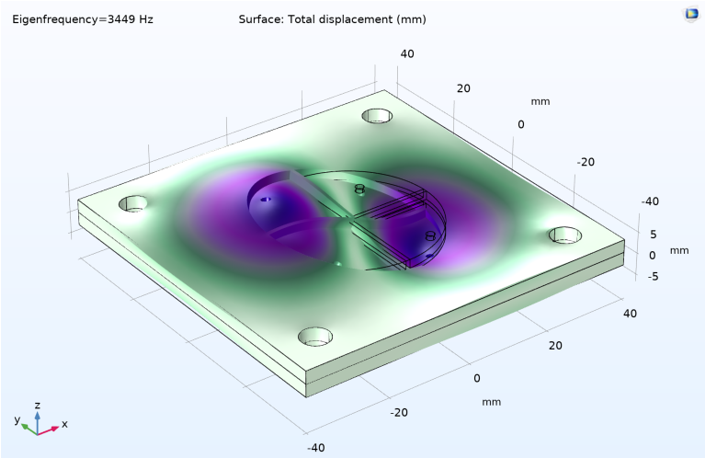

Figure 4.39: Structural resonant mode for combined AC plates.

4.6 Conclusions

Multiple multilayered plate configurations were analysed as part of this study. Some exhibited low frequency high absorption resonant peaks and others through a parallel behaviour possessed wider absorption bands. These configurations are promising for low frequency noise absorption and some of the configurations explored were investigated under the presence of grazing flow which showed good performance. The use of machine learning to provide a robust optimisation of these parallel behaviour absorptive plate configurations could be pioneering in the advancement of liner design for turbofan engines. As part of this study, certain factors were identified during the experimental validation from printed PLA components. Indeed the normal incident tests to evaluate their behaviour does not ensure a controlled tightening of the samples and there were inner plate vibrations. Therefore, a different manufacturing strategy could be used or experimental vibration measurements could be included in an acoustic-structural numerical model. The vibrational effects observed are not negligible. Indeed they may interact and modify the Helmholtz resonators when the cavity is fixed compared to when it is in motion. This structural modification of the resonator cavity can vary the resonant frequency and the absorption produced. The vibro-acoustic coupling produces additional resonances which could also be exploited. The structural and acoustic-structural analyses provided a valid explanation for what may be occurring and why the structural mode is not represented in the frequency range studied.

Chapter 5

Discussion

An efficient modelling strategy was developed which enabled the design of low-frequency broadband noise absorptive structures which have a valid application for noise reduction in a turbofan engine environment.

Additive manufacturing allows to develop a multitude of different noise reducing treatments such as metamaterials, metasurfaces and porous materials. Considering a noise treatment for an engine duct with predominant fan noise it would be desirable to obtain a material with low frequency absorptive behaviour. Through design there is a motivation to extend this to broadband perfect absorption within the industry [120]. Observations of the results obtained as part of this thesis which analysed the absorptive behaviour of samples manufactured using different printing technologies, it is reasonable to say that there are deviations dependent on the technology employed. A Round Robin study was carried out to evaluate the acoustic properties of a benchmark porous material manufactured using different technologies in multiple laboratories part of the DENORMS COST action. It confirmed that there are deviations in the acoustical behaviour due to the nature of the manufacturing process employed. There were also differences in the acoustic behaviour obtained between laboratories using the same technology [74].
For a commercial scale application the use of such materials seems expensive, time consuming to produce, and can lack reliability with respect to the predicted performance. The numerical results obtained on a benchmark acoustic metamaterial which included the associated viscothermal losses in the system provides a good match with the experimental data obtained nonetheless. There can be significant differences between the resultant absorption obtained numerically and experimentally from 3D printed samples. The defects which are inherent to the printing technology increase the losses within the system. However, the deviations observed from an ideal unit cell representation in the numerical approach show deviations consistent with manufacturing imperfections. Availing of the opportunity to utilise four different additive manufacturing technologies which ranged from low cost to premium state of the art machines for the designed configurations in this project has been a significant tool. This gave an overview of the rapid prototyping technologies available to manufacture metamaterials and assess the suitability of one technique over another in terms of acoustic

performance obtained. The samples printed with SLA and SLM provided the closest match with predicted numerical models in terms of the resonant acoustic modes and their location. Therefore, SLA printing technology is a good compromise to manufacture such structures. It is relatively low cost and less specialist training is needed to operate the printer in comparison with SLM. There are still some inherent problems with this technology as large amounts of resin can become entrapped which creates blockages in channels. This will undoubtedly affect the absorptive properties of the structure. There are reservations with these printing technologies on the economies of scale and the capability of producing these structures on large build platforms. Overall, these printing technologies have inherent effects linked to their process on the resultant printed structure. Some produce lower quality parts, others show a higher fidelity to the designed structure but have large surface roughness. Even though there are some issues with the manufacturing, this technology has allowed the printing of absorptive materials at microscopic scales and the addition of modified built-up structures from the fundamental unit cell. The dedicated area reserved for noise treatments inside ducts remains quite tight. The development of space-coiling mechanisms allowed to double the length of resonators within a certain depth. The lowering of the first resonant peak of absorption was successful through a sensitivity analysis of parameters within the resonant chambers in the labyrinthine system. This sort of configuration would be unmanufacturable without 3D printing, so it still possesses a lot of merit. The quantification of additional losses depending on the printing technology employed was carried out in a simple proof of concept approach through the viscosity and hydraulic radius. In an efficient design loop, it might be a wasted effort to quantify these effects as the variability with some technologies is small which was confirmed from the amplitude of the absorptivity observed between predicted values and measurements.
Studies which have dealt with the acoustic characterisation of 3D printed absorptive materials agree with the fact that the manufacturing defects alter the predicted behaviour. Between direct numerical predictions and measurements obtained from 3D printed samples there is an increase of ≈ 0.15 in the amplitude of absorption [121] as the imperfections increase the intrinsic losses in the system. Other studies have focused on using reverse engineering methods to experimentally determine acoustic parameters from printed samples. Equivalent fluid methods are then used to evaluate the Johnson

Champoux Allard Lafarge (JCAL) parameters via FEM on an ideal representative elementary volume of the porous materials [120]. After numerically obtaining the different transport parameters, the acoustic deviations caused by the geometric defects are experimentally characterised through experimental acoustic measurements from which the transport parameters comprising defects can be retrieved. The corrected predictive models were simulated using the transfer matrix approach and validated against macroscale measurements [122]. These studies are of valued scientific interest as they aim to incorporate defects resultant from the manufacturing processes into the modelling approach. However, from the design development point of view for an industrial application it seems impractical. Indeed prior knowledge of the sample is required to correct the acoustic behaviour. Interesting reflections which attempts to create a dialogue between the local scale numerical model, imaging techniques and measurements have been made by [123]. In reality there are always adjustments to take into account when comparing measurements with macroscopic parameters obtained from the local geometry. The usage of imaging techniques such as scanning electron microscope and x-ray imaging can inform some important microstructural defects which have a significant impact on the acoustic properties. From this new information, adjustments can be made to the model of the representative unit and then macroscale acoustic properties can be evaluated again. These studies add a lot of scientific value and merit to this field. However from a design point of view in an industrial application, they are rather impractical as there is too much back and forth in the modelling procedure which is inefficient in a delimited time frame. The numerical results produced from these equivalent fluid models do not give direct predictive acoustic behaviour. Furthermore, the estimation of viscothermal losses using this equivalent fluid approach is too much of an approximation. Being capable of including some of the resultant defects arising from additive manufacturing technologies into numerical models remains a challenge as some of the variability can be difficult to quantify.
In terms of using acoustic metamaterials for large scale industrial applications it is important to note inherent defects even though they might have a positive impact on the produced acoustical behaviour, direct numerical approaches provide a good estimation.

The use of additive technology for noise reducing acoustic metamaterials could be

more suited to other small scale industrial applications. In the case of turbofan engines, development of novel liner concepts can be envisaged using more traditional manufacturing techniques which exhibit advantageous low broadband frequency absorption. Within the industry there is continued work in the development of novel liner concepts using variable depth chambers with an embedded parallel element [124]. The absorptive performance of a multilayered plate configuration manufactured from perforated aluminium sheets separated by stainless steel spacers where the dissipation was provided mainly in the gaps proved to be particularly effective for low frequency absorption. The metaliner designed where the air travels through a staggered pathway instead of a direct passage with aligned pores effectively used controlled tortuosity to lower the acoustic resonances. In addition, the coupling of the transfer matrix method with a full viscothermal description of the unit cell through FEM provides a fast and efficient tool to predict the acoustic characteristics of a larger repeated cellular structure. This is possible due to the fundamental periodic nature of metamaterials. Thus the design provided a good balance using a tortuosity controlled absorptivity. This motivated a search to obtain a design which had a broader band of absorption while remaining at a low frequency of operation.

Critical geometric parameters were identified in the design which successfully reduced the frequency of occurrence of the resonant peaks. In a second stage other geometric parameters were introduced which achieved a broader high absorption band. The acoustic behaviour of basic designs were validated with experimental measurements obtained from printed PLA samples. The deviation between experimental, viscothermal and reduced order results was analysed. As the level of deviation observed was similar for all three, the reduced order approach is a valid approximation. With this modelling efficiency it allows to explore and evaluate more elaborate multilayered plate configurations. An emphasis was placed on achieving a parallel type behaviour between separated chambers inside the gaps. Having pores of different sizes behaving in parallel with other sized pores in separate quadrants successfully contributed to broaden the absorption band. An incremental design process was used, where 2 quadrants had the same geometric properties followed by 4 quadrants where each of these 4 had different geometric parameters within. During the validation process, deviations were

observed due to internal plate resonances. This design process allowed the exploration of more complicated patterns for which a proper design optimisation approach would be required. The introduction of artificial intelligence and machine learning in the development of novel liner concepts is a promising design avenue. This will greatly reduce the development time associated with their design [125]. This design development along with the efficient modelling tools to approximate viscothermal dissipation within the gaps of these multilayered configurations paves the way for optimum noise reducing treatments for turbofan engines.

Chapter 6

Conclusions

6.1 General

In a context of guaranteeing the continued development of sustainable air travel efforts to deliver effective noise reducing treatments for engine ducts is of critical importance. The studies examined within this thesis provide novel contributions to evaluate the usage of printed acoustic metamaterials as noise reducing treatments. However it also demonstrates their limitations at an industrial development stage and reaching a high technology readiness level. Another avenue which seems more promising in achieving further significant noise reduction for turbofan engines is through novel liner concepts.

The aim of this thesis was to deliver a rapid developmental design process aided by efficient modelling tools to obtain sub-wavelength absorptive structures. And to evaluate the influence of additive manufacturing in the design of acoustic metamaterials. The following objectives were achieved:

- The predicted acoustic performance of acoustic materials through different additive printing technologies was experimentally validated. Traditional construction layups on balance seem to be easier to model and implement although additive manufacturing could potentially introduce more disruptive dissipation mechanisms.

- Viable macro models were obtained through a full description of a fundamental unit cell.

- An efficient reduced-order modelling strategy was put forward, comparable to a full viscothermal description to estimate losses within air gaps in multilayered perforated panels which was shown to be a robust design tool.

- Sensitivity analysis of critical parameters to design a multilayered panel structure to obtain low-frequency broadband absorption.

6.2 Future Work

Considering some of the experimental results obtained in this thesis with the printed multilayered plate configurations, further investigation of the structural responses could be investigated. This could be done either by quantifying the structural resonances

within the models by prior experimental investigation with a vibrometer or using a different manufacturing procedure. Indeed the plates were printed individually, printing one cell composed of two plates with fixed partition walls might alter the resonances observed. However, the added resonance provided by the vibro-acoustic coupling could be further exploited to provide additional sound absorption. In order to analyse the performance of these noise reducing treatments, it is necessary to evaluate them in environmental conditions which resemble the environment where they will be used. Attempt of a continuation study of the topics explored in this thesis which in the author's view is critical to evaluate their suitability in a turbofan engine environment is given in Appendix B.4. The preliminary experimental work analyses some absorptive structures under external flow conditions. The results obtained attest the stability of these structures at low Mach numbers. As temperatures in the proximity of the engine can reach approximately $850°C$, analysing noise reducing treatments under hot flow would extend the knowledge on the usage of such materials and provide information on certain necessary adaptation required so their performance is not altered.

Bibliography

[1] M. Basner, C. Clark, A. Hansell, J. I. Hileman, S. Janssen, K. Shepherd, and V. Sparrow. Aviation noise impacts: State of the science. *Noise Health*, 19(87): 41–50, 2017. ISSN 1463-1741 (Print) 1463-1741. doi: 10.4103/nah.NAH_104_16.

[2] Agency, European Aviation Safety and Agency, European Environment. European Aviation Environmental Report 2016. Technical report, European Commission, 2016. URL {https://ec.europa.eu/transport/sites/transport/files/european-aviation-environmental-report-2016-72dpi.pdf},publisher={PublicationsOffice}.

[3] European Parliament. Air and noise pollution | Fact Sheets on the European Union | European Parliament, 2019. URL http://www.europarl.europa.eu/factsheets/en/sheet/75/air-and-noise-pollution.

[4] Wiktoria Wojciechowska, Andrzej Januszewicz, Tomasz Drozdz, Marta Rojek, Justyna Baczalska, Michal Terlecki, Karol Kurasz, Agnieszka Olszanecka, Mikolaj Smolski, Aleksander Prejbisz, Piotr Dobrowolski, Tomasz Hryniewiecki, Reinhold Kreutz, and Marek Rajzer. IMPACT OF REDUCTION IN AIRCRAFT NOISE EXPOSURE ON BLOOD PRESSURE AND ARTERIAL STIFFNESS DURING COVID-19 PANDEMIC: CROSS-SECTIONAL AND LONGITUDINAL STUDY. *Journal of Hypertension*, 39, 2021. ISSN 0263-6352. URL https://journals.lww.com/jhypertension/Fulltext/2021/04001/IMPACT_OF_REDUCTION_IN_AIRCRAFT_NOISE_EXPOSURE_ON.597.aspx.

[5] Thomas Münzel, Tommaso Gori, Wolfgang Babisch, and Mathias Basner. Cardiovascular effects of environmental noise exposure. *European heart journal*, 35 (13):829–836, April 2014. ISSN 1522-9645. doi: 10.1093/eurheartj/ehu030. URL https://www.ncbi.nlm.nih.gov/pubmed/24616334.

[6] World Health Organization. Burden of disease from environmental noise Quantification of healthy life years lost in Europe. Technical report, WHO Regional Office for Europe, 2011. URL http://www.who.int/quantifying_ehimpacts/publications/en/.

[7] Anne-Sophie Evrard, Marie Lefèvre, Patricia Champelovier, Jacques Lambert, and Bernard Laumon. Does aircraft noise exposure increase the risk of hypertension in the population living near airports in france? *Occupational and Environmental Medicine*, 74(2):123–129, 2017. ISSN 1351-0711. doi: 10.1136/oemed-2016-103648. URL https://oem.bmj.com/content/74/2/123.

[8] L Leylekian, M Lebrun, and P Lempereur. An overview of aircraft noise reduction technologies. *Aerospace Lab Journal*, 2014.

[9] AIRBUS. Getting to grips with aircraft noise, December 2003. URL https://www.slideshare.net/FernandoNobre1/aircraft-noise-27755949.

[10] P S Tide and K Srinivasan. Novel chevron nozzle concepts for jet noise reduction. *Proceedings of the Institution of Mechanical Engineers, Part G: Journal of Aerospace Engineering*, 223(1):51–67, 2009. doi: 10.1243/09544100JAERO347. URL https://doi.org/10.1243/09544100JAERO347.

[11] Maxime Huet, François Vuillot, Nicolas Bertier, Marek Mazur, Nancy Kings, Wenjie Tao, Philippe Scouflaire, Franck Richecoeur, Sebastien Ducruix, Corentin Lapeyre, et al. Recent improvements in combustion noise investigation: from the combustion chamber to nozzle flow. *AerospaceLab*, (11):10, 2016.

[12] Uno Ingard. On the theory and design of acoustic resonators. *The Journal of the Acoustical Society of America*, 25(6):1037–1061, 1953. doi: 10.1121/1.1907235. URL https://doi.org/10.1121/1.1907235.

[13] SAFRAN Aircelle. GdR META kick-off Metamaterials for aeronautics, January 2016. URL http://events.femto-st.fr/sites/femto-st.fr.GdR-META/files/content/Documents/Reunion_Lancement/2016-01%20KO%20GdR%20META%20-%20Aircelle%20presentation.pdf.

[14] Jacky Mardjono, Riou Georges, Boiteux Jean-Michel, and Frederic Boubila. The epsl static tests demonstration of liners noise reduction concepts. In *19th AIAA/CEAS Aeroacoustics Conference*, page 2174, 2013.

[15] DLR Berlin Enghardt, Lars. Proband: Improvement of fan broadband noise prediction: Experimental investigation and computational modelling. In *CEAS BBN Workshop 2008, Bilbao*, 2008.

[16] RE Motsinger and RE Kraft. Design and performance of duct acoustic treatment. *NASA Tehcnial Reports*, 1991.

[17] T Zandbergen. Do locally reacting acoustic liners always behave as they should? *AIAA Journal*, 18(4):396–397, 1980.

[18] Umut Zalluhoglu and Nejat Olgaç. Placement of helmholtz resonators in series for passive control of thermoacoustic instabilities from a time-delay perspective. *2016 American Control Conference (ACC)*, pages 1845–1850, 2016.

[19] Gerald W Bielak, John W Premo, and Alan S Hersh. Advanced turbofan duct liner concepts. *NASA Technical Reports*, February 1999.

[20] Andrew Kempton. Acoustic liners for modern aero-engines. In *15th CEAS-ASC Workshop and 1st Scientific Workshop of X-Noise EV*, 2011.

[21] M. A. Biot. Theory of propagation of elastic waves in a fluid-saturated porous solid. i. low-frequency range. *The Journal of the Acoustical Society of America*, 28(2):168–178, 1956. doi: 10.1121/1.1908239. URL `https://doi.org/10.1121/1.1908239`.

[22] Anna Färm. *Absorption of Sound: On the effects of field interaction on absorber performance*. PhD thesis, KTH Royal Institute of Technology, 2016.

[23] Lawrence E. Kinsler, Austin R. Frey, Alan B. Coppens, and James V. Sanders. *Fundamentals of Acoustics, 4th Edition*. John Wiley & Sons, 1999.

[24] NASA. Turbofan Engine Acoustic Liner Design and Analysis Tools, 2015. URL `https://technology.nasa.gov/patent/LAR-TOPS-185`.

[25] Rie Sugimoto, R Jeremy Astley, and Paul B Murray. Low frequency liners for turbofan engines. In *Proceedings of the 20th International Congress on Acoustics*, page 4. Australian Acoustical Soc. Sydney, Australia, 2010.

[26] Brandon L Bertolucci. *An experimental investigation of the grazing flow impedance duct at the University of Florida for acoustic liner applications*. University of Florida, 2012.

[27] V. G. Veselago. The Electrodynamics of Substances with Simultaneously Negative Values of $\in$ and μ. *Soviet Physics Uspekhi*, 10:509, January 1968. doi: 10.1070/PU1968v010n04ABEH003699.

[28] J. B. Pendry, A. J. Holden, D. J. Robbins, and W. J. Stewart. Magnetism from conductors and enhanced nonlinear phenomena. *IEEE Transactions on Microwave Theory and Techniques*, 47(11):2075–2084, Nov 1999. ISSN 0018-9480. doi: 10.1109/22.798002.

[29] J. B. Pendry, A. J. Holden, W. J. Stewart, and I. Youngs. Extremely low frequency plasmons in metallic mesostructures. *Phys. Rev. Lett.*, 76:4773–4776, Jun 1996. doi: 10.1103/PhysRevLett.76.4773. URL `https://link.aps.org/doi/10.1103/PhysRevLett.76.4773`.

[30] D. R. Smith, Willie J. Padilla, D. C. Vier, S. C. Nemat-Nasser, and S. Schultz. Composite medium with simultaneously negative permeability and permittivity. *Phys. Rev. Lett.*, 84:4184–4187, May 2000. doi: 10.1103/PhysRevLett.84.4184. URL `https://link.aps.org/doi/10.1103/PhysRevLett.84.4184`.

[31] J. B. Pendry. Negative refraction makes a perfect lens. *Phys. Rev. Lett.*, 85: 3966–3969, Oct 2000. doi: 10.1103/PhysRevLett.85.3966. URL `https://link.aps.org/doi/10.1103/PhysRevLett.85.3966`.

[32] Minkyung Kim and Junsuk Rho. Metamaterials and imaging. *Nano Convergence*, 2(1):22, November 2015. ISSN 2196-5404. doi: 10.1186/s40580-015-0053-7. URL `https://doi.org/10.1186/s40580-015-0053-7`.

[33] P.A. Deymier. *Acoustic Metamaterials and Phononic Crystals*. Springer Series in Solid-State Sciences. Springer Berlin Heidelberg, 2013. ISBN 978-3-642-31232-8. URL https://books.google.fr/books?id=8eg_AAAAQBAJ.

[34] W.S. Weiglhofer and A. Lakhtakia. *Introduction to Complex Mediums for Optics and Electromagnetics*. Press Monographs. SPIE Press, 2003. ISBN 978-0-8194-4947-4. URL https://books.google.fr/books?id=QtIP_Lr3gngC.

[35] Tie Jun Cui, David Smith, and Ruopeng Liu, editors. *Metamaterials: Theory, Design, and Applications*. Springer US, 2010. ISBN 978-1-4419-0572-7. URL https://www.springer.com/gp/book/9781441905727.

[36] Guancong Ma and Ping Sheng. Acoustic metamaterials: From local resonances to broad horizons. *Science Advances*, 2(2), 2016. doi: 10.1126/sciadv.1501595. URL https://advances.sciencemag.org/content/2/2/e1501595.

[37] Giorgio Palma, Huina Mao, Lorenzo Burghignoli, Peter Göransson, and Umberto Iemma. Acoustic metamaterials in aeronautics. *Applied Sciences*, 8(6):971, 2018.

[38] Zhengyou Liu, Xixiang Zhang, Yiwei Mao, Y. Y. Zhu, Zhiyu Yang, C. T. Chan, and Ping Sheng. Locally Resonant Sonic Materials. *Science*, 289(5485):1734–1736, 2000. ISSN 0036-8075. doi: 10.1126/science.289.5485.1734. URL https://science.sciencemag.org/content/289/5485/1734.

[39] Nicholas Fang, Dongjuan Xi, Jianyi Xu, Muralidhar Ambati, Werayut Srituravanich, Cheng Sun, and Xiang Zhang. Ultrasonic metamaterials with negative modulus. *Nature Materials*, 5(6):452–456, June 2006. ISSN 1476-4660. doi: 10.1038/nmat1644. URL https://doi.org/10.1038/nmat1644.

[40] Jensen Li, K. H. Fung, Z. Y. Liu, Ping Sheng, and Che Ting Chan. Generalizing the concept of negative medium to acoustic waves. In Clifford M. Krowne and Yong Zhang, editors, *Physics of Negative Refraction and Negative Index Materials: Optical and Electronic Aspects and Diversified Approaches*, pages 183–215. Springer Berlin Heidelberg, Berlin, Heidelberg, 2007. ISBN 978-3-540-72132-1. doi: 10.1007/978-3-540-72132-1_8. URL https://doi.org/10.1007/978-3-540-72132-1_8.

[41] Jensen Li and C. T. Chan. Double-negative acoustic metamaterial. *Phys. Rev. E*, 70:055602, Nov 2004. doi: 10.1103/PhysRevE.70.055602. URL https://link.aps.org/doi/10.1103/PhysRevE.70.055602.

[42] Sam Hyeon Lee, Choon Mahn Park, Yong Mun Seo, Zhi Guo Wang, and Chul Koo Kim. Composite acoustic medium with simultaneously negative density and modulus. *Phys. Rev. Lett.*, 104:054301, Feb 2010. doi: 10.1103/PhysRevLett.104.054301. URL https://link.aps.org/doi/10.1103/PhysRevLett.104.054301.

[43] Sam Hyeon Lee, Choon Mahn Park, Yong Mun Seo, Zhi Guo Wang, and Chul Koo Kim. Acoustic metamaterial with negative density. *Physics Letters A*, 373(48):4464 – 4469, 2009. ISSN 0375-9601. doi: https://doi.org/10.1016/j.physleta.2009.10.013. URL http://www.sciencedirect.com/science/article/pii/S0375960109012754.

[44] Sam Hyeon Lee, Choon Mahn Park, Yong Mun Seo, Zhi Guo Wang, and Chul Koo Kim. Acoustic metamaterial with negative modulus. *Journal of Physics: Condensed Matter*, 21(17):175704, mar 2009. doi: 10.1088/0953-8984/21/17/175704. URL https://doi.org/10.1088%2F0953-8984%2F21%2F17%2F175704.

[45] Nicolas Dauchez, Benoit Nennig, and Olivier Robin. Additional sound absorption within a poroelastic lamella network under oblique incidence. *Acta Acustica united with Acustica*, 104(2):211–219, 2018.

[46] Abdelhalim Azbaid El Ouahabi, Victor V Krylov, and DJ O'Boy. Gradient metamaterial layers as impedance matching devices for efficient sound absorption. In *Proceedings of Euronoise 2015, C. Glorieux, Ed., Maastricht*, June 1-3,2015.

[47] Jun Mei, Guancong Ma, Min Yang, Zhiyu Yang, Weijia Wen, and Ping Sheng. Dark acoustic metamaterials as super absorbers for low-frequency sound. *Nature Communications*, 3(1):756, March 2012. ISSN 2041-1723. doi: 10.1038/ncomms1758. URL https://doi.org/10.1038/ncomms1758.

[48] Jung-San Chen, Yu-Bin Chen, Hsin-Jung Tsai, Kuan-Yu Chen, and Li-Chih Chou. Membrane-ring acoustic metamaterials with an orifice. *Materials Research*

Express, 6(9):095802, jul 2019. doi: 10.1088/2053-1591/ab3088. URL https://doi.org/10.1088%2F2053-1591%2Fab3088.

[49] Yufan Tang, Shuwei Ren, Han Meng, Fengxian Xin, Lixi Huang, Tianning Chen, Chuanzeng Zhang, and Tian Jian Lu. Hybrid acoustic metamaterial as super absorber for broadband low-frequency sound. *Scientific Reports*, 7 (1):43340, February 2017. ISSN 2045-2322. doi: 10.1038/srep43340. URL https://doi.org/10.1038/srep43340.

[50] Lara Flanagan, David Heaphy, John Kennedy, Raphaël Leiba, and Henry Rice. Development of acoustic "meta-liners" providing sub-wavelength absorption. *International Journal of Aeroacoustics*, 19(6-8):310–323, 2020. doi: 10.1177/1475472X20954894. URL https://doi.org/10.1177/1475472X20954894.

[51] D. P. Jena, J. Dandsena, and V. G. Jayakumari. Demonstration of effective acoustic properties of different configurations of Helmholtz resonators. *Applied Acoustics*, 155:371 – 382, 2019. ISSN 0003-682X. doi: https://doi.org/10.1016/j.apacoust.2019.06.004. URL http://www.sciencedirect.com/science/article/pii/S0003682X19303500.

[52] Wenqin Wang, Yukun Zhou, Yong Li, and Tong Hao. Aerogels-filled Helmholtz resonators for enhanced low-frequency sound absorption. *The Journal of Supercritical Fluids*, 150:103 – 111, 2019. ISSN 0896-8446. doi: https://doi.org/10.1016/j.supflu.2019.04.011. URL http://www.sciencedirect.com/science/article/pii/S0896844618308507.

[53] John Kennedy, Lara Flanagan, Luke Dowling, G. J. Bennett, Henry Rice, and Daniel Trimble. The Influence of Additive Manufacturing Processes on the Performance of a Periodic Acoustic Metamaterial. *International Journal of Polymer Science*, 2019:7029143, July 2019. ISSN 1687-9422. doi: 10.1155/2019/7029143. URL https://doi.org/10.1155/2019/7029143. Publisher: Hindawi.

[54] Yangbo Xie, Bogdan-Ioan Popa, Lucian Zigoneanu, and Steven A. Cummer. Measurement of a broadband negative index with space-coiling acoustic metamaterials. *Phys. Rev. Lett.*, 110:175501, Apr 2013. doi: 10.1103/PhysRevLett.

110.175501. URL https://link.aps.org/doi/10.1103/PhysRevLett.110.175501.

[55] Yong Li, Xue Jiang, Rui-qi Li, Bin Liang, Xin-ye Zou, Lei-lei Yin, and Jian-chun Cheng. Experimental realization of full control of reflected waves with subwavelength acoustic metasurfaces. *Phys. Rev. Applied*, 2:064002, Dec 2014. doi: 10.1103/PhysRevApplied.2.064002. URL https://link.aps.org/doi/10.1103/PhysRevApplied.2.064002.

[56] Yong Li, Bin Liang, Zhong-ming Gu, Xin-ye Zou, and Jian-chun Cheng. Reflected wavefront manipulation based on ultrathin planar acoustic metasurfaces. *Scientific Reports*, 3(1):2546, August 2013. ISSN 2045-2322. doi: 10.1038/srep02546. URL https://doi.org/10.1038/srep02546.

[57] Y. Cheng, C. Zhou, B. G. Yuan, D. J. Wu, Q. Wei, and X. J. Liu. Ultra-sparse metasurface for high reflection of low-frequency sound based on artificial Mie resonances. *Nature Materials*, 14(10):1013–1019, October 2015. ISSN 1476-4660. doi: 10.1038/nmat4393. URL https://doi.org/10.1038/nmat4393.

[58] Jun Mei and Ying Wu. Controllable transmission and total reflection through an impedance-matched acoustic metasurface. *New Journal of Physics*, 16(12):123007, dec 2014. doi: 10.1088/1367-2630/16/12/123007. URL https://doi.org/10.1088%2F1367-2630%2F16%2F12%2F123007.

[59] J. B. Pendry, D. Schurig, and D. R. Smith. Controlling Electromagnetic Fields. *Science*, 312(5781):1780–1782, 2006. ISSN 0036-8075. doi: 10.1126/science.1125907. URL https://science.sciencemag.org/content/312/5781/1780. Publisher: American Association for the Advancement of Science _eprint: https://science.sciencemag.org/content/312/5781/1780.full.pdf.

[60] Steven A Cummer and David Schurig. One path to acoustic cloaking. *New Journal of Physics*, 9(3):45–45, mar 2007. doi: 10.1088/1367-2630/9/3/045. URL https://doi.org/10.1088%2F1367-2630%2F9%2F3%2F045.

[61] Andrew N Norris. Acoustic cloaking. *Acoust. Today*, 11(1):38–46, 2015.

[62] Andrew N Norris. Acoustic cloaking theory. *Proceedings of the Royal Society A: Mathematical, Physical and Engineering Sciences*, 464(2097):2411–2434, 2008.

[63] T. Bückmann, M. Thiel, M. Kadic, R. Schittny, and M. Wegener. An elasto-mechanical unfeelability cloak made of pentamode metamaterials. *Nature Communications*, 5(1):4130, June 2014. ISSN 2041-1723. doi: 10.1038/ncomms5130. URL https://doi.org/10.1038/ncomms5130.

[64] Reza Hedayati and Sandhya Lakshmanan. Pneumatically-Actuated Acoustic Metamaterials Based on Helmholtz Resonators. *Materials (Basel, Switzerland)*, 13(6):1456, March 2020. ISSN 1996-1944. doi: 10.3390/ma13061456. URL https://pubmed.ncbi.nlm.nih.gov/32210047. Publisher: MDPI.

[65] Josh Bishop-Moser, Chris Spadaccini, and Christine Andres. Metamaterials manufacturing: Pathway to industrial competitiveness. Technical report, MForesight: Alliance for Manufacturing Foresight, 2018.

[66] AERIALIST. Wp3 - principal outcomes, 2020. URL https://www.aerialist-project.eu/wp3-outcomes/.

[67] ZHU Zuowei, Safa Keimasi, Nabil Anwer, Luc Mathieu, and QIAO Lihong. Review of shape deviation modeling for additive manufacturing. In *Advances on Mechanics, Design Engineering and Manufacturing*, pages 241–250. Springer, 2017.

[68] Mariano Jiménez, Luis Romero, Iris A. Domínguez, María del Mar Espinosa, and Manuel Domínguez. Additive Manufacturing Technologies: An Overview about 3D Printing Methods and Future Prospects. *Complexity*, 2019:9656938, February 2019. ISSN 1076-2787. doi: 10.1155/2019/9656938. URL https://doi.org/10.1155/2019/9656938. Publisher: Hindawi.

[69] Fei Chen, Gary Mac, and Nikhil Gupta. Security features embedded in computer aided design (CAD) solid models for additive manufacturing. *Materials & Design*, 128:182 – 194, 2017. ISSN 0264-1275. doi: https://doi.org/10.1016/j.matdes.2017.04.078. URL http://www.sciencedirect.com/science/article/pii/S0264127517304355.

[70] Kaufui V. Wong and Aldo Hernandez. A Review of Additive Manufacturing. *ISRN Mechanical Engineering*, 2012:208760, August 2012. ISSN xxxx-xxxx. doi: 10.5402/2012/208760. URL https://doi.org/10.5402/2012/208760. Publisher: International Scholarly Research Network.

[71] Ian Gibson, David W Rosen, Brent Stucker, et al. *Additive manufacturing technologies*, volume 17. Springer, 2014.

[72] L. Dowling, J. Kennedy, S. O'Shaughnessy, and D. Trimble. A review of critical repeatability and reproducibility issues in powder bed fusion. *Materials & Design*, 186:108346, 2020. ISSN 0264-1275. doi: https://doi.org/10.1016/j.matdes.2019.108346. URL http://www.sciencedirect.com/science/article/pii/S0264127519307841.

[73] Masoumeh Aminzadeh. A machine vision system for in-situ quality inspection in metal powder-bed additive manufacturing. 2016.

[74] Tomasz G. Zieliński, Kamil C. Opiela, Piotr Pawłowski, Nicolas Dauchez, Thomas Boutin, John Kennedy, Daniel Trimble, Henry Rice, Bart Van Damme, Gwenael Hannema, Rafał Wróbel, Seok Kim, Shahrzad Ghaffari Mosanenzadeh, Nicholas X. Fang, Jieun Yang, Baltazar Briere de La Hosseraye, Maarten C. J. Hornikx, Edouard Salze, Marie-Annick Galland, René Boonen, Augusto Carvalho de Sousa, Elke Deckers, Mathieu Gaborit, and Jean-Philippe Groby. Reproducibility of sound-absorbing periodic porous materials using additive manufacturing technologies: Round robin study. *Additive Manufacturing*, 36:101564, 2020. ISSN 2214-8604. doi: https://doi.org/10.1016/j.addma.2020.101564. URL http://www.sciencedirect.com/science/article/pii/S2214860420309362.

[75] Willem M. Beltman, Ysbrand H. Wijnant, and Marten J. Nijhof. An overview of models for viscothermal wave propagation, including fluid structure interaction. *The Journal of the Acoustical Society of America*, 123(5):3420–3420, 2008. doi: 10.1121/1.2934166. URL https://doi.org/10.1121/1.2934166.

[76] WR Kampinga, Ysbrand H Wijnant, and Andries de Boer. An efficient finite element model for viscothermal acoustics. *Acta Acustica united with Acustica*, 97 (4):618–631, 2011. ISSN 1610-1928.

[77] Miguel Molerón, Marc Serra-Garcia, and Chiara Daraio. Visco-thermal effects in acoustic metamaterials: from total transmission to total reflection and high absorption. *New Journal of Physics*, 18(3):033003, mar 2016. doi: 10.1088/1367-2630/18/3/033003. URL https://doi.org/10.1088/1367-2630/18/3/033003.

[78] COMSOL COMSOL. 5.5 acoustics module user's guide, 2019.

[79] H von Helmholtz. On the influence of friction in the air on sound motion. *Verhandl. Naturhist. Med. Ver. Heidelberg*, 3:16–20, 1863.

[80] Philip A. Cotterill, David Nigro, I. David Abrahams, Erik Garcia-Neefjes, and William J. Parnell. Thermo-viscous damping of acoustic waves in narrow channels: A comparison of effects in air and water. *The Journal of the Acoustical Society of America*, 144(6):3421–3436, 2018. doi: 10.1121/1.5078528. URL https://doi.org/10.1121/1.5078528.

[81] G. Kirchhoff. Ueber den Einfluss der Wärmeleitung in einem Gase auf die Schallbewegung. *Annalen der Physik*, 210(6):177–193, 1868. doi: 10.1002/andp.18682100602. URL https://onlinelibrary.wiley.com/doi/abs/10.1002/andp.18682100602.

[82] Sjoerd W Rienstra and Avraham Hirschberg. An introduction to acoustics. *Eindhoven University of Technology*, 18:19, 2004.

[83] Philip McCord Morse and K Uno Ingard. *Theoretical acoustics*. Princeton university press, 1986.

[84] Tomasz G ZIELINSKI. Fundamentals of fluid dynamics: Elementary viscous flow [online].[cit. 16.9. 2016]. *Dostupnỳ na WWW: http://bluebox. ippt. pan. pl/˜ tzielins/doc/ICMM_TGZielinski_ViscousFlow. slides. pdf*, 2016.

[85] D.J. Acheson and F.D.J. Acheson. *Elementary Fluid Dynamics*. Comparative Pathobiology - Studies in the Postmodern Theory of Education. Clarendon Press, 1990. ISBN 978-0-19-859679-0. URL https://books.google.fr/books?id=IGfDBAAAQBAJ.

[86] Guido Buresti. A note on stokes' hypothesis. *Acta Mechanica*, 226(10):3555–3559, 2015.

[87] D.T. Blackstock. *Fundamentals of Physical Acoustics*. A Wiley-Interscience publication. Wiley, 2000. ISBN 978-0-471-31979-5. URL https://books.google.fr/books?id=5N-ZDwAAQBAJ.

[88] MJJ Nijhof, Ysbrand H Wijnant, and Andries De Boer. An acoustic finite element including viscothermal effects. In *in Proceedings of the 14th International Congress on Sound and Vibration*. Citeseer, 2007.

[89] W.R. Kampinga. *Viscothermal acoustics using finite elements - Analysis tools for engineers*. PhD thesis, University of Twente, Netherlands, 6 2010.

[90] Martin Berggren, Anders Bernland, and Daniel Noreland. Acoustic boundary layers as boundary conditions. *Journal of Computational Physics*, 371:633–650, Oct 2018. ISSN 0021-9991. doi: 10.1016/j.jcp.2018.06.005. URL http://dx.doi.org/10.1016/j.jcp.2018.06.005.

[91] WR Kampinga, Ysbrand H Wijnant, and Andries de Boer. Performance of several viscothermal acoustic finite elements. *Acta acustica united with Acustica*, 96(1): 115–124, 2010.

[92] H.J. Rice, J. Kennedy, P. Göransson, L. Dowling, and D. Trimble. Design of a kelvin cell acoustic metamaterial. *Journal of Sound and Vibration*, 472:115167, 2020. ISSN 0022-460X. doi: https://doi.org/10.1016/j.jsv.2019.115167. URL https://www.sciencedirect.com/science/article/pii/S0022460X19307308.

[93] Olek C Zienkiewicz, Robert L Taylor, and Jian Z Zhu. *The finite element method: its basis and fundamentals*. Elsevier, 2005.

[94] Peter Risby Andersen. *Modelling of acoustic viscothermal losses using the Boundary Element Method: From method to optimization*. PhD thesis, 2018.

[95] Derek Michael Forrester, Jinrui Huang, and Valerie J. Pinfield. Modelling viscous boundary layer dissipation effects in liquid surrounding individual solid nano and

micro-particles in an ultrasonic field. *Scientific Reports*, 9(1):4956, March 2019. ISSN 2045-2322. doi: 10.1038/s41598-019-40665-9. URL https://doi.org/10.1038/s41598-019-40665-9.

[96] WR Kampinga and YH Wijnant. Comsol's new thermoacoustics interface and computationally efficient alternative formulations for fem. In *2011 COMSOL Conference, Stuttgart*, Stuttgart, Germany, 2011. Comsol.

[97] René Christensen. Topology optimization of thermoviscous acoustics in tubes and slits with hearing aid applications. In *COMSOL Conference*, 2017.

[98] John William Strutt Baron Rayleigh. *Theory of Sound*. Macmillan, London, 1877.

[99] G. P. Ward, R. K. Lovelock, A. R. J. Murray, A. P. Hibbins, J. R. Sambles, and J. D. Smith. Boundary-layer effects on acoustic transmission through narrow slit cavities. *Phys. Rev. Lett.*, 115:044302, Jul 2015. doi: 10.1103/PhysRevLett.115.044302. URL https://link.aps.org/doi/10.1103/PhysRevLett.115.044302.

[100] C. Zwikker and Cornelis Willem. Kosten. *Sound absorbing materials*. Number ix, 174 p. Elsevier Pub. Co., New York, 1949. URL //catalog.hathitrust.org/Record/001479870.

[101] H. Tijdeman. On the propagation of sound waves in cylindrical tubes. *Journal of Sound and Vibration*, 39(1):1–33, March 1975. ISSN 0022-460X. doi: 10.1016/S0022-460X(75)80206-9. URL http://www.sciencedirect.com/science/article/pii/S0022460X75802069.

[102] David Oliva and Valtteri Hongisto. Sound absorption of porous materials – Accuracy of prediction methods. *Applied Acoustics*, 74(12):1473–1479, December 2013. ISSN 0003-682X. doi: 10.1016/j.apacoust.2013.06.004. URL http://www.sciencedirect.com/science/article/pii/S0003682X13001382.

[103] Yasushi Miki. Acoustical properties of porous materials-Modifications of Delany-Bazley models. *Journal of the Acoustical Society of Japan (E)*, 11(1):19–24, 1990. ISSN 0388-2861.

[104] Jean Allard and Noureddine Atalla. *Propagation of sound in porous media: modelling sound absorbing materials 2e*. John Wiley & Sons, 2009.

[105] F.J. Fahy. *Foundations of Engineering Acoustics*. Elsevier Science, 2001. ISBN 978-0-12-247665-5. URL https://books.google.ie/books?id=EDnwlpOUqDoC.

[106] Jean-Louis Auriault, Claude Boutin, and Christian Geindreau. *Homogenization of coupled phenomena in heterogenous media*, volume 149. John Wiley & Sons, 2010.

[107] K.R. Rajagopal. A new development and interpretation of the navier–stokes fluid which reveals why the "stokes assumption" is inapt. *International Journal of Non-Linear Mechanics*, 50:141–151, 2013. ISSN 0020-7462. doi: https://doi.org/10.1016/j.ijnonlinmec.2012.10.007. URL https://www.sciencedirect.com/science/article/pii/S0020746212001655.

[108] L. Brekhovskikh. *Waves in Layered Media*. Applied mathematics and mechanics. Elsevier Science, New York, 1980. ISBN 978-0-323-16162-6.

[109] S. Y. Song, X. H. Yang, F. X. Xin, S. W. Ren, and T. J. Lu. Modeling of roughness effects on acoustic properties of micro-slits. *Journal of Physics D: Applied Physics*, 50(23):235303, May 2017. ISSN 0022-3727 1361-6463. doi: 10.1088/1361-6463/aa6fa1. URL http://dx.doi.org/10.1088/1361-6463/aa6fa1.

[110] British Standards Institution. Iso 10534-2:1998 acoustics: determination of sound absorption coefficient and impedance in impedance tubes - part 2: Transfer function method. *British Standards Institution*, 1998. ISSN 9780580324628 0580324621. OCLC: 958821240.

[111] Erlend Magnus Viggen. The lattice boltzmann method: Fundamentals and acoustics. 2014.

[112] AERIALIST-Horizon 2020. Simulation of benchmark, aerialist deliverable 2.5, jun 2019.

[113] Michail Papanikolaou, Michael Frank, and Dimitris Drikakis. Effects of surface roughness on shear viscosity. *Phys. Rev. E*, 95:033108, Mar 2017. doi: 10.1103/

PhysRevE.95.033108. URL https://link.aps.org/doi/10.1103/PhysRevE.95.033108.

[114] ManishKumar Gupta and Monika Singh. Comparison between metamaterial based circular patch antenna and microstrip patch antenna. *International Journal of Engineering Research and Applications (IJERA)*, 2(3):574–579, 2012.

[115] Bichoy Bahr, Luca Daniel, and Dana Weinstein. Optimization of unreleased cmos-mems rbts. In *2016 IEEE International Frequency Control Symposium (IFCS)*, pages 1–4. IEEE, 2016.

[116] Lawrence T Pillage and Ronald A Rohrer. Asymptotic waveform evaluation for timing analysis. *IEEE Transactions on Computer-Aided Design of Integrated Circuits and Systems*, 9(4):352–366, 1990.

[117] B. Brouard, D. Lafarge, and J.-F. Allard. A general method of modelling sound propagation in layered media. *Journal of Sound and Vibration*, 183(1):129–142, 1995. ISSN 0022-460X. doi: https://doi.org/10.1006/jsvi.1995.0243. URL https://www.sciencedirect.com/science/article/pii/S0022460X8570243X.

[118] T.H. Melling. The acoustic impendance of perforates at medium and high sound pressure levels. *Journal of Sound and Vibration*, 29(1):1–65, 1973. ISSN 0022-460X. doi: https://doi.org/10.1016/S0022-460X(73)80125-7. URL https://www.sciencedirect.com/science/article/pii/S0022460X73801257.

[119] Michael R. Stinson. The propagation of plane sound waves in narrow and wide circular tubes, and generalization to uniform tubes of arbitrary cross-sectional shape. *The Journal of the Acoustical Society of America*, 89(2):550–558, 1991. doi: 10.1121/1.400379. URL https://doi.org/10.1121/1.400379.

[120] Jean Boulvert, Théo Cavalieri, Josué Costa-Baptista, Logan Schwan, Vicente Romero-García, Gwénaël Gabard, Edith Roland Fotsing, Annie Ross, Jacky Mardjono, and Jean-Philippe Groby. Optimally graded porous material for broadband perfect absorption of sound. *Journal of Applied Physics*, 126(17):175101, 2019. doi: 10.1063/1.5119715. URL https://doi.org/10.1063/1.5119715.

[121] TG Zielinski. Pore-size effects in sound absorbing foams with periodic microstructure: modelling and experimental verification using 3d printed specimens. In *Proceedings of Isma2016 international conference on noise and vibration engineering and Usd2016 international conference on uncertainty in structural dynamics*, pages 95–104, 2016.

[122] Jean Boulvert, Josué Costa-Baptista, Théo Cavalieri, Maxime Perna, Edith Roland Fotsing, Vicente Romero-García, Gwénaël Gabard, Annie Ross, Jacky Mardjono, and Jean-Philippe Groby. Acoustic modeling of micro-lattices obtained by additive manufacturing. *Applied Acoustics*, 164:107244, 2020. ISSN 0003-682X. doi: https://doi.org/10.1016/j.apacoust.2020.107244. URL `https://www.sciencedirect.com/science/article/pii/S0003682X19307297`.

[123] Camille Perrot. 3d printing of porous sound absorbers. UKAN 3D printed porous absorbers workshop, 4 2020.

[124] Michael G Jones, Willie R Watson, Douglas M Nark, Brian M Howerton, and Martha C Brown. A review of acoustic liner experimental characterization at nasa langley. *NASA TP*, 220583, 2020.

[125] Andrea Giglio and Ingrid Paoletti. Scenario for embedding ai in acoustic design . exploiting applications at several design stages. 2019.

[126] Arthur Terroir, Logan Schwan, Théo Cavalieri, Vicente Romero-García, Gwénaël Gabard, and Jean-Philippe Groby. General method to retrieve all effective acoustic properties of fully-anisotropic fluid materials in three dimensional space. *Journal of Applied Physics*, 125(2):025114, 2019. doi: 10.1063/1.5066608. URL `https://doi.org/10.1063/1.5066608`.

[127] Denis Lafarge, Pavel Lemarinier, Jean F. Allard, and Viggo Tarnow. Dynamic compressibility of air in porous structures at audible frequencies. *The Journal of the Acoustical Society of America*, 102(4):1995–2006, 1997. doi: 10.1121/1.419690. URL `https://doi.org/10.1121/1.419690`.

[128] Cavalieri,Théo and Boulvert,Jean. Practical session on design/manufacturing and characterization of porous materials.

[129] Thomas Humbert. Optical duct facility of laum general informations, 2020.

Appendix A

Evaluation of absorptive behaviour using an equivalent fluid approach

A.1 Introduction to multiscale modelling for acoustic structures

In relation to the configurations examined in this thesis, a direct approach was chosen to examine the impact of defects within the structure, caused by the manufacturing processes employed. As waves propagate through such materials, viscous and thermal effects are induced. In order to analyse their acoustic behaviour it is necessary to first obtain their effective parameters. The principle of homogenisation allows to zoom out from the unit structure. When dealing with a periodic media, the problem can be treated as an equivalent continuous medium [106]. Describing small scale heterogeneities on a unit cell is a complicated process, especially in the case of a printed structure. If a large volume is composed of many small-scale heterogeneities, modelling these numerically can be difficult and expensive. Homogenisation is an upscaling method which is analogous to an averaging process over a larger scale. In the studies carried out throughout this thesis, there was a clear separation of scales, examining the acoustic effects on a unit cell and using transformation methods to obtain the acoustic performance of a built up structure. This process is referred to as a micro to macro approach. The multiple scale approach separates what occurs internally at a microscopic level and the effective fields at a macroscopic level [106]. The unit cells that were analysed are all periodic structures therefore, homogenisation seems like a reasonable approach. Through homogenisation, the homogeneous effective parameters are extracted from the heterogeneous media. These extracted effective parameters can then be substituted in propagation models to obtain their behaviour at different length scales. The equivalent fluid approach which reposes on the theory of two scale asymptotic homogenisation was used to extract the JCAL transport parameters, its theory is outlined in Section A.1.1.

A.1.1 Two scale asymptotic homogenisation procedure

The finite element method code from COMSOL was used to calculate the quantities that describe the behaviour inside the structure. Once these parameters have been evaluated they were substituted inside the JCAL model. The unit cell which was modelled in COMSOL is an idealised model which does not take into account internal defects. some studies have been performed where effective parameters are inversely

characterised through experimental procedures and then substituted into propagation models to determine a macro scale behaviour [120]. In order to carry out two-scale asymptotic homogenisation a representative volume of a unit must be determined. The unit structure is evaluated and the transport parameters are then derived and computed, which can be done through FEM in COMSOL [120]. The homogenization method is applied to the governing equations 2.1 to 2.3 on the representative volume. The JCAL parameters are derived by integrating the solution fields to these equations over the fluid domain, Ω_f, or the fluid-solid interface, Γ. The solution fields are outlined bellow arising from the viscous and thermal cell problem.

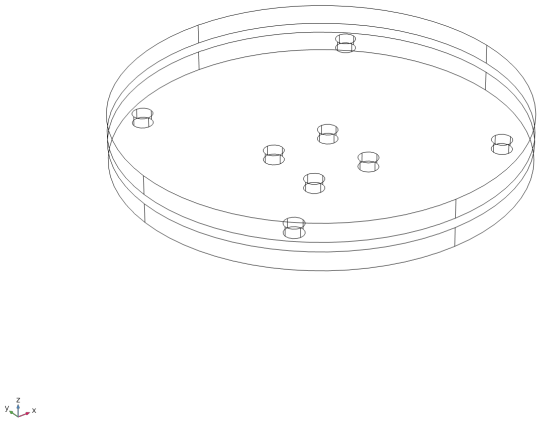

Figure A.1: Representative volume AC of unit cell size, l_c with orthonormal basis (e_1, e_2, e_3).

Visco-inertial effects

The visco-inertial cell problem is composed of the incompressible stokes flow through the unit cell in response to a pressure gradient. The cell is considered in its main direction where the dynamic tensor of viscous permeability is diagonal, the visco-inertial equations are outlined in [126]. The numerical model for tortuosity was built in COMSOL in the normal direction, e_3 for the fluid volume, Ω_f. The following parameters are direction dependent denoted by the direction x_j.

High frequency limit of the tortuosity, τ_{33}^{∞}

$$\tau_{33}^{\infty} = \phi\left\langle e_3 - {}^{T}\nabla_y \zeta_3^{\infty}\right\rangle^{-1} \cdot e_3 \tag{A.1}$$

Characteristic viscous length in normal direction, λ_3^∞

$$\lambda_3 = 2\frac{\int_{\Omega_f}(e_3 - \nabla_y\zeta_3^\infty)^2 d\Omega_y}{\int_\Gamma(e_3 - \nabla_y\zeta_3^\infty)^2 d\Gamma} \tag{A.2}$$

The numerical model to obtain the Darcy permeability a creeping flow model was created in COMSOL, and the permeability was integrated over the fluid volume the unit cell AC.

Static viscous permeability, q_{33}^0

$$q_{33}^0 = \frac{1}{|\Omega|_y}\int_{\Omega_f} k_3^0 d\Omega_y \tag{A.3}$$

Thermo-acoustic effect

The thermo-acoustic effect in the cell consists of the heat conduction through the unit cell loaded by a constant pressure. the homogenisation process of the constitutive equations in [106, 126]leads to the temperature field at the local scale. The thermostatic problem was evaluated in COMSOL with the coefficient form PDE interface.

Open porosity, ϕ

$$\phi = \frac{1}{|\Omega|_y}\int_{\Omega_f} d\Omega_y \tag{A.4}$$

Thermal characteristic length, Λ'

$$\Lambda' = 2\frac{\int_{\Omega_f}(\theta^\infty \cdot \theta^\infty)d\Omega_y}{\int_\Gamma(\theta^\infty \cdot \theta^\infty)d\Gamma} = 2\frac{|\Omega|_y}{|\Gamma|} \tag{A.5}$$

Static thermal permeability, Θ^0

$$\Theta^0 = \frac{1}{|\Omega|_y}\int_{\Omega f} \theta^0 d\Omega_y \tag{A.6}$$

A.1.2 Johnson-Champoux-Allard-Lafarge propagation model

The transport parameters are used to estimate the dynamic viscous and thermal permeabilities. The frequency dependent macroscopic viscous and thermal permeabilities can be obtained from the asymptotic regime at low and high frequencies [127]. The dynamic viscous and thermal permeabilities are given by Equations A.8. The trans-

port parameters determined numerically are used to estimate the shape factors M_j and $M_{\prime}$ and characteristic frequencies ω_j and $\omega_{\prime}$ for the viscous and thermal permeabilities respectively. The characteristic frequency ω_j denotes the transition between static and viscous regions and $\omega_{\prime}$ the isothermal to adiabatic transition.

$$M_j = \frac{8\tau_{jj}^{\infty} K_{jj}^{0}}{\Lambda_j^2 \phi} \qquad M^{'} = \frac{8\Theta^0}{\phi \Lambda^{\prime 2}}$$
$$\omega_j = \frac{\mu\phi}{\rho_0 K_{jj}^{0} \tau_{jj}^{\infty}} \quad \omega_{\prime} = \frac{\kappa\phi}{\Theta^0 \rho_0 c_p} \tag{A.7}$$

where ρ_0 is the density, c_p the heat capacity, μ the dynamic viscosity and κ the thermal conductivity of the air.

$$q_{jj}^{\omega} = \frac{q_{jj}^{0}}{\sqrt{1 - \jmath\frac{\omega}{\omega_j}\frac{M_j}{2} - \jmath\frac{\omega}{\omega_j}}} \quad \text{where} j \in \{1,2,3\}$$
$$\Theta^{\omega} = \frac{\Theta^0}{\sqrt{1 - \jmath\frac{\omega}{\omega^{\prime}}\frac{M^{'}}{2} - \jmath\frac{\omega}{\omega^{\prime}}}} \tag{A.8}$$

The effective density and bulk modulus in Equations A.9 and A.10 can be obtained from the homogenised permeabilities in Equation A.8 [128].

$$\rho(\omega) = \frac{\eta}{-\jmath\omega} \left[q^{\omega}\right]^{-1} \tag{A.9}$$

$$K(\omega) = \frac{K_0}{\phi\gamma + \jmath\omega\rho_0 c_p (\gamma - 1)\Theta^{\omega}/\kappa} \tag{A.10}$$

The fluid properties used to estimate the effective parameters are outlined in A.1.

Symbol	Value	Unit	
K_0	101325	K	Bulk modulus
ρ_0	1.2043	kg/m^3	Density
μ	1.8132E-05	$Pa.s$	Dynamic viscosity
c_0	342	m/s	Speed of sound
C_p	1005	$J/(kgK)$	Specific heat capacity
κ	0.025756	$W/(mK)$	Thermal conductivity
Pr_0	0.7075	-	Prandtl number
D_{th}	2.128-05	m^2/s	Thermal diffusivity

Table A.1: Fluid properties-equivalent fluid model.

A.1.3 Estimation of aborptivity from JCAL model for unit AC

A normal incident plane wave of frequency ω propagates in an impedance tube of domain Ω_0 and impinges on the porous sample Ω of thickness L=0.006m presented in Figure A.1, backed by an impervious layer. In the normal direction the incident and reflected waves travelling in the tube are defined by Equation A.11.

$$\begin{aligned} p^i(x,\omega) &= e^{-\jmath k_0(x_3-L)} \\ p^r(x,\omega) &= \overline{R}(\omega)e^{\jmath k_0(x_3-L)} \end{aligned} \tag{A.11}$$

In the porous sample the effective properties are defined by Equations A.9 and A.10. The transfer matrix outlined in 3 can be used to obtain the solution to the wave propagation problem of the characteristic cell and the built-up structure. The loading variables are known, $\begin{Bmatrix} p \\ v_3 \end{Bmatrix}$ and used to solve the field variables at the interface of the sample (inlet and outlet).

$$\begin{Bmatrix} p \\ v_3 \end{Bmatrix}_L = \underbrace{expm\left\{ L \begin{bmatrix} 0 & \jmath\omega\rho_{33} \\ \jmath\omega/K & 0 \end{bmatrix} \right\}}_{TM} \begin{Bmatrix} p \\ 0 \end{Bmatrix}_0 \tag{A.12}$$

$$R = \frac{\dfrac{TM_{11}}{TM_{21}} + Z_0}{\dfrac{TM_{11}}{TM_{21}} - Z_0} \tag{A.13}$$

$$\alpha = 1 - |R|^2 \tag{A.14}$$

The transport parameters were obtained numerically from the equivalent fluid approach detailed previously. These were then substituted to obtain the effective parameters of the medium. The absorptivity obtained through the JCAL model is displayed in Figure A.2. This is compared with the numerical models used to determine the absorptivity of the AC unit and the experimental measurements on a printed PLA cell under normal incidence.

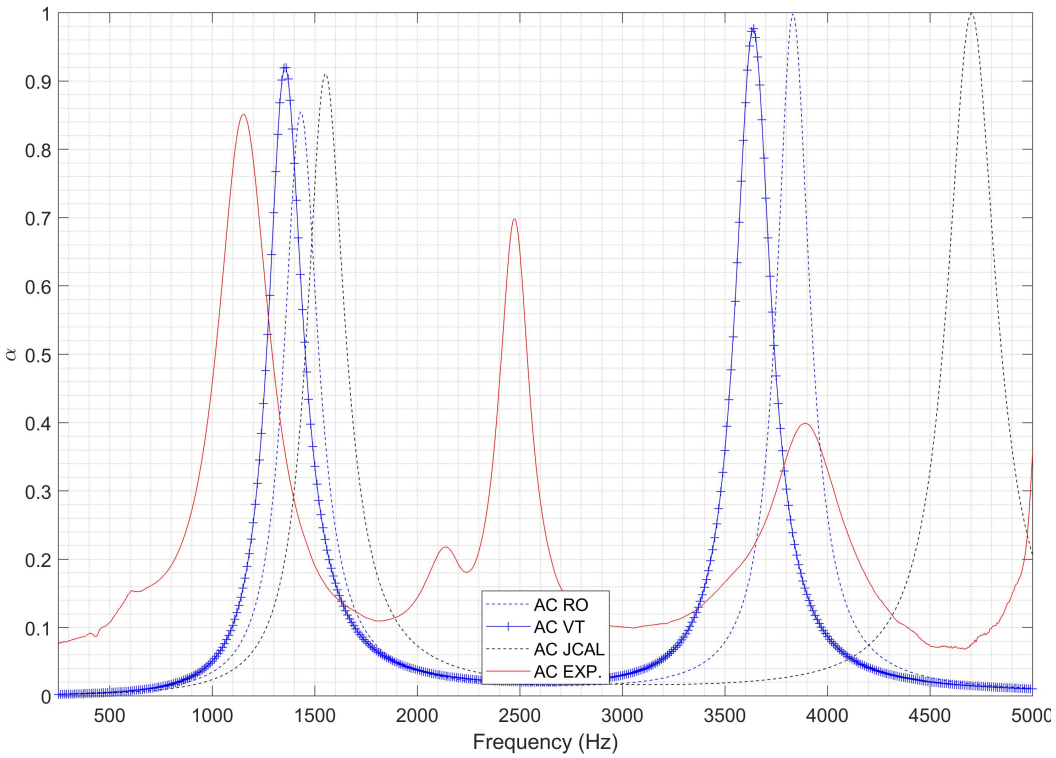

Figure A.2: Results from JCAL propagation model where parameters were determined through homogenisation for the plate design AC.

It can be seen that there is an overestimation of the first resonant frequency with the JCAL model. In comparison with the direct numerical models, the viscothermal and reduced order provide a closer match to experiment using an equivalent fluid might not be the best approach. The two numerical models plotted in blue are acoustic-structural models and were reviewed in Chapter 4. The mode located at 2500 Hz is suspected to be a structural resonance and a discussion on the reasoning for this has been provided. In order for the homogenisation approach to be effective it is necessary to zoom in on a cell within the periodic medium which is representative of the existing geometry. In the assessment, using homogenisation for the problem under consideration might

not be truly representative of the problem. With this asymptotic method it was possible to recover the reflection coefficient for the structure. The parameters obtained numerically represent the unit in a purely geometric sense. For the unit volume to properly represent the heterogeneities, only inverse characterisation methods of the sample would satisfy this as the microstructure is the main factor which influences the transport parameters. Even if inverse characterisation of the sample is possible with experimental measurements, a precise description of the microstructure is difficult to obtain.

In conclusion, for the geometry considered there is more fidelity in the results obtained through the reduced order and viscothermal models, as it is within the experimental error tolerated with experimental tests. The homogenisation approach which is an averaging method is in the author's view a step further in the approximation of dissipative effects, and should not be privileged in the modelling of sub-wavelength structures.

Appendix B

Acoustic treatments under grazing incidence and external grazing flow

B.1 Introduction

The structures analysed as part of this thesis are set in a linear acoustic regime. Some preliminary experimental work has been carried out on some of these structures to assess their stability in other environmental conditions in collaboration with Thomas Humbert, research engineer at the LAUM and Yves Aurègan, research director at the CNRS (UMR CNRS 6613). The experimental grazing incidence test bench at the LAUM (Laboratoire d'Acoustique de l'Université du Mans) where experimental work was carried out on a number of samples manufactured for this testing campaign is shown in Figure B.1.

Figure B.1: Grazing incidence test bench facility at the LAUM, Le Mans [129].

This test bench is composed of a section 40x50 mm^2 and the lined section is 200 mm in length. There are two acoustic sources which are used to obtain measurements upstream and downstream of the sample and two anechoic terminations. The acoustic measurements were carried out by 20 face to face microphones by impedance eduction. The flow measurements were carried out using a pitot tube. The three samples manufactured are 190 mm long and 50 mm wide. A holder was manufactured to fit in the acoustic testing section in B.2(a) which was used in one of the measurements but due to clamping issues it was then substituted for the holder shown in Figure B.2.

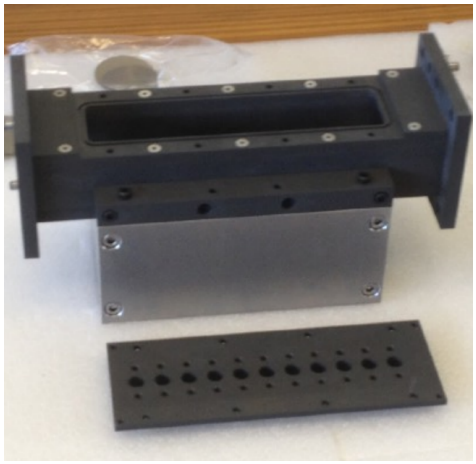

(a) Sample holder

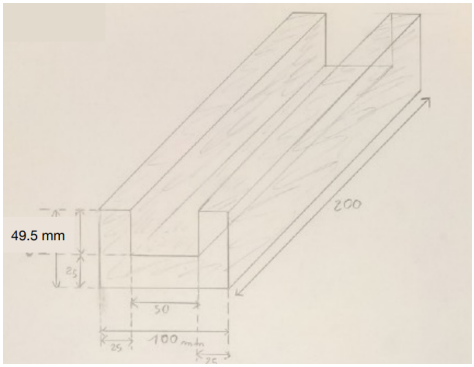

(b) Section of sample holder

Figure B.2: Sample holder for acoustic measurements at LAUM [129].

A swept sine excitation from 100 Hz to 4000 Hz with a 5 Hz step is used for acoustic impedance eduction. Transmission coefficients for upstream and downstream waves are obtained measuring the pressure at different location on both sides of the sample. The impedance of the lined section was obtained by an inverse method based on multimodal calculations to match numerical and experimental scattering matrices. For the experiments performed the pressure was averaged over 200 cycles at each frequency and in the presences of flow it was averaged over 1000 cycles. The cut off frequency for plane wave propagation in the tube is 3500 Hz.

One of the structures examined in Chapter 2 based on a unit cell amenable to additive manufacture put forward by the COST action DENORMS was assessed under grazing incidence in the presence of external flow. Details of the results obtained on the labyrinthine DENORMS structure are presented in B.2. Two other plate structures were also tested under grazing. One which was previously examined under normal incidence in Chapter 3 and whose main findings were published in [50]. The other which is based on the AC cell unit structure of which most results attesting of its acoustic behaviour are detailed in Chapter 4.

B.2 Grazing incidence results for DENORMS cell configuration

One of the built-up structure based on the design proposed by the COST action DENORMS was manufactured to be the tested in the grazing rig presented previously.

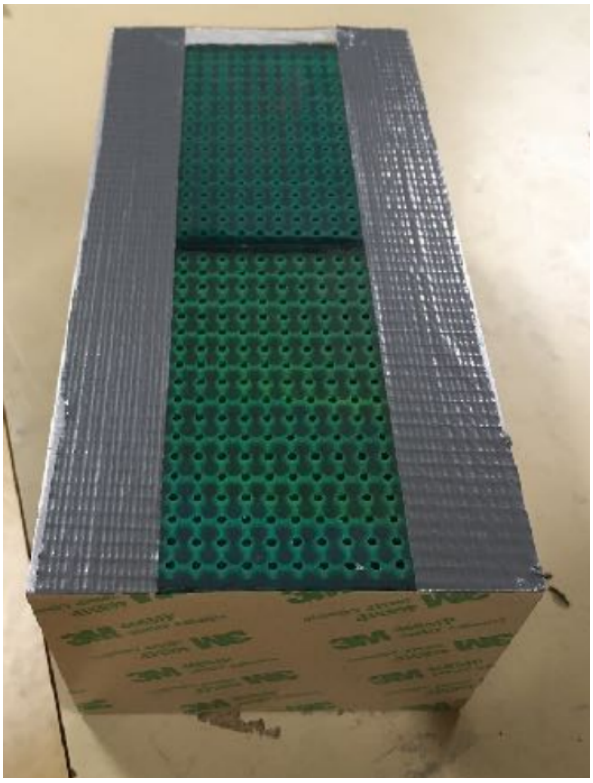

(a) Denorms labyrinthine structure

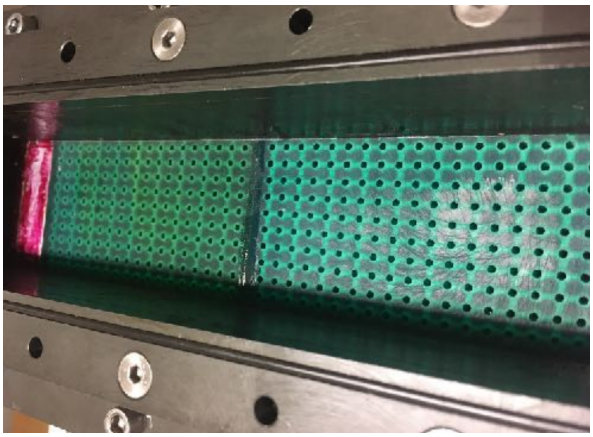

(b) Sample in holder

Figure B.3: Denorms labyrinthine sample manufactured for grazing incidence testing.

It was manufactured using an Anycubic photon DLP printer. This labyrinthine set-up doubles the length of the number of resonators through a space coiling mechanism. The sample was printed in two separate 50 mm x 50 mm, 100 mm long samples due to build plate constraints. The sample within the holder is presented in a U-shaped holder in Figure B.3(a). The sample was placed in its regular orientation in the housing for acoustic testing in Figure B.3(b). The transmission and absorption coefficients obtained experimentally for this set up without flow are shown in Figures B.4(b)and B.4(a). The

system was excited at different sound pressure levels to ensure the stability and linearity of the system. This was done for 100 dB, 120 dB and 130 dB. From observations made in FigureB.4 it can be affirmed that the system is linear.

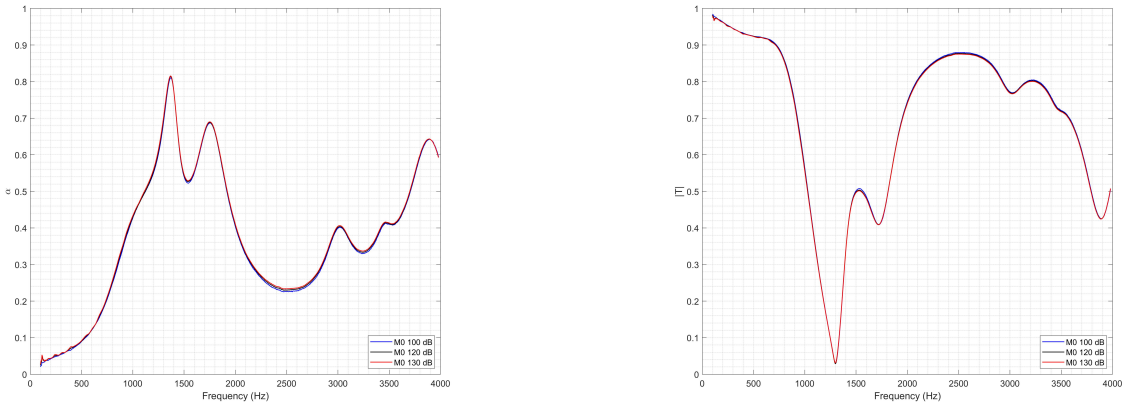

(a) Absorption

(b) Transmission coefficient

Figure B.4: Absorption and Transmission results for Denorms labyrinthine sample at different sound pressure levels under grazing incidence.

For optimal noise to signal ratio, an acoustic signal at 130 dB was used to excite the system and the response obtained was analysed with the addition of different external flow velocities. The absorption and transmission coefficients are given in the presence of different external flow velocities propagating in the same direction as the acoustic wave in Figure B.5. The addition of flow contributes to a slight reduction in the transmission coefficient at low flow velocities, and is more significant at higher flow velocities. However, the whistling effects in the system are minimal which is encouraging. Therefore the absorptivity provided by this configuration ensures good performance in the presence high flow velocities. As this type of structure shows good absorptive acoustic performance in the presence of flow, secondary tests with flow reversal were carried out.

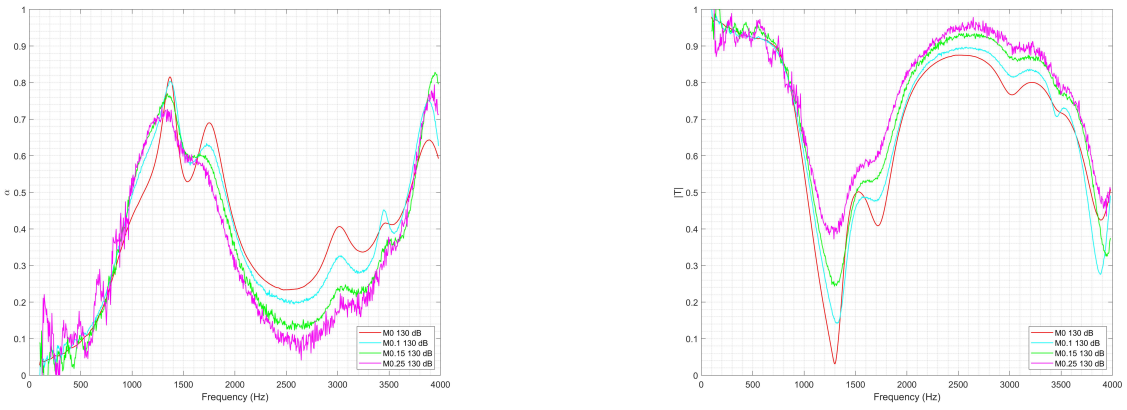

(a) Absorption (b) Transmission coefficient

Figure B.5: Absorption and Transmission results for Denorms labyrinthine sample for different Mach numbers at 130 dB where flow and sound waves propagate in the same direction.

The acoustic sources in this rig are provided by compression chambers upstream and downstream of the lined section. In the absorption and transmission coefficients plots shown in Figures B.5(a)and B.5(a), the acoustic source was located upstream of the sample, therefore results shown are composed of the acoustic wave travelling in the same direction as the flow. The results presented in B.6 display the absorption and transmission coefficients obtained at Mach 0.25 with the flow plotted as a continuous magenta line which are compared to results from the acoustic wave travelling against the flow represented by the dashed line. These results are plotted against a baseline result at the same sound pressure level without flow.

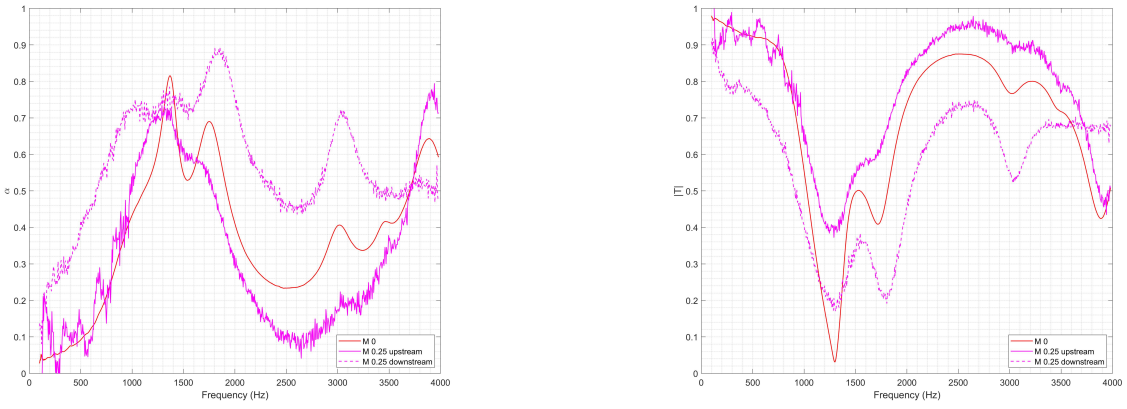

(a) Absorption (b) Transmission coefficient

Figure B.6: Absorption and Transmission results for Denorms labyrinthine sample for Ma 0.25 at 130 dB where waves propagate with (-) and against (- -) the flow.

Analysing both the absorption and transmission coefficients in Figures B.6(a)and B.6(b), it can be seen that with flow reversal against the acoustic wave the absorption increases by approximately 18%-24% with respect to the no flow case, and with respect to the acoustic wave and flow propagating in the same direction it increases by 28%-40%.

B.3 Grazing incidence results for plate design AC in Chapter 4

The plate design labelled AC in Chapter 4 was manufactured in order to test it in the grazing rig in Figure 2.11 with the pore radius. The drawings for this setup are available in Figure B.14, the plates are made from 1 mm think aluminium sheet and the air gaps between the plates are provided by 2 mm thick stainless steel spacers. This was assembled together by 8 screws placed on the sides which clamp the plate-air-gap-plate set-up. The holder which was made for the testing is shown in Figure B.7, a slot had been created into the holder in a potential case of adding a Kevlar sheet to the rectangular drum mount to ensure it was flush with the set up.

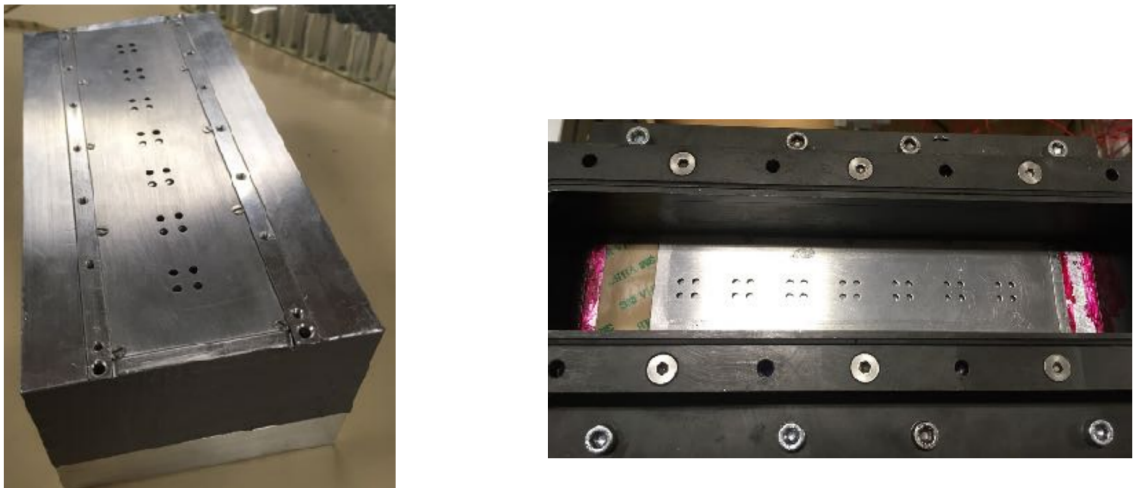

Figure B.7: Multilayered plates denoted as SET A in holder manufactured for test campaign with screws used to tighten the plates and spacers together.

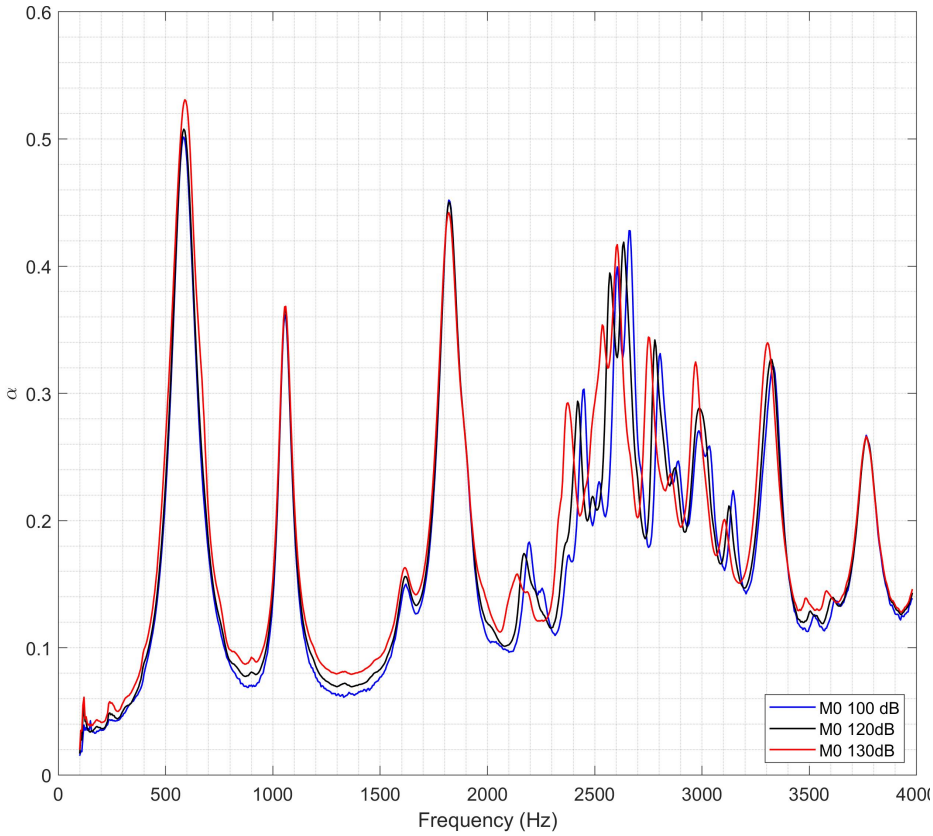

Figure B.8: Grazing incidence absorption coefficient results on sample A clamped with screws at different sound pressure levels.

The plane wave behaviour in this duct is assured until 3500 Hz, the absorption coefficient is shown at different sound pressure levels for SET A in Figure B.8. Even though the behaviour produced remains linear there is a level of sporadicity displayed for each test. Countersunk screws were used to clamp the plates together which was not necessarily the best approach as they can interact both with the acoustic wave and the external flow. To prevent this from occurring, double-sided tape was deposited on the sides of the plate which is shown in Figure B.9. The experiment without flow was reproduced at 130 dB. The absorption coefficient result of the modified experimental set-up with double-sided tape is compared to the original clamped screw set-up in Figure B.10.

Figure B.9: Multilayered plates denoted as SET A with double sided tape to remove interference produced by the screws.

The absorptivity obtained with the double-sided tape dampened the sporadic behaviour that was observed with the visible screw mounting. The amplitude of the first resonant peak was also larger, however the second resonant acoustic peak is 10% lower than with the visible screws in the test section. The sporadicity that predominated from 2300 Hz onwards is reduced and provides a lower absorption but a continuous broaderband behaviour.

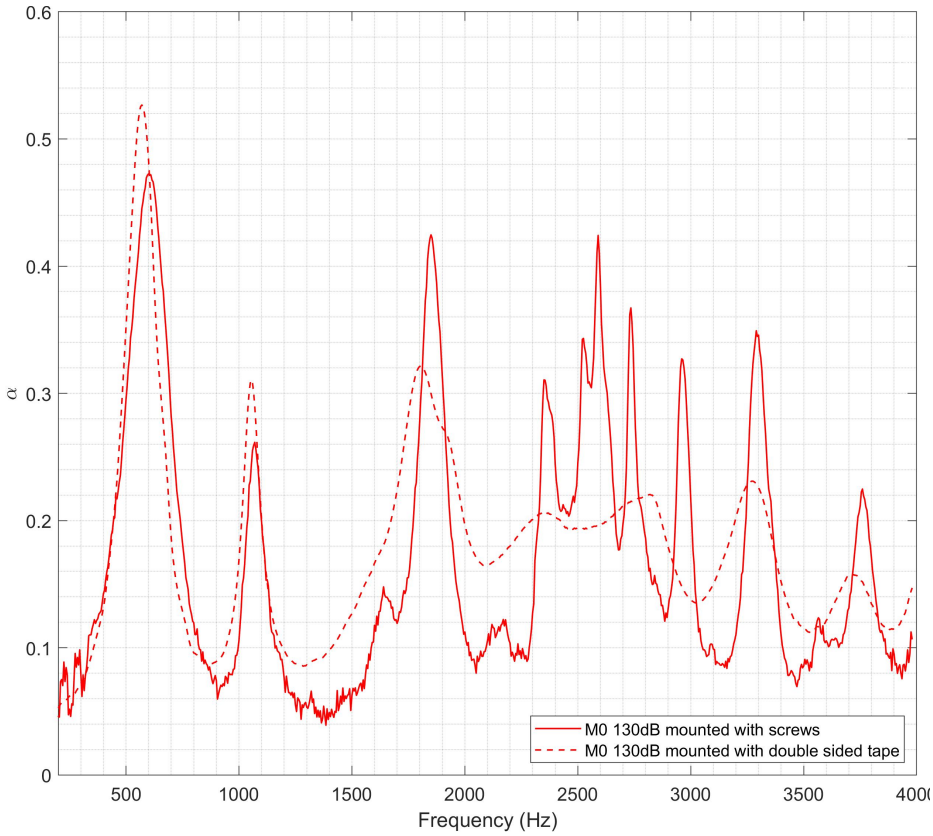

Figure B.10: Grazing incidence absorption coefficient results on sample A clamped with screws versus with double sided tape at 130 dB.

In a first instance, the experimental grazing results were compared with numerically obtained absorptivity results under a normal incident sound wave from an acoustic-structure interaction model. This is displayed in Figure B.11. The red plot corresponds to the experimental normal incident wave impinging on a PLA sample of three stacked AC plates. The dotted red plot corresponds to the absorptivity obtained from grazing incidence results over an aluminium-stainless steel configuration of 3 multilayered AC plates with a repeated pattern along the length of the lined section, therefore the sample has a different porosity. The local porosity of the sample would affect its local impedance as well, which can shift the resonant frequency. Therefore, comparing normal and grazing incident waves on the manufactured samples, the resonant frequencies for the grazing sample are shifted to the right as the porosity is increased. However, the difference observed remains minimal. The structural resonance observed from the grazing results at around 1000 Hz was not visible in the normal incident results visible experimentally which is to be expected as the plates are manufactured from different materials with differing natural frequencies at which they oscillate. The acoustic res-

onances observed occur around the same frequencies for the first and second acoustic modes, however under grazing the amplitude observed for the absorption coefficient is lower. The impedance obtained under normal incident plane wave does not account for any grazing incidence effects which might occur. However, these effects are not substantial as there is no additional external grazing flow represented in Figure B.11. Nonetheless, the results obtained show good agreement between normal and grazing incidence testing.

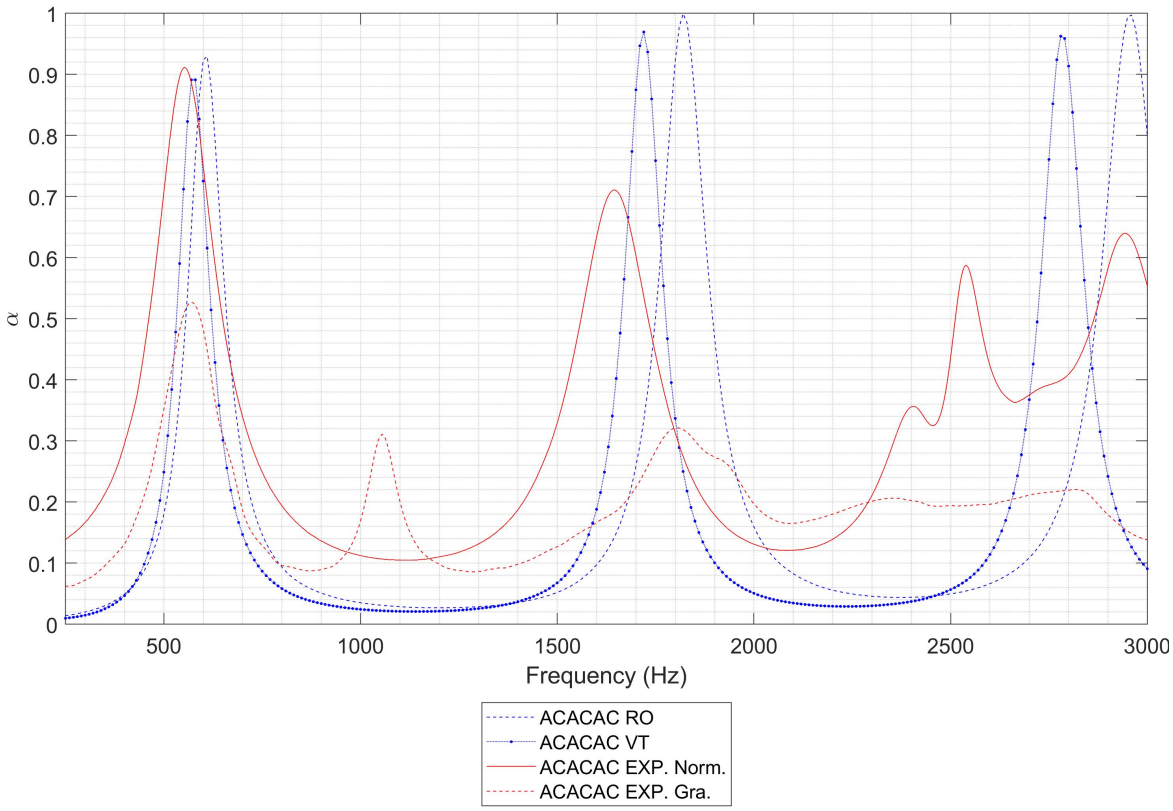

Figure B.11: Comparison of normal incident plane wave impinging on three stacked AC units compared with grazing incidence results on the same configuration adapted for the holder in the Le Mans grazing bench.

The plate configuration was tested in the grazing rig in the presence of flow at different velocities. The resulting cumulative effects of acoustic and flow velocities are shown through the absorption and transmission coefficients in Figures B.12(a) and B.12(b). The responses remains smooth despite an amplitude decrease with the addition of grazing flow at low Mach numbers and some instabilities occur at $Ma > 0.2$.

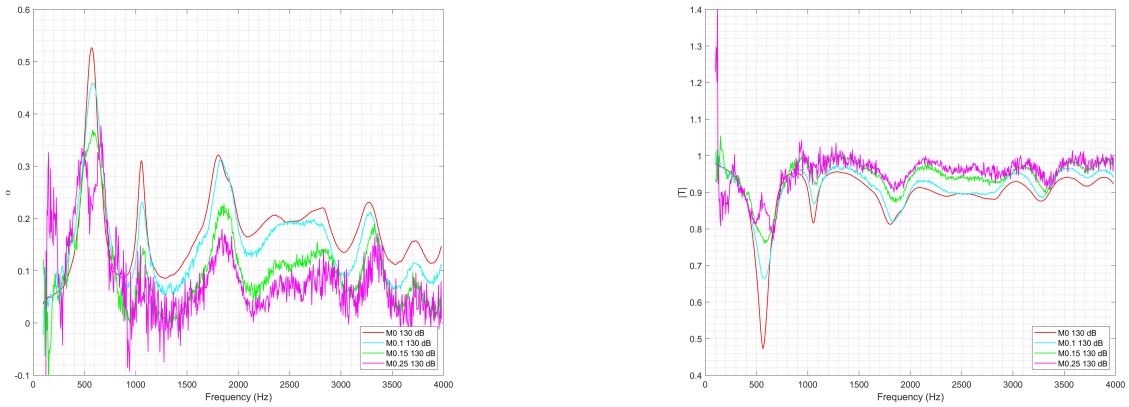

(a) Absorption (b) Transmission coefficient

Figure B.12: Absorption and Transmission results for multilayered Set A plates for different Mach numbers at 130 dB under grazing sound incidence with flow.

The configuration referred to as Set A in FigureB.14 system was investigated under flow reversal in Figures B.13(a) and B.13(b). The absorption and transmission coefficients for the acoustic wave propagating with and against the flow are compared against the no flow case at 130dB. The absorption when the acoustic wave was propagating against the grazing flow resulted in an increased absorption of around 25 % compared with both velocities in the same direction.

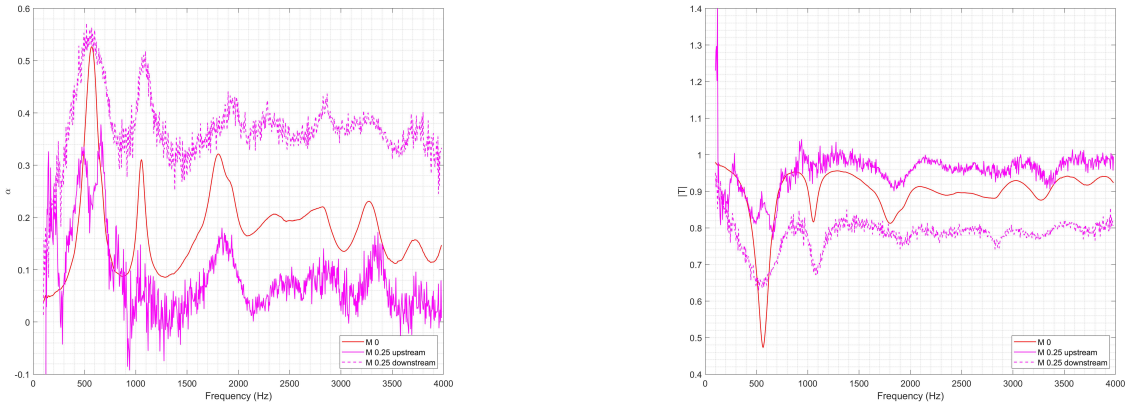

(a) Absorption (b) Transmission coefficient

Figure B.13: Absorption and Transmission results for multilayered plates, Set A for Ma 0.25 at 130 dB where waves propagate with (-) and against (- -) the flow.

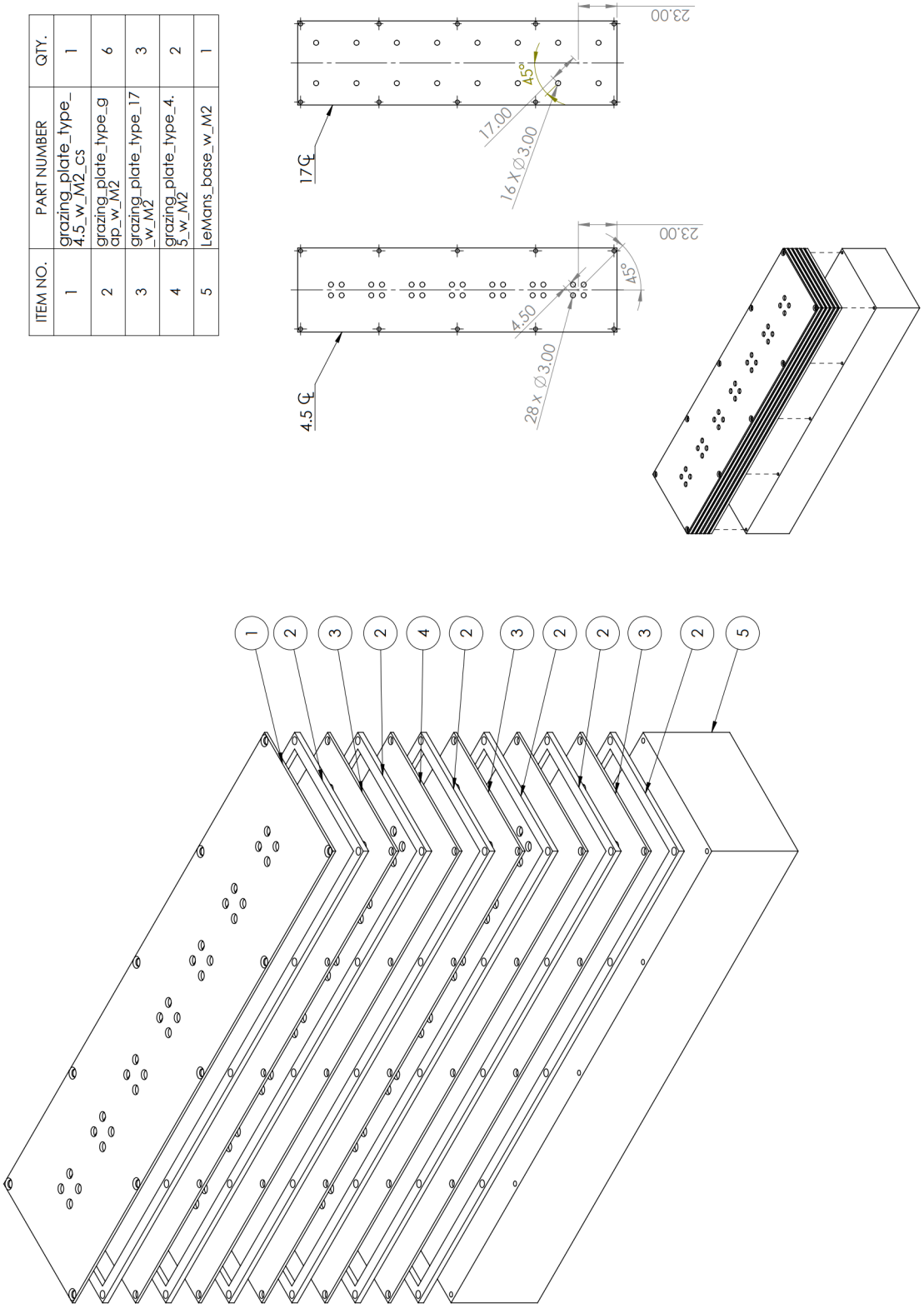

Figure B.14: Drawings of manufactured sample Set A (AC plates in Chapter 4) for grazing incidence test.

B.4 Grazing incidence results for unit plate design in Chapter 3

The first configuration of plates studied which was published in [50] was also manufactured for testing in the grazing rig at LAUM. The assembly used for Set A detailed in Section B.3 was also applied to Set B as in Figure B.18 using spacers made from stainless steel and the perforated plates from 1 mm aluminium sheet. As the results obtained with the exposed screw setup was not satisfactory double sided tape was added to this configuration in the holder in Figure B.15. The plate system shown was very similar to the previous design, in both cases the pores were 3 mm diameter, the hole location and the number of holes in each plate differed. The grazing flow tests were carried out at the highest signal to noise ratio (130 dB) possible. Results obtained under grazing incidence for different Mach numbers are presented through the absorption and transmission coefficients in Figures B.16(a) and B.16(b).

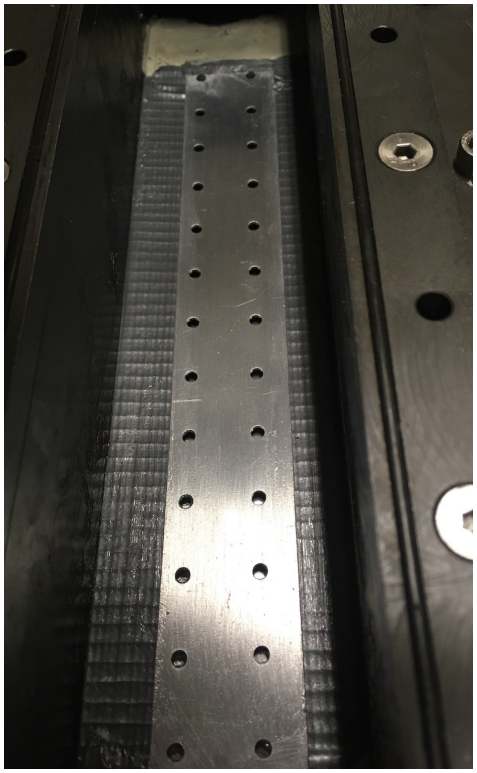

(a) Set B plates in holder

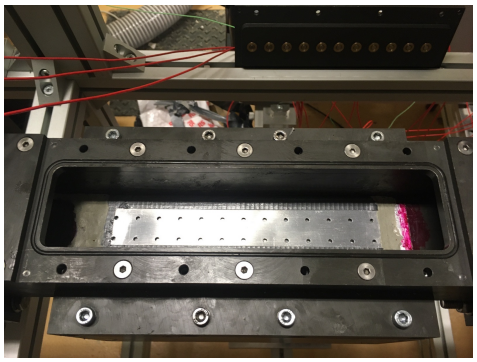

(b) Tape on existing screws to clamp plates and spacers

Figure B.15: Multilayered plates Set B following metaliner unit in Chapter 3 manufactured for grazing incidence testing.

The absorption is highest without the presence of flow, as the external flow velocities increase there is a further amplitude decrease in the absorption coefficient. With respect to the stability of the system it would seem that there is more noise at a lower Mach number compared to Set A. Indeed in Figure B.12(a), the behaviour appears to be less sporadic. The uneven number of pores on each alternating plates provide a merging of resonant peaks with compared to Set A, which provides a broader-band behaviour. However, further analysis would be required to determine the true nature of the resonance at 1100 Hz as from the study performed in [50] analysing solely acoustic modes it would seem to be of a structural nature.

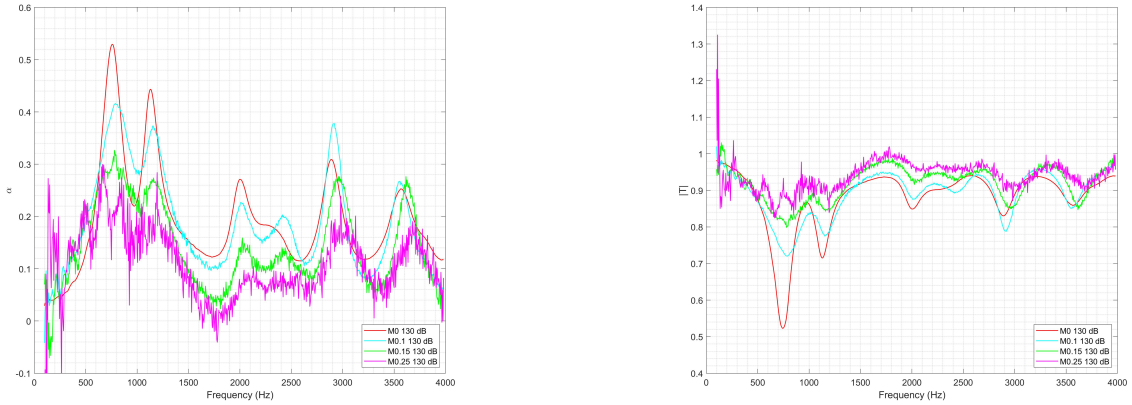

(a) Absorption

(b) Transmission coefficient

Figure B.16: Absorption and Transmission results for multilayered Set B plates at different sound pressure levels under grazing incidence.

As in previous cases the flow reversal contributes to increasing the amplitude of the absorption coefficient from approximately 20% to 40% with respect to the behaviour obtained when the acoustic wave propagates in the same direction as the external flow. Overall the absorption obtained exhibited a more broadband nature in the flow reversal scenario.

All the configurations examined exhibit a resistive behaviour, the sound pressure level and the grazing flow velocity contribute to diminishing the resistance of the acoustic treatment. However in the samples observed the reduction was not dramatic. This resistive behaviour observed has a potential benefit for aeronautical applications, the treatments seem relatively consistent under grazing flow which points to their suitability in engine duct environments. Inside turbofan engines the sound pressure level can reach approximately 160 dB and external flow velocities up to Ma 0.7. There are

limitations to representing operating conditions for liners in experimental setups both under normal incidence and grazing incidence with the addition of flow. Other variables come into play which are difficult to account for in test bench rigs used in this study.

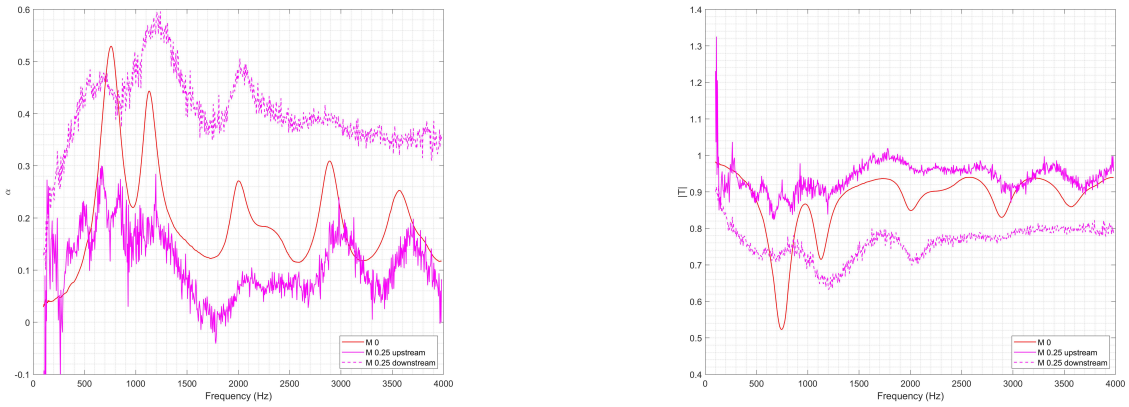

(a) Absorption

(b) Transmission coefficient

Figure B.17: Absorption and Transmission results for multilayered Set B plates for Ma 0.25 at 130 dB where waves propagate with (-) and against (- -) the flow.

ITEM NO.	PART NUMBER	QTY.
1	grazing_plate_type_2_7.5_w_M2_cs	1
2	grazing_plate_type_gap_w_M2	6
3	grazing_plate_type_1_15_w_M2	3
4	grazing_plate_type_2_7.5_w_M2	2
5	LeMans_base_w_M2	1

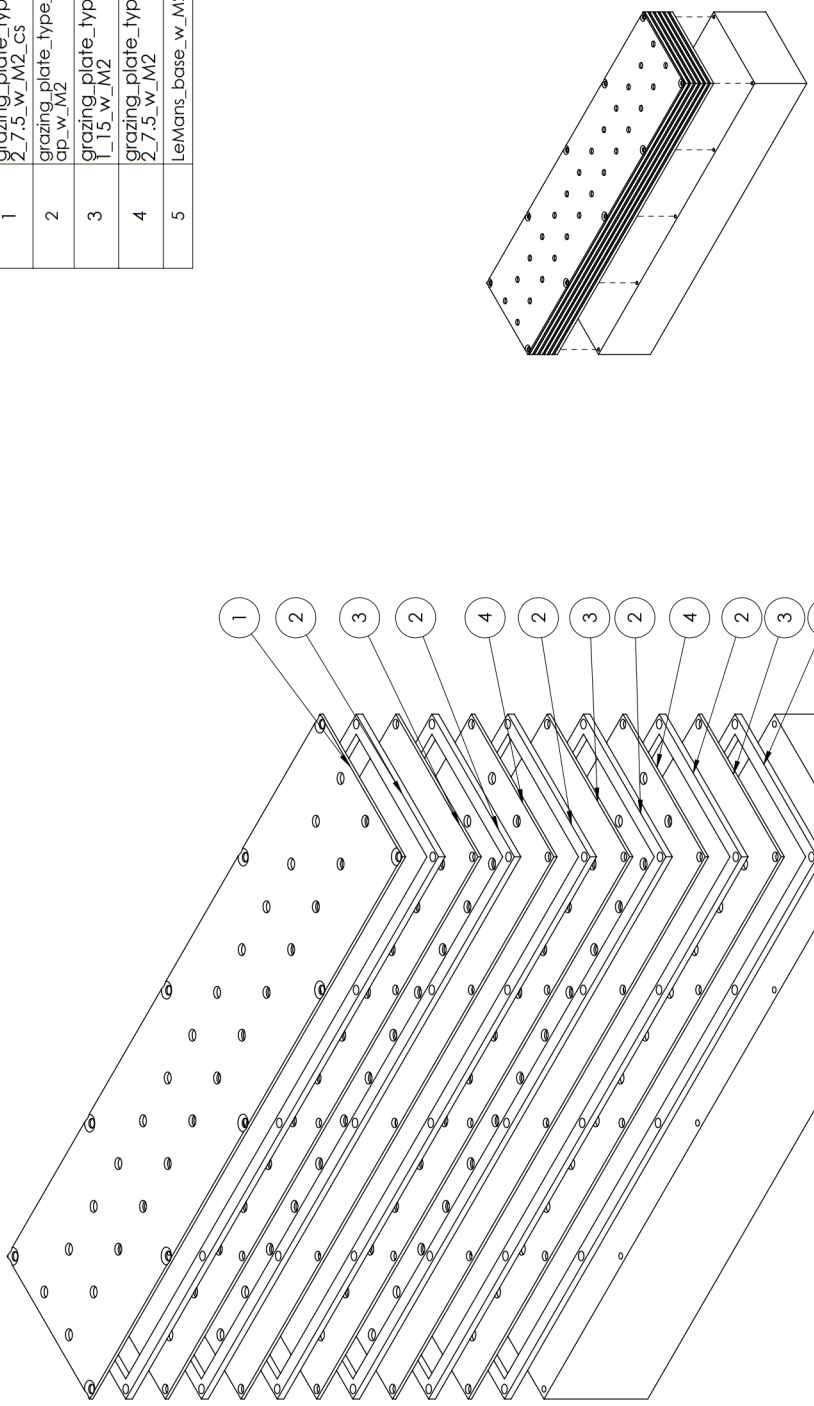

Figure B.18: Drawings of manufactured sample Set B (AB in Chapter 3) for grazing incidence tests.